RADC-TR-88-49
Final Technical Report
March 1988

CALIBRATED L-BAND TERRAIN MEASUREMENTS AND ANALYSIS PROGRAM - RESULTS

Environmental Research Institute of Michigan

R. W. Larson, E. S. Kasischke and A. L. Maffett

APPROVED FOR PUBLIC RELEASE; DISTRIBUTION UNLIMITED.

ROME AIR DEVELOPMENT CENTER
Air Force Systems Command
Griffiss Air Force Base, NY 13441-5700

This report has been reviewed by the RADC Public Affairs Office (PA) and is releasable to the National Technical Information Service (NTIS). At NTIS it will be releasable to the general public, including foreign nations.

RADC-TR-88-49 has been reviewed and is approved for publication.

APPROVED: K V N Rao

K. V. N. RAO
Project Engineer

APPROVED: John K Schindler

JOHN K. SCHINDLER
Acting Director of Electromagnetics

FOR THE COMMANDER: John A. Ritz

JOHN A. RITZ
Directorate of Plans & Programs

If your address has changed or if you wish to be removed from the RADC mailing list, or if the addressee is no longer employed by your organization, please notify RADC (EECE) Hanscom AFB MA 01731-5000. This will assist us in maintaining a current mailing list.

Do not return copies of this report unless contractual obligations or notice on a specific document requires that it be returned.

UNCLASSIFIED
SECURITY CLASSIFICATION OF THIS PAGE

AD-A196 332

REPORT DOCUMENTATION PAGE

Form Approved
OMB No. 0704-0188

1a. REPORT SECURITY CLASSIFICATION UNCLASSIFIED	1b. RESTRICTIVE MARKINGS N/A
2a. SECURITY CLASSIFICATION AUTHORITY N/A	3. DISTRIBUTION/AVAILABILITY OF REPORT Approved for public release; distribution unlimited.
2b. DECLASSIFICATION/DOWNGRADING SCHEDULE N/A	
4. PERFORMING ORGANIZATION REPORT NUMBER(S) 174200-16-F	5. MONITORING ORGANIZATION REPORT NUMBER(S) RADC-TR-88-49
6a. NAME OF PERFORMING ORGANIZATION Environmental Research Institute of Michigan 6b. OFFICE SYMBOL (If applicable)	7a. NAME OF MONITORING ORGANIZATION Rome Air Development Center (EECE)
6c. ADDRESS (City, State, and ZIP Code) P.O. Box 8618 Ann Arbor MI 48107	7b. ADDRESS (City, State, and ZIP Code) Hanscom AFB MA 01731-5000
8a. NAME OF FUNDING/SPONSORING ORGANIZATION Rome Air Development Center 8b OFFICE SYMBOL (If applicable) EECE	9. PROCUREMENT INSTRUMENT IDENTIFICATION NUMBER F19628-84-C-0081
8c. ADDRESS (City, State, and ZIP Code) Hanscom AFB MA 01731-5000	10. SOURCE OF FUNDING NUMBERS PROGRAM ELEMENT NO. 62702F; PROJECT NO. 4600; TASK NO. 15; WORK UNIT ACCESSION NO. 73

11. TITLE (Include Security Classification)
CALIBRATED L-BAND TERRAIN MEASUREMENTS AND ANALYSIS PROGRAM - RESULTS

12. PERSONAL AUTHOR(S)
R. W. Larson, E. S. Kasischke and A. L. Maffett

13a. TYPE OF REPORT	13b. TIME COVERED	14. DATE OF REPORT (Year, Month, Day)	15. PAGE COUNT
Final	FROM Apr 84 TO Jan 87	March 1988	114

16. SUPPLEMENTARY NOTATION
N/A

17. COSATI CODES		
FIELD	GROUP	SUB-GROUP
17	09	
20	14	

18. SUBJECT TERMS (Continue on reverse if necessary and identify by block number)
Radar, Terrain, L-Band, Measurement, Backscatter Cross Sections (See Reverse)

19. ABSTRACT (Continue on reverse if necessary and identify by block number)

This report discusses the final year's activities of a program to generate and analyze L-band clutter data. The L-band radar data used throughout this study were derived from airborne synthetic aperture radar imagery. Radar cross section measurements from a variety of distributed targets are presented, including sea surface, sea ice, agricultural fields and forests. Both HH and VV polarized data are presented. Models are presented which describe the intensity distribution of the SAR data as well as describe L-band scattering from rough surfaces. The density distribution models describe the observed SAR intensity distributions quite well, whereas the radar scattering models in some cases overpredict the SAR-observed values.

20. DISTRIBUTION/AVAILABILITY OF ABSTRACT	21 ABSTRACT SECURITY CLASSIFICATION
☒ UNCLASSIFIED/UNLIMITED ☐ SAME AS RPT ☐ DTIC USERS	UNCLASSIFIED

22a. NAME OF RESPONSIBLE INDIVIDUAL	22b TELEPHONE (Include Area Code)	22c OFFICE SYMBOL
K. V. N. Rao	(617) 377-3585	RADC (EECE)

DD Form 1473, JUN 86 *Previous editions are obsolete.* SECURITY CLASSIFICATION OF THIS PAGE
UNCLASSIFIED

17. COSATI CODES (Continued).

Field	Group
09	03

18. SUBJECT TERMS (Continued).

Calibration
SAR Imagery

TABLE OF CONTENTS

LIST OF FIGURES

LIST OF FIGURES
(Continued)

LIST OF FIGURES
(Concluded)

LIST OF TABLES

CALIBRATED L-BAND TERRAIN MEASUREMENTS AND ANALYSIS PROGRAM - RESULTS

1 INTRODUCTION

This report presents the results obtained during the three years of the Calibrated L-band Terrain Measurements and Analysis Program conducted by the Environmental Research Institute of Michigan (ERIM) for the Rome Air Development Center of the USAF. The overall goal of this program was to provide L-band radar clutter data from a variety of terrain types and sea states and to begin to evaluate models which describe the radar clutter. The approach adopted for this program was to utilize airborne synthetic aperture radar (SAR) (Rawson, et al., 1985) imagery as a source for the L-band clutter data. The SAR imagery used during this program was provided courtesy of several different U.S. Government sponsors. The primary data sets were collected over central North Carolina during a U.S. Geological Survey Radar data collection (Kasischke, 1985; Kover and Jones, 1985) and over Long Island, New York during the ONR-sponsored SARSEX experiment (Kasischke, et al., 1985). Additional SAR data was collected over the Marginal Ice Zone during the ONR-sponsored MIZEX '84 experiment (MIZEX Group, 1986).

This program was conducted in two distinct phases. During Phase I, four distinct tasks were performed: (1) collection of SAR data and associated ground truth information; (2) processing and calibration of SAR data of selected test areas; (3) reduction of ground-truth data; and (4) selection of radar surface scattering models. The Phase I activities are summarized by Larson, et al. (1986). During Phase II, the following tasks were performed: (1) extraction of calibrated L-band radar cross section measurements from the SAR data; (2) evaluation and modeling of the image intensity distributions observed on SAR imagery; and (3) comparison of the radar scattering coefficients obtained in Phase 1 to the ground-truth data via

deterministic models and statistical analyses. The procedures used to analyze the SAR imagery, along with the results of these analyses are presented in this report.

Including this introduction, this report includes five chapters. Chapter 2 presents a summary of the radar scattering coefficients extracted during this program. In addition to the L-band SAR data, a limited amount of X-band and C-band radar scattering coefficient measurements were made available to this program. These measurements are summarized in this chapter. Chapter 3 of this report discusses the modeling of the intensity distributions observed on SAR data. Chapter 4 presents the results of the comparison of the SAR radar cross sections to the ground-truth data. Finally, Chapter 5 discusses the conclusions and recommendations from this program.

2
L-BAND RADAR SCATTERING COEFFICIENTS

In this chapter, the radar scattering coefficient (σ^o) measurements derived from the various SAR data sets are presented. Calibration of the SAR system is described in the interim report (Larson, et al 1986). Because the size of the individual test sites within the several different data sets varied considerably, different data extraction and display techniques were employed. These techniques will be discussed in the different sections of this chapter.

In this chapter, we will present σ^o measurements from four different test areas:

1 Long Island, New York (SARSEX)
2. Duke Forest, North Carolina (USGS)
3. Atlantic Ocean (SARSEX), and
4. Fram Strait, Greenland Sea (MIZEX).

2.1 LONG ISLAND, NEW YORK TEST SITES

The Long Island, New York test sites were imaged during a number of different passes during the SARSEX experiment. The test sites used for this study were located in and around the Peconic River Airport, which is owned and operated by Grumman Aerospace Corporation. For this analysis, we will present data collected during six different SAR passes on two separate dates at different incidence angles and polarizations. Specifically, we will present data from four passes where HH-polarization data were collected and data from two passes where VV-polarization data were collected. Figures 1 and 2 present examples of the L-band HH- and VV-polarized SAR imagery collected over the Long Island test sites.

Radar scattering coefficient (σ^o) measurements were extracted from 22 different test sites. These test sites are summarized in Table 1

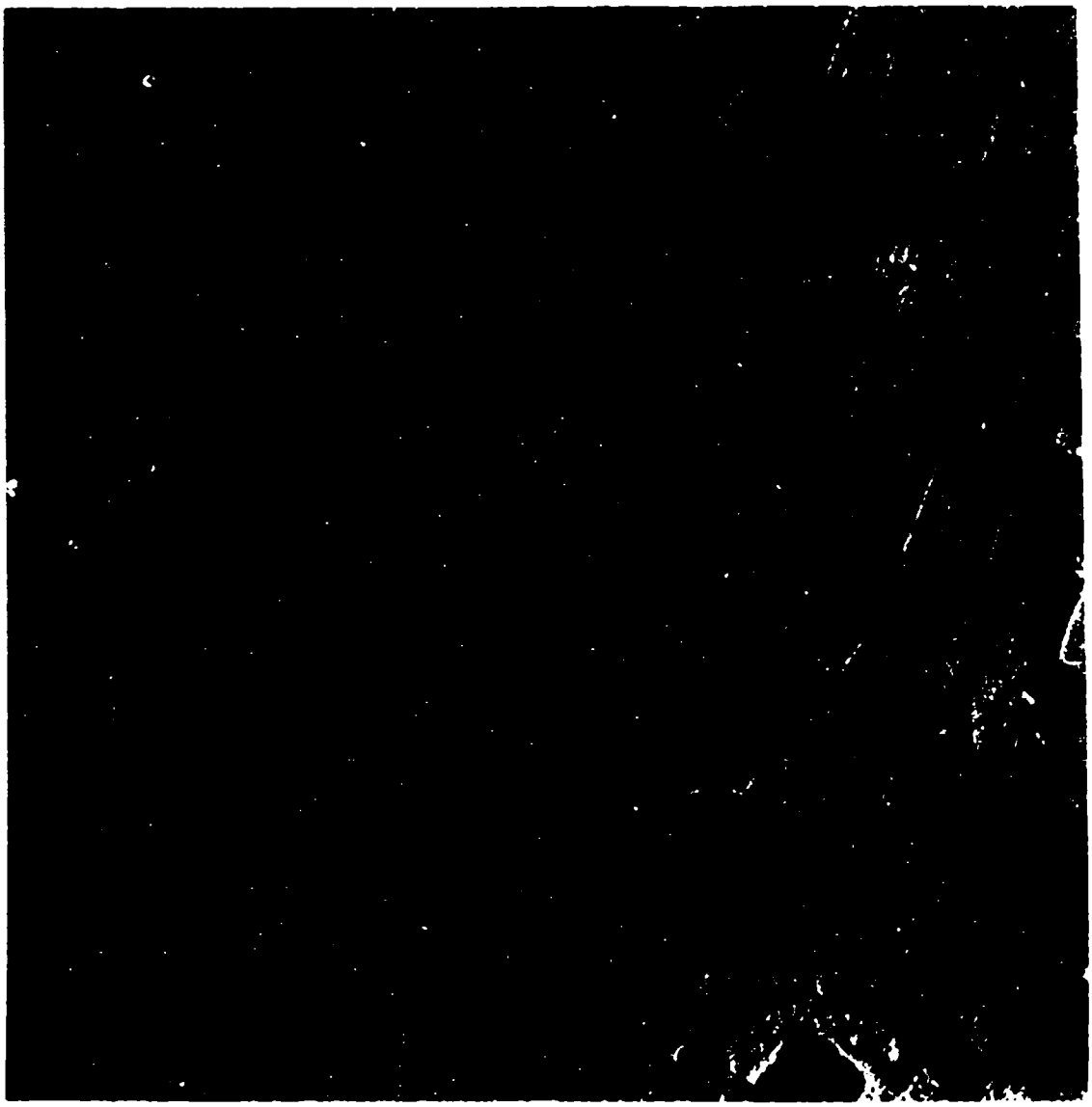

Figure 1. L-band (HH) SAR Imagery of the Long Island Test Sites Collected During SARSEX-10, Pass 1, 7 October 1984

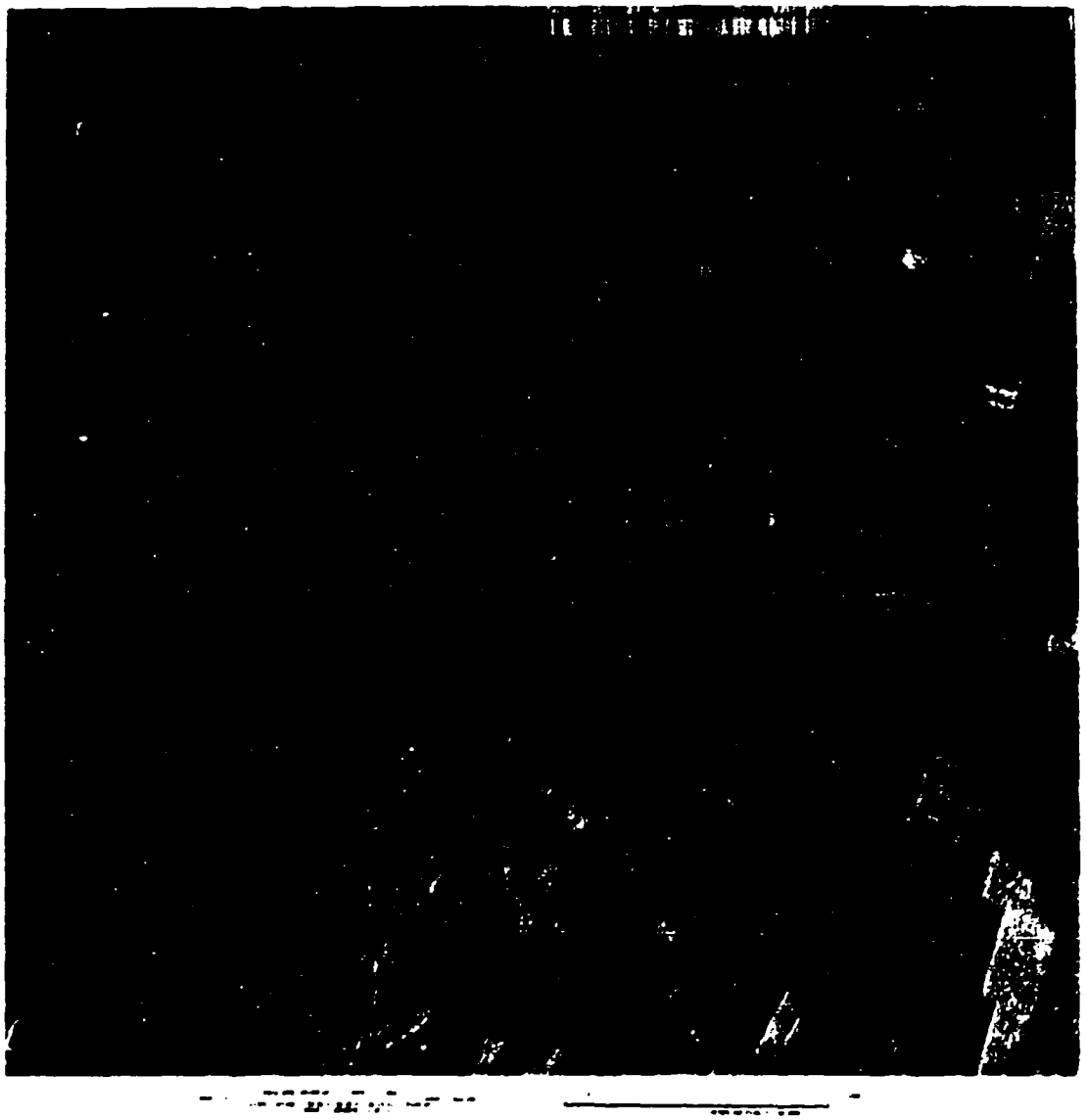

Figure 2. L-band (VV) SAR Imagery of the Long Island Test Sites Collected During SARSEX-10, Pass 3, 7 October 1984

TABLE 1

LONG ISLAND TEST SITES

Site Designation	Site Description
A	Strawberry Field
B	Orchard
C	Smooth, Bare Field
D	Smooth Field - Near South Rd. Potatoes - South Side
E	Potatoes
O	Potatoes
8	Potatoes
3	Potatoes
F	Grass
H	Corn Stalks
I	Grass
J	Cabbage
K	Grass Field (VOR, Reflectors)
RF1	Grass Field
RF2	Grass Field
RF3	Grass Field
L	Short Pike, Trees - Weeds
M	Smooth, Bare Field
N	Smooth, Bare Field
O	Smooth, Bare Field
P	Smooth, Bare Field
Q	Sod
R	Sod
W	Sod
Z	Bare, Smooth Field, N-S Furrows

and their locations presented in Figure 3. Figure 4 presents selected surface photographs illustrating the different types of ground cover present at the Long Island test sites. (Other photographs included in Larson, et al 1986).

The σ^0 measurements were generated by averaging a 40 by 40 pixel subset from the individual test sites. The ERIM SAR image processor generates pixels with a dimension of 1.5 by 1.44 m. The 3 m resolution of the SAR data is therefore oversampled by a factor of 2 in both the range and azimuth dimensions. In order to estimate the number of independent looks, N, for the σ^0 measurements, we must divide the number of pixels averaged by 2 in both the range and azimuth dimensions (Kasischke, et al., 1987). Each σ^0 value thus was generated using 400 independent samples (20 by 20 pixels), resulting in a 90% confidence interval due to speckle or fading of $\pm$ 0.35 dB, assuming that radar speckle has a chi-square distribution (Ulaby, et al., 1982).

Another source of uncertainty in the σ^0 measurements is the within field variation present in the data. To measure this uncertainty, six different σ^0 measurements were obtained from three of the test sites (F, G and H) at four separate incidence angles using the L-band (HH) data sets. These measurements are summarized in Table 2. The maximum standard deviation obtained was 0.5 dB. We can define a standard error of the mean (SE) as

$$SE = SD/N^{1/2} \qquad (1)$$

where SD is the standard deviation and N is the number of samples averaged. Doing so results in a maximum standard error of $\pm$ 0.3 dB. Combining the uncertainty due to radar fading, with the maximum uncertainty due to the within field variability results in a maximum $\pm$ 0.5 dB error bound for the σ^0 measurements. In Figure 5, we plot

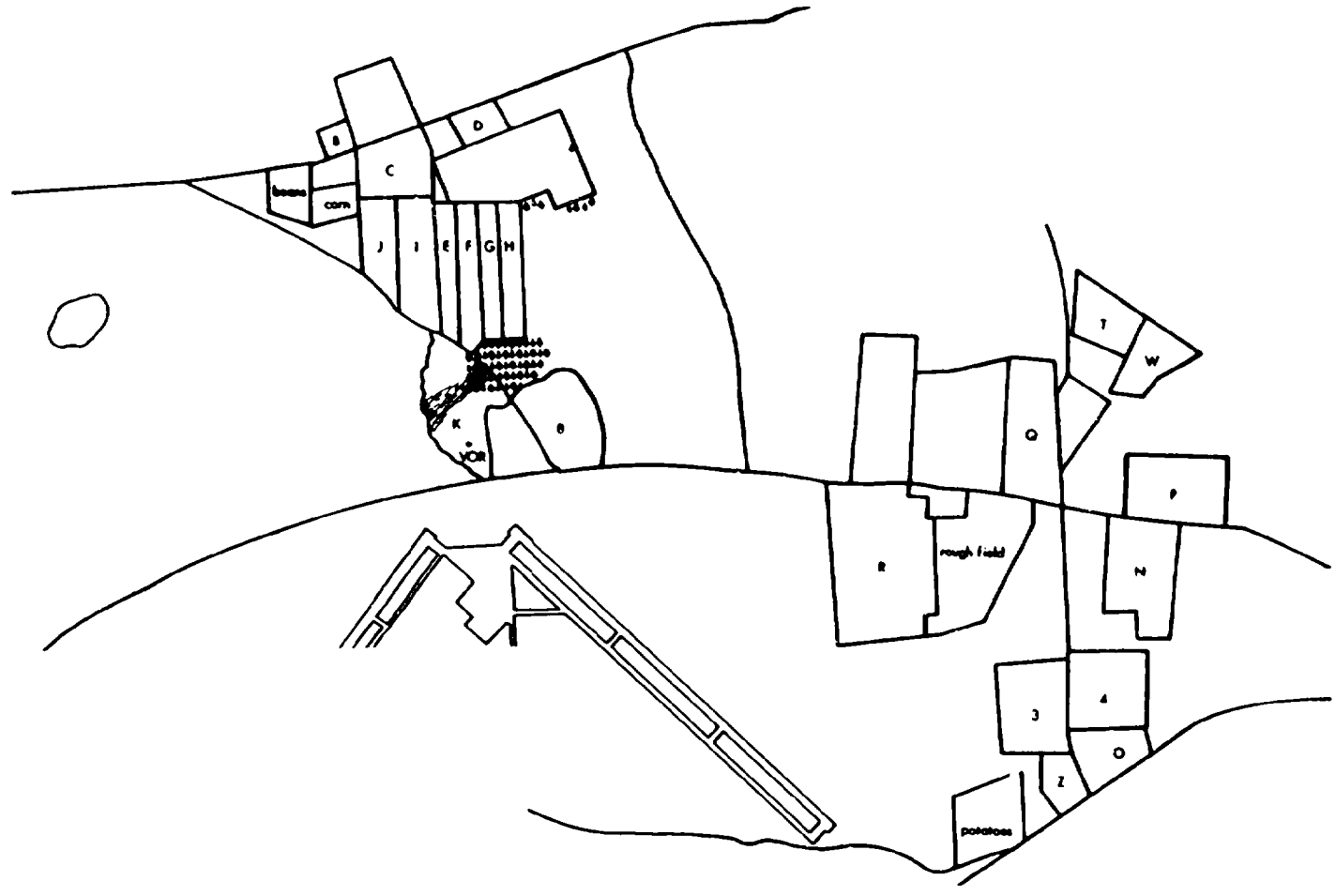

Figure 3. Location of Test Sites Around the Peconic River Airport Long Island

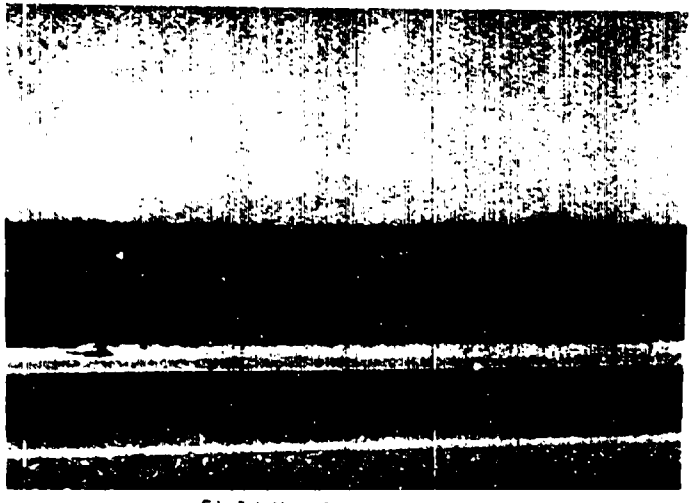

Field M - Smooth Field

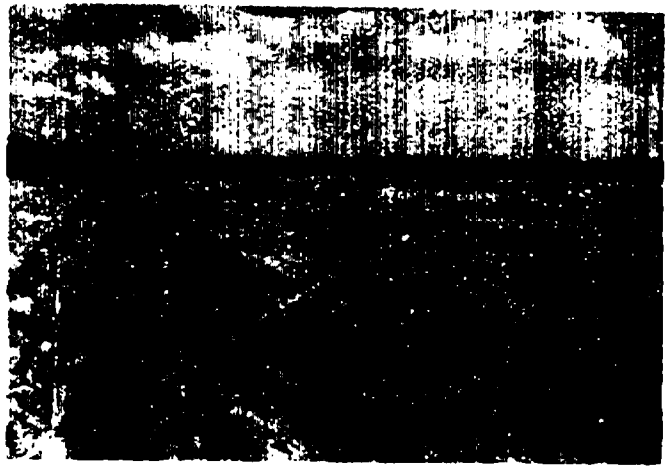

Field RFS-3 - Reflector Site Area

Field H - Cut Corn, East of Field G

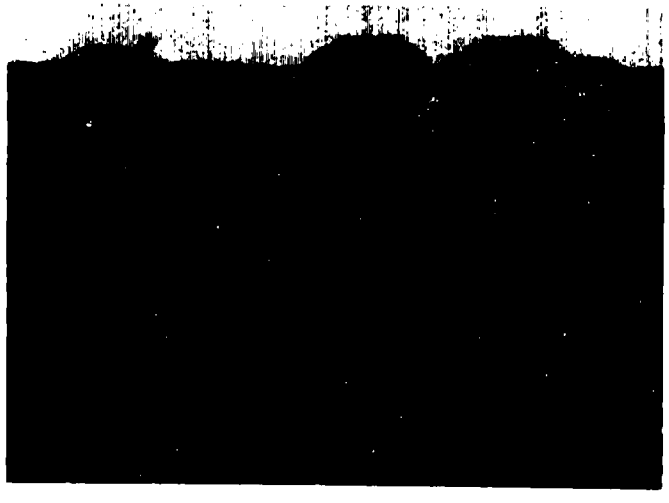

Field K - Tall Grass Field

Figure 4. Surface Photographs of Selected Long Island Test Sites

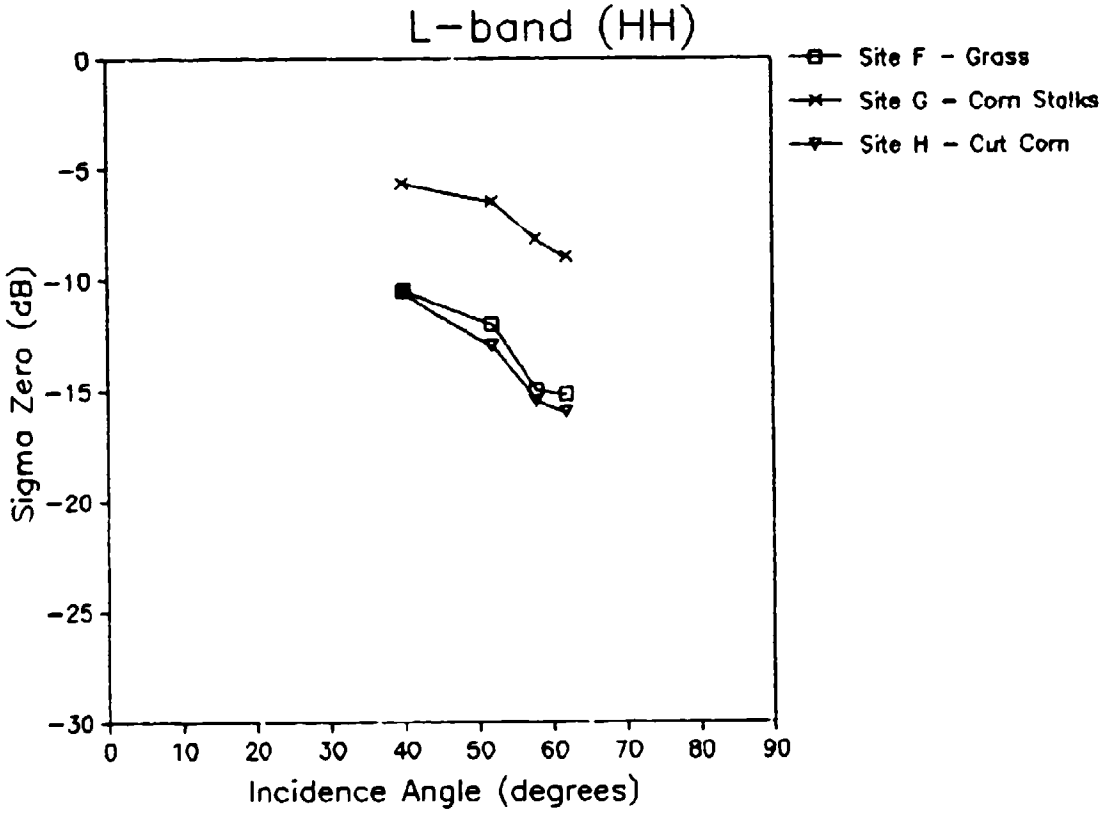

Figure 5. Plot of Average L-band (HH) σ^{o} Values for Three Test Sites

TABLE 2

AVERAGE VALUES, STANDARD DEVIATIONS, AND STANDARD ERRORS OF σ^{o} FROM THREE DIFFERENT TEST SITES (N = 6)

F (grass), G (corn stalks), and H (corn stubble)
(Each area consists of 400 samples. Values given for four values of incidence angle.)

	Incidence Angle			
	48°	52°	58°	62°
Site F - Grass				
σ^{o} average/dB	0.0893/-10.5 db	0.0642/12 dB	0.0327/15 dB	0.0299/-15.2 dB
S.D./dB	0.078.0.3 dB	0.0063/0.40 dB	0.0052/0.60 dB	0.0032/0.40 dB
S.E./dB	0.0032/0.12 dB	0.0026/0.16 dB	0.0021/0.24 dB	0.0013/0.20 dB
Site G - Corn Stalks				
σ^{o} average/dB	0.271/-5.7 dB	0.225/-6.5 dB	0.152/-8.2 dB	0.125/-9 dB
S.E./dB	0.0200/0.31 dB	0.0200/0.37 dB	0.013/0.30 dB	0.0100/0.33 dB
S.E./dB	0.0082/0.13 dB	0.0082/0.15 dB	0.0053/0.15 dB	0.0041/0.13 dB
Site H - Corn Stubble				
σ^{o} average/dB	0.087/-10.6 dB	0.05/-13 dB	0.028/-15.5 dB	0.025/-16 dB
S.D./dB	0.0052/0.25 dB	0.0050/0.40 dB	0.003 '0.50 dB	0.0032/0.50 dB
S.E./dB	0.0021/0.10 dB	0.0020/0.16 dB	0.0015/0.21 dB	0.0013/0.20 dB

the σ° measurements presented in Table 2. We can see that for all 3 test sites, there is a clear decrease in σ° as incidence angle increases. In these examples, the σ° values for the standing corn stalks are clearly 5 dB higher than the other two test sites, whose σ° values are essentially equivalent.

The σ° values for the 14 test sites are summarized in Figure 6. From these graphs, we can note the following trends. In general, for L-band (HH) radar data, as incidence angle increases, σ° decreases. This trend was observed for all data sets. The trend for the L-band (VV) data was not as clear, with σ° both increasing and decreasing as incidence angle increases.

Figure 7 presents a composite plot of the various fields compared to one another. In this plot, we combined all similar test sites to obtain an average σ° signature for a particular terrain type. In this plot, we compare only the L-band (HH) data sets. The highest σ° values were obtained for the orchard and corn stalks, while the lowest were obtained for the sod and potato fields. There is clearly a 10 dB difference between the darkest and brightest fields at all incidence angles.

2.2 DUKE FOREST TEST SITES

In early April 1984, during a data collection program conducted for the U.S. Geological Survey (Kover and Jones, 1985), multifrequency, multipolarization SAR data were collected over the Duke Forest using the ERIM/CCRS CV580 SAR System (see Figures 8 and 9). In this study we utilize L-band (VV) data collected on 8 April 1984 and X and C-band (VV) data collected on 10 April 1984. The deciduous trees in the study area were at a stage where most of the buds had burst, but no significant leaf flushing or new stem growth had occurred. The weather conditions were identical on each day of the SAR data collection, with overcast skies and periods of light rain.

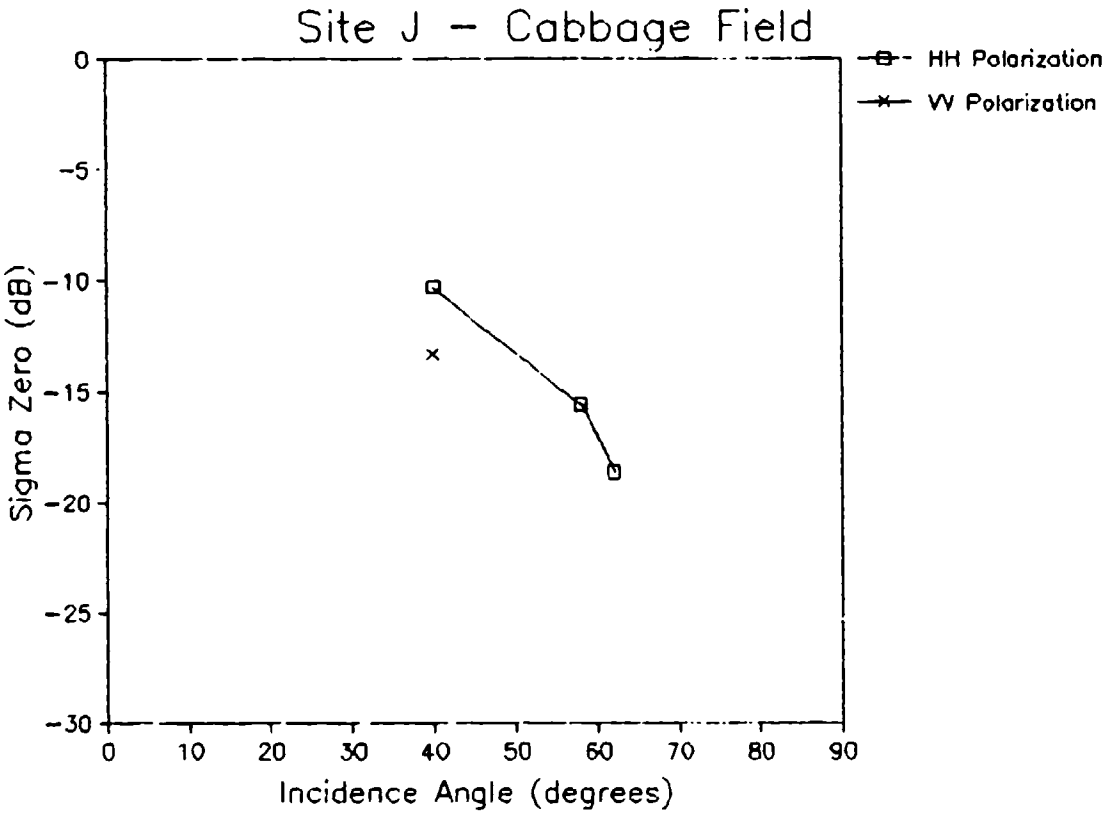

Figure 6. Plots of L-band (HH and VV) σ^{o} Values for the Long Island Test Sites [Figures (a) through (n)]

(a). Cabbage Field (Site J)

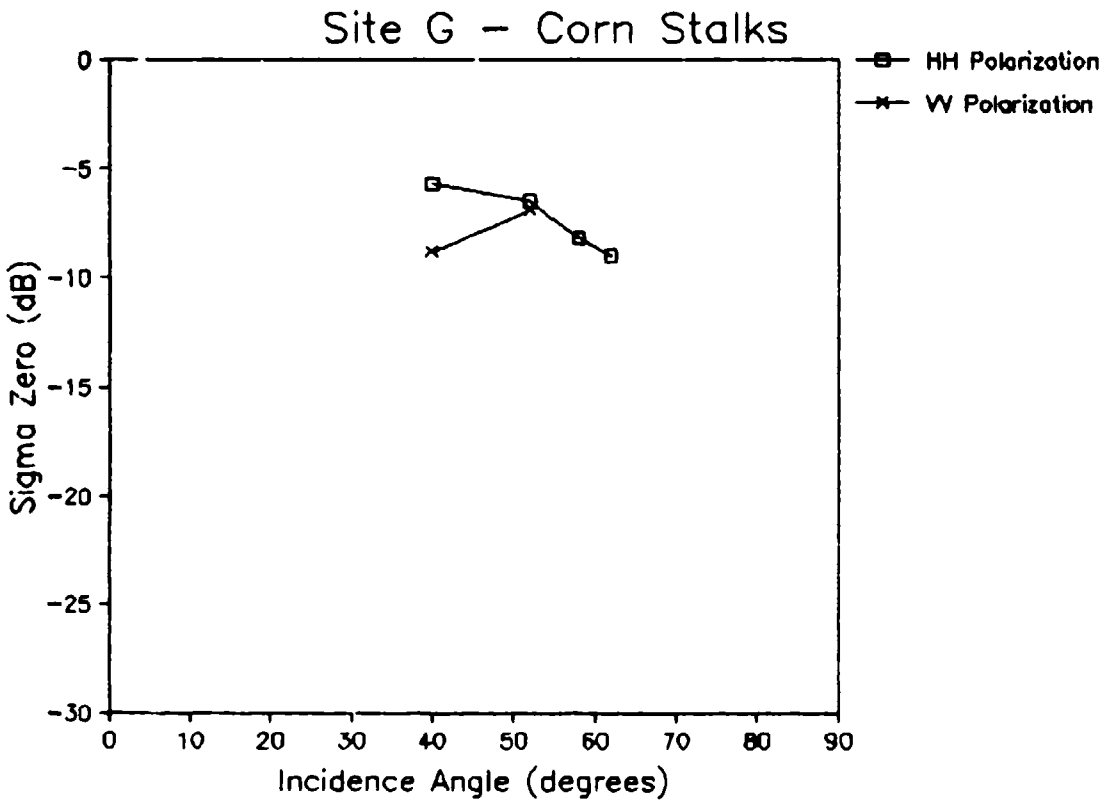

Figure 6 (b). Corn Stalks (Site G)

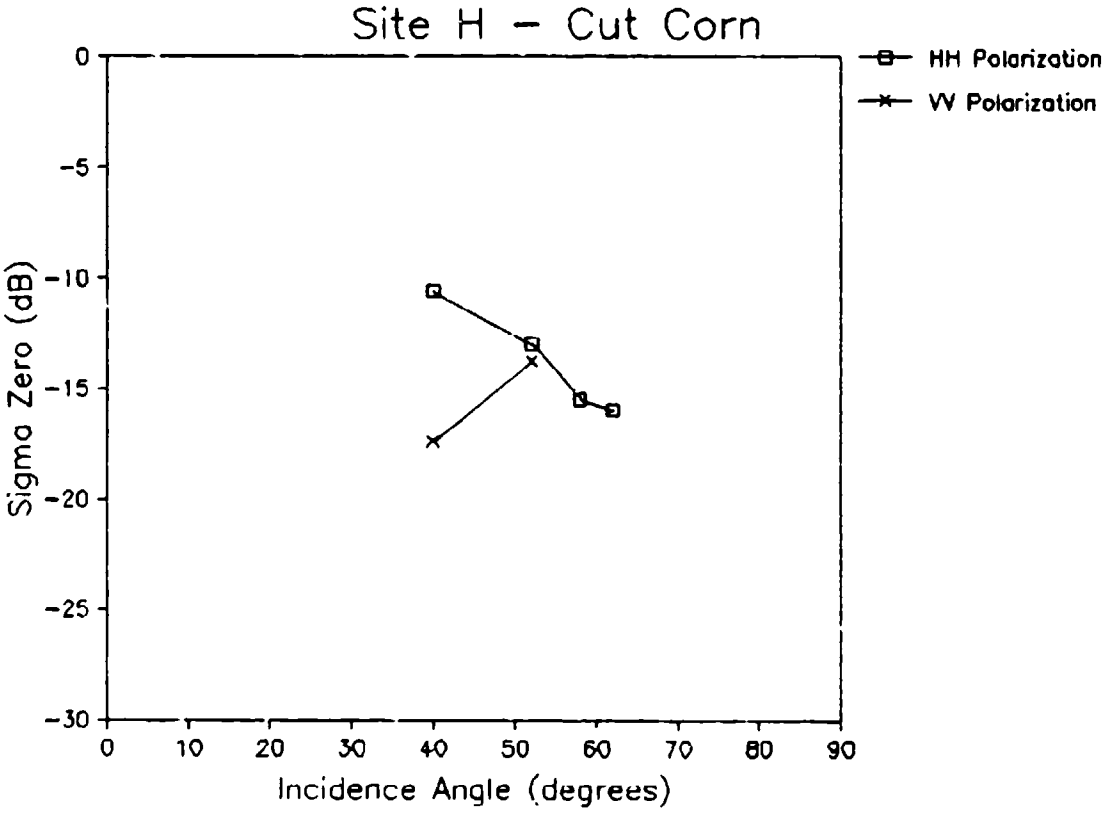

Figure 6 (c). Cut Corn (Site H)

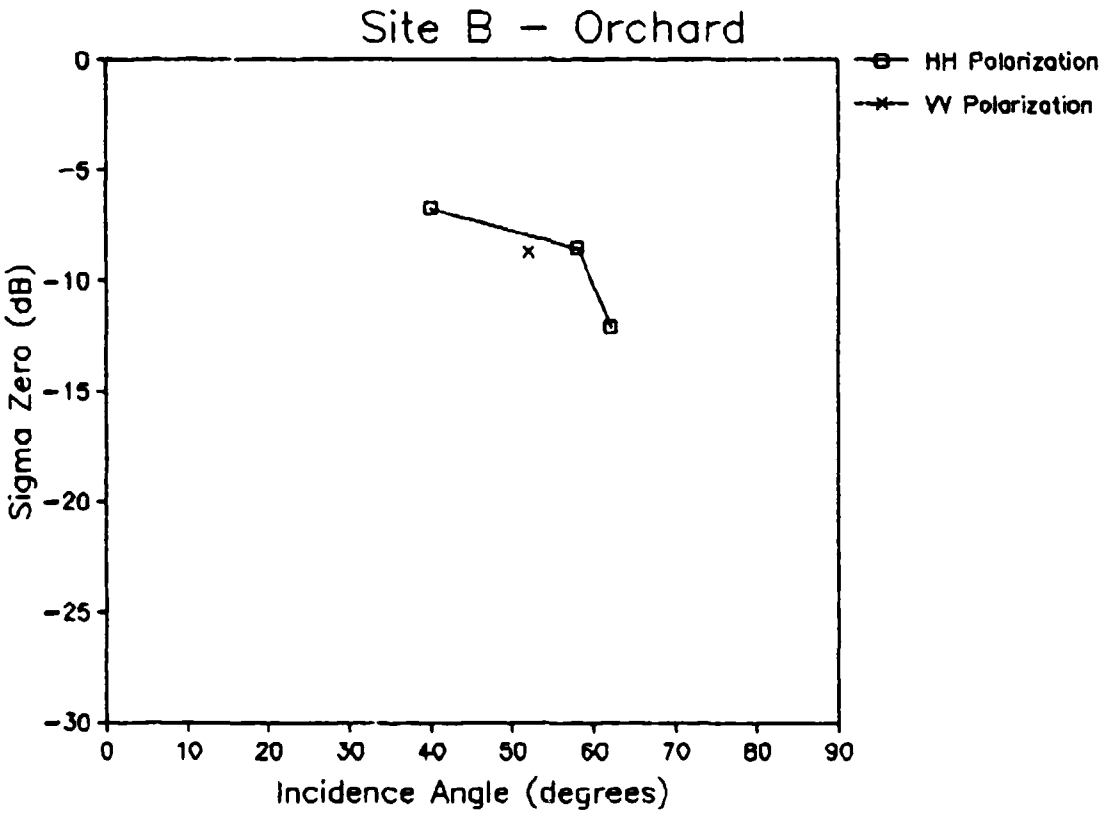

Figure 6 (d). Orchard (Site B)

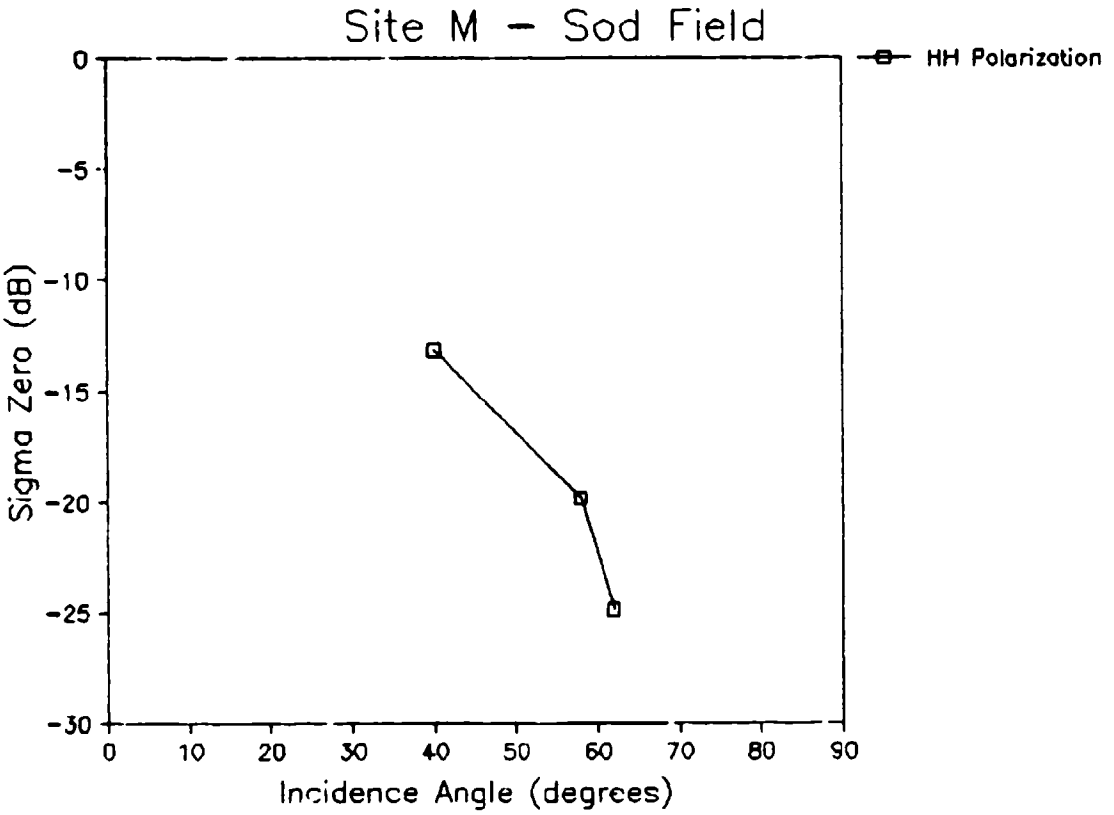

Figure 6 (e). Sod Field (Site M)

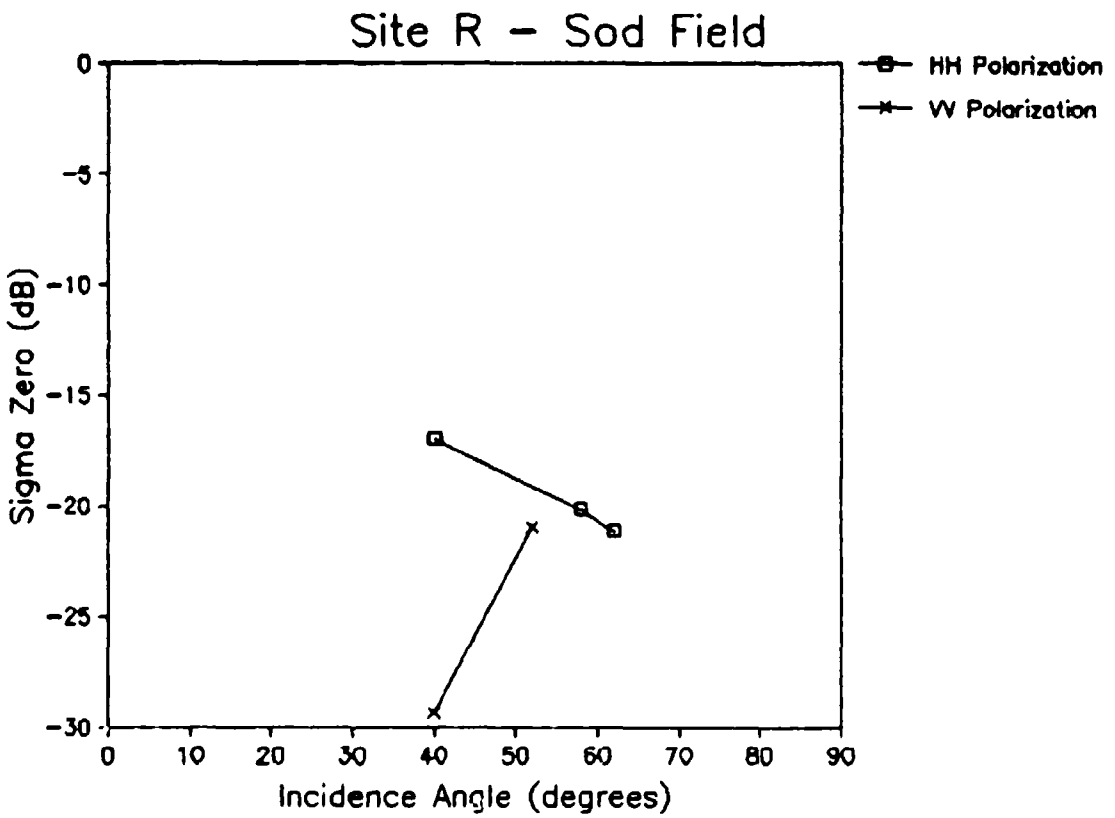

Figure 6 (f). Sod Field (Site R)

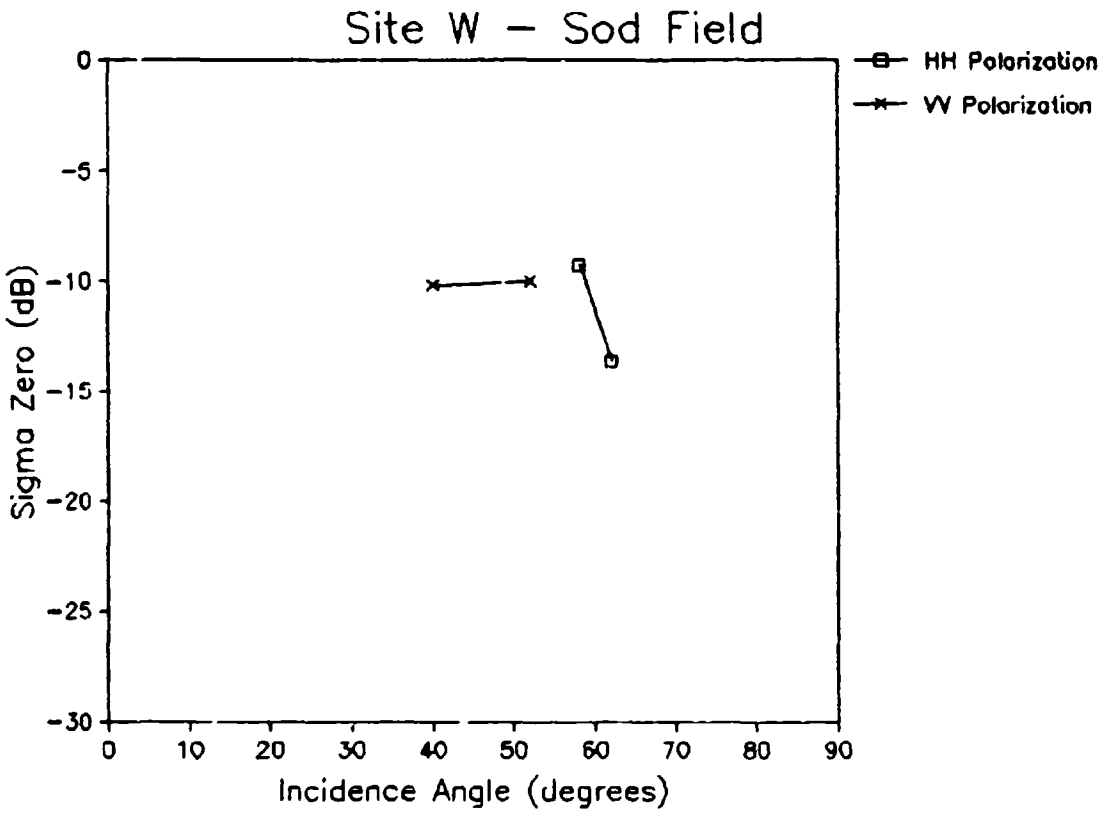

Figure 6 (g). Sod Field (Site W)

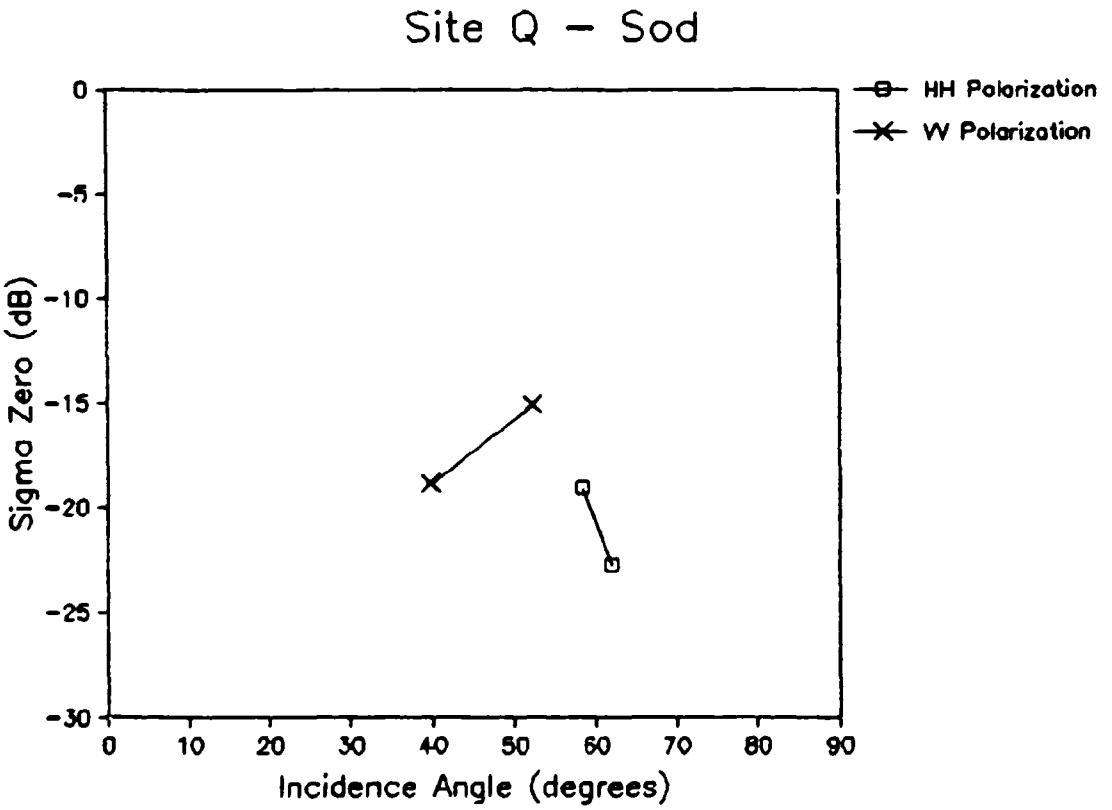

Figure 6 (h). Sod (Site Q)

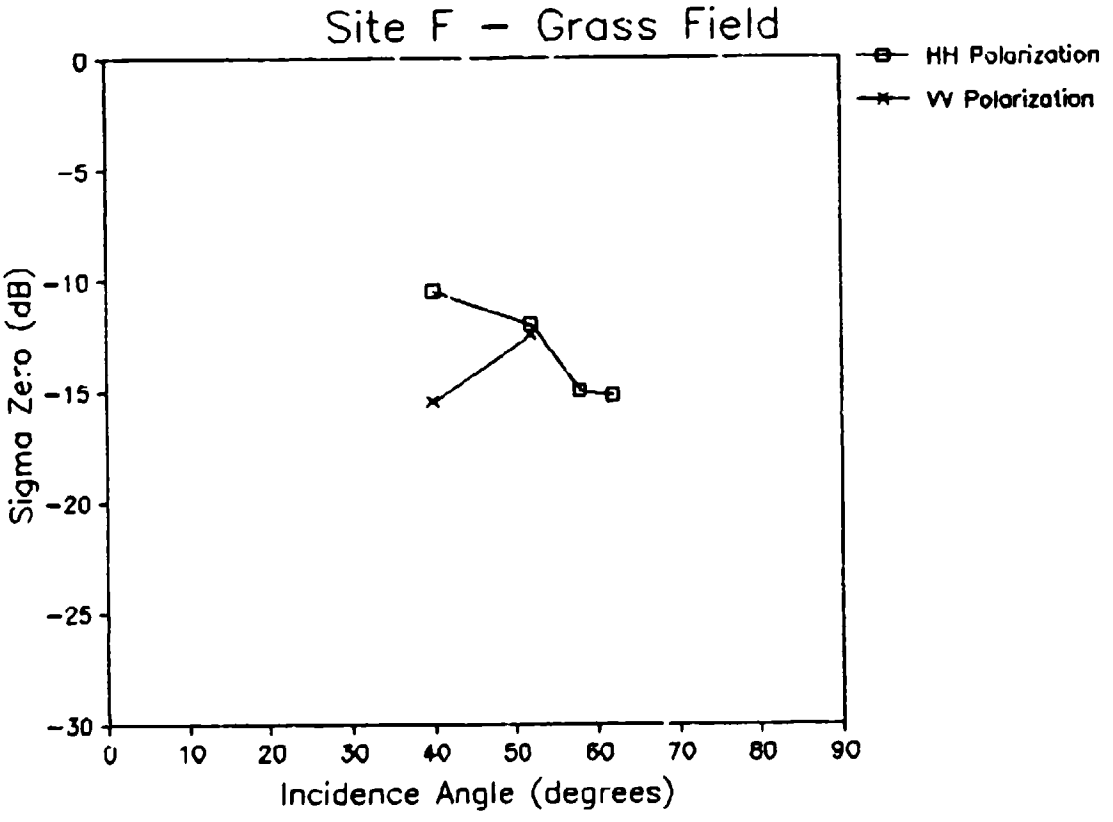

Figure 6 (i). Grass Field (Site F)

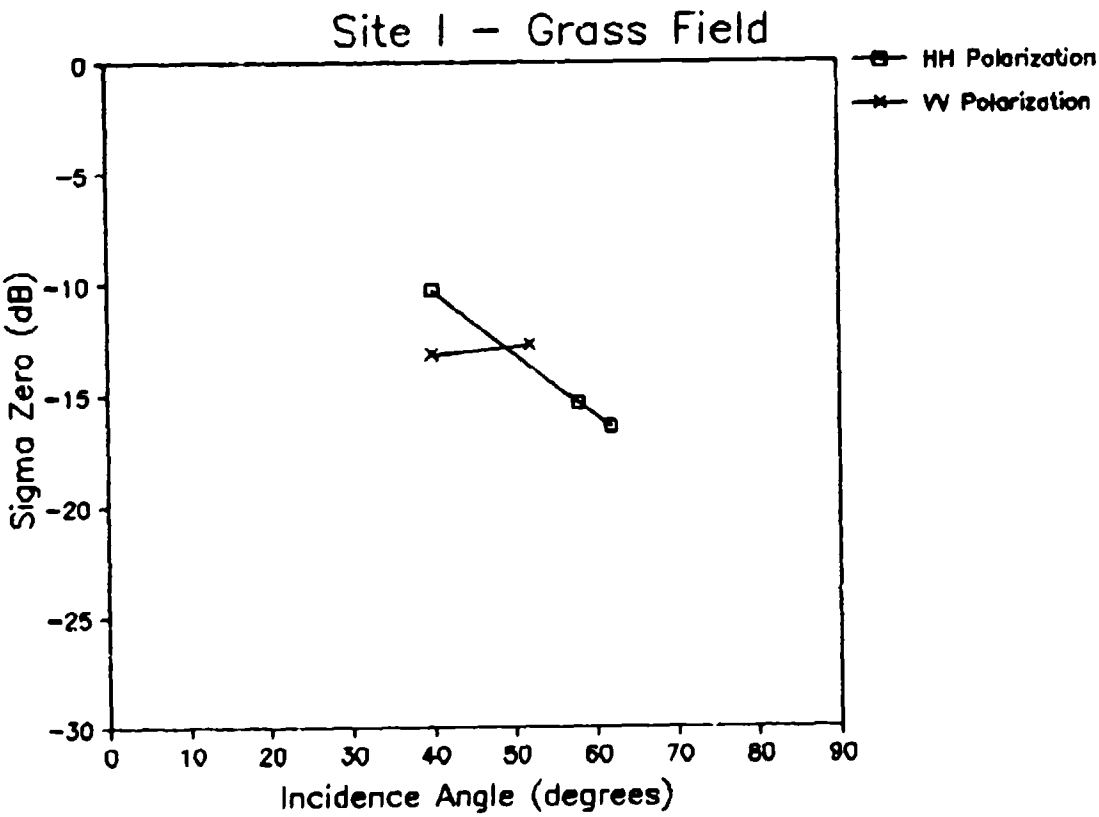

Figure 6 (j). Grass Field (Site I)

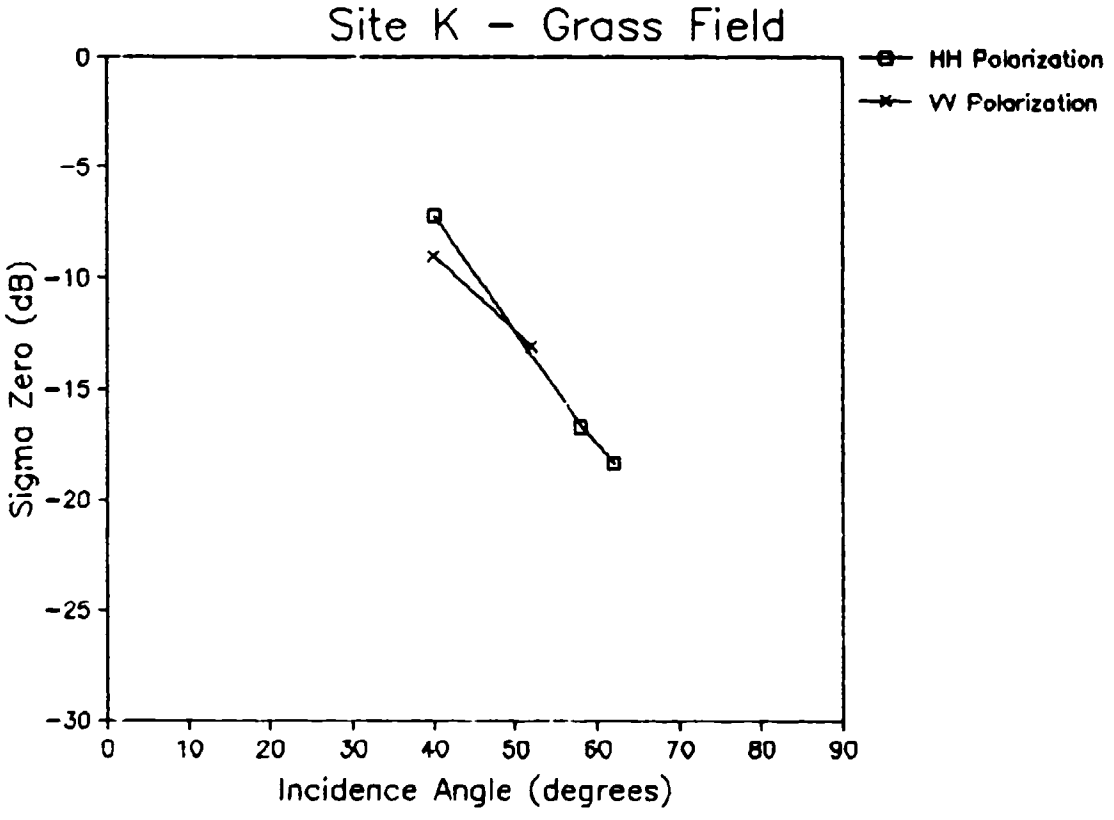

Figure 6 (k). Grass Field (Site K)

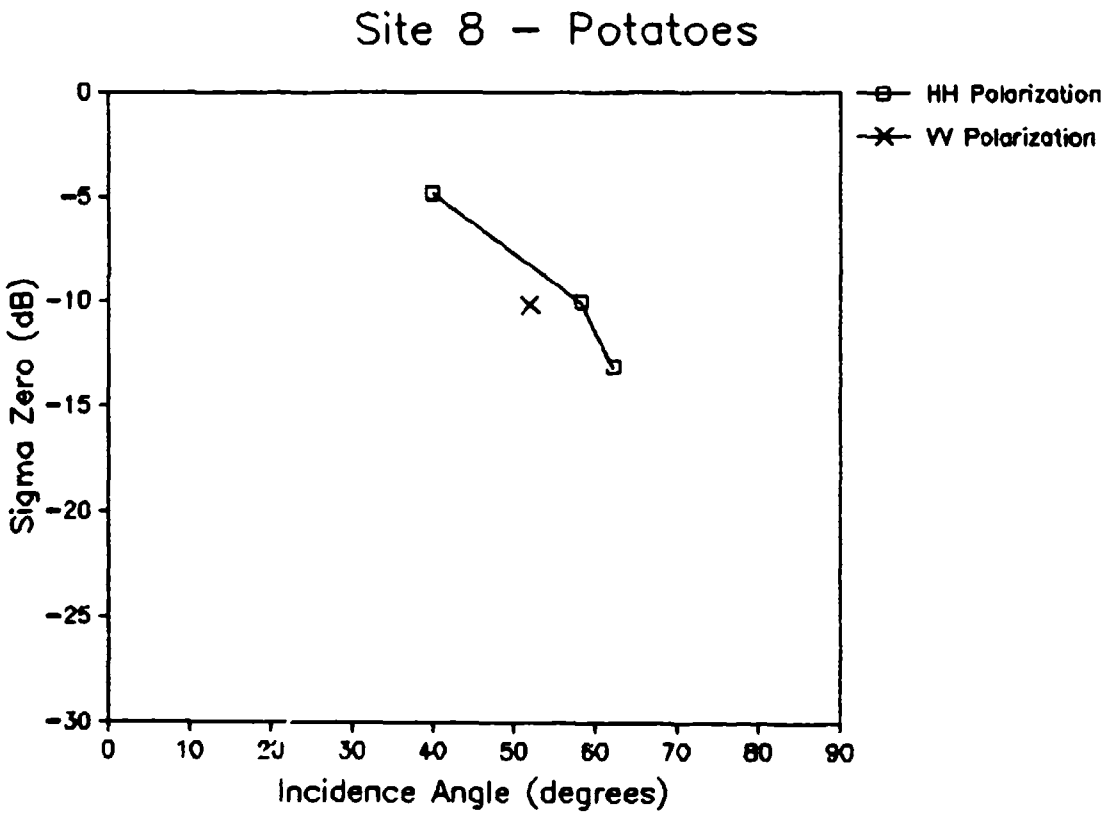

Figure 6 (1). Potatoes (Site 8)

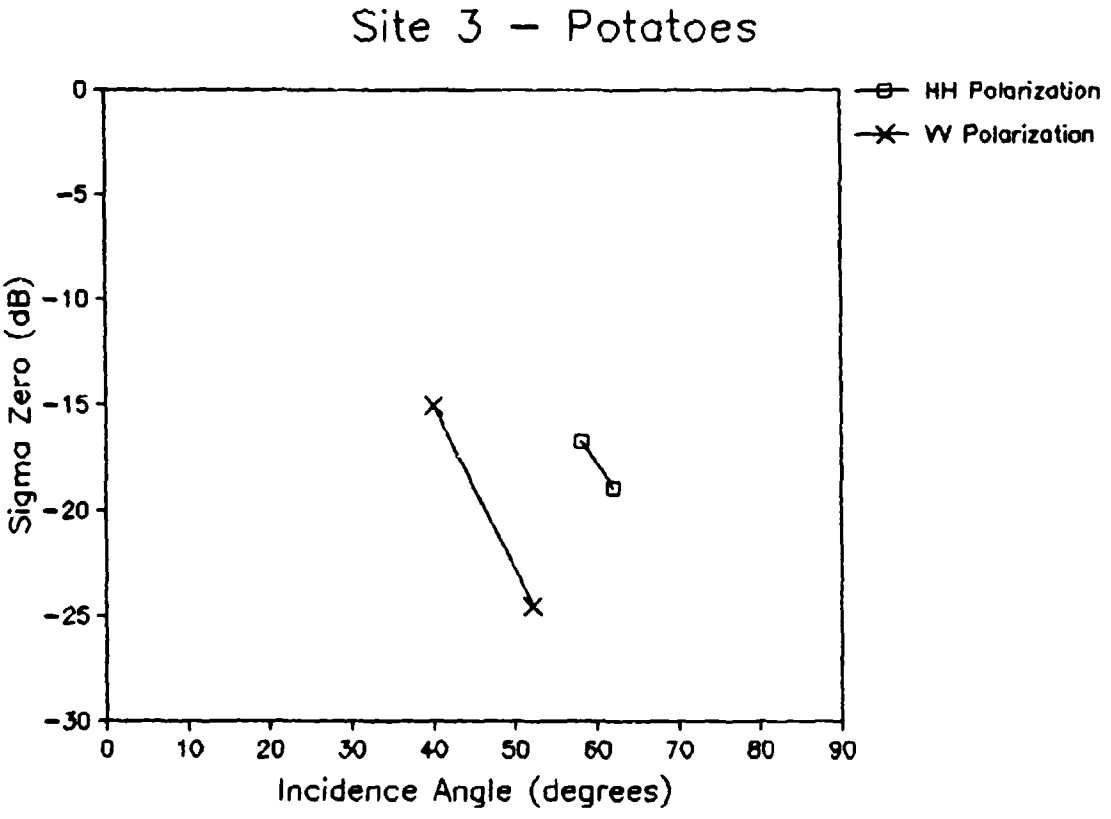

Figure 6 (m). Potatoes (Site 3)

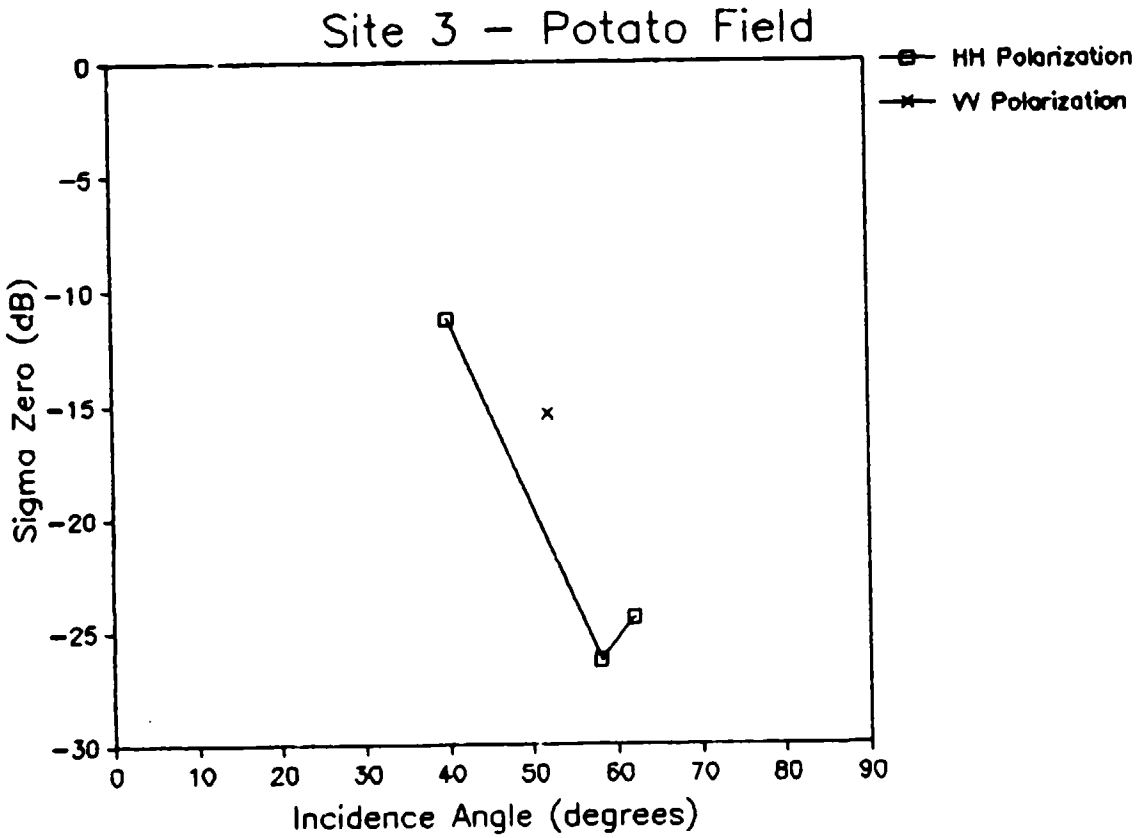

Figure 6 (n). Potato Field (Site 3)

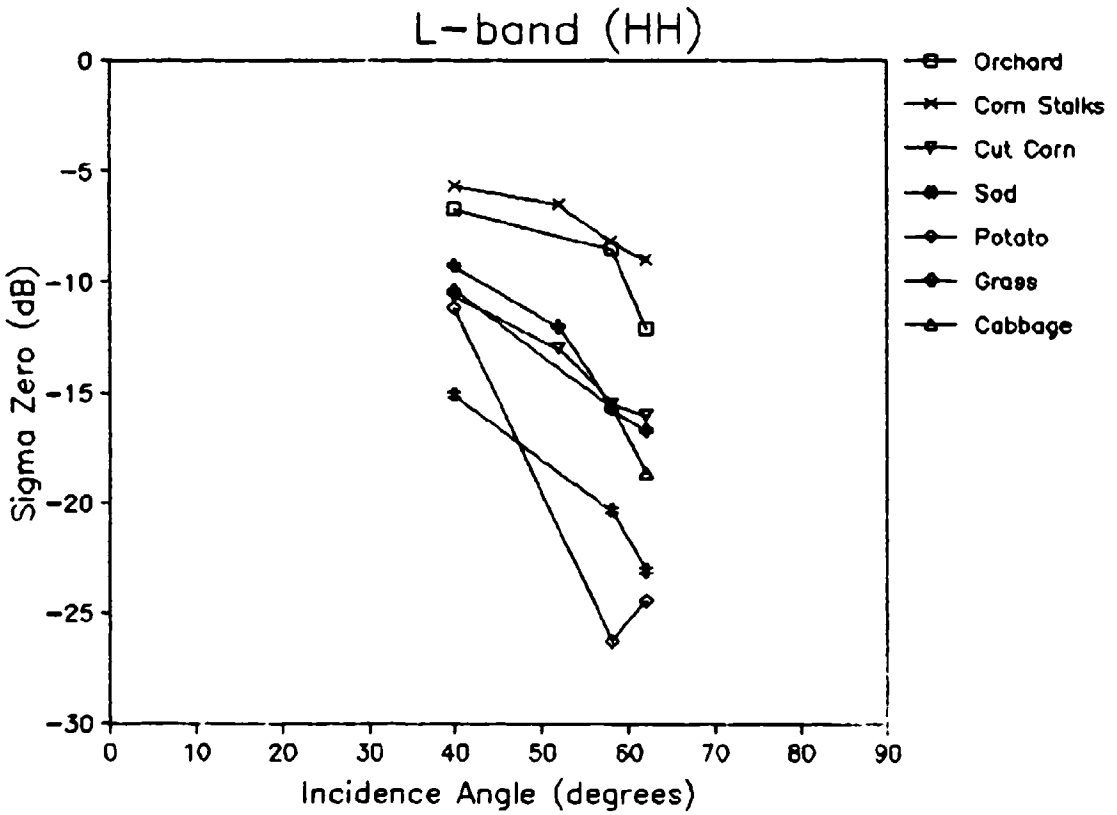

Figure 7. Composite Plots of L-band (HH) σ^{o} Values for Similar Fields

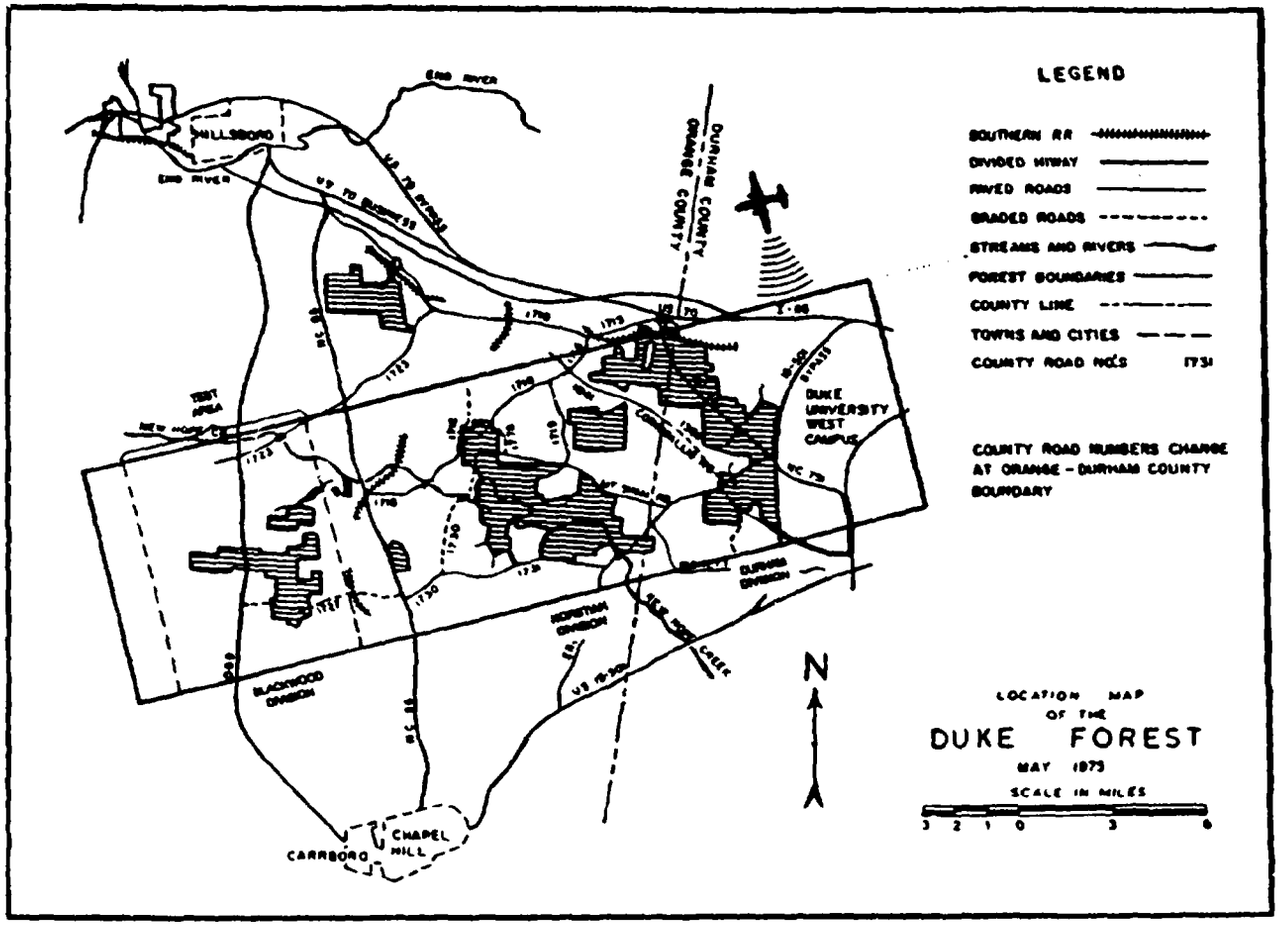

Figure 8. Major Divisions of the Duke Forest with the Approximate Ground Coverage of the USGS SAR Data Collection Flights

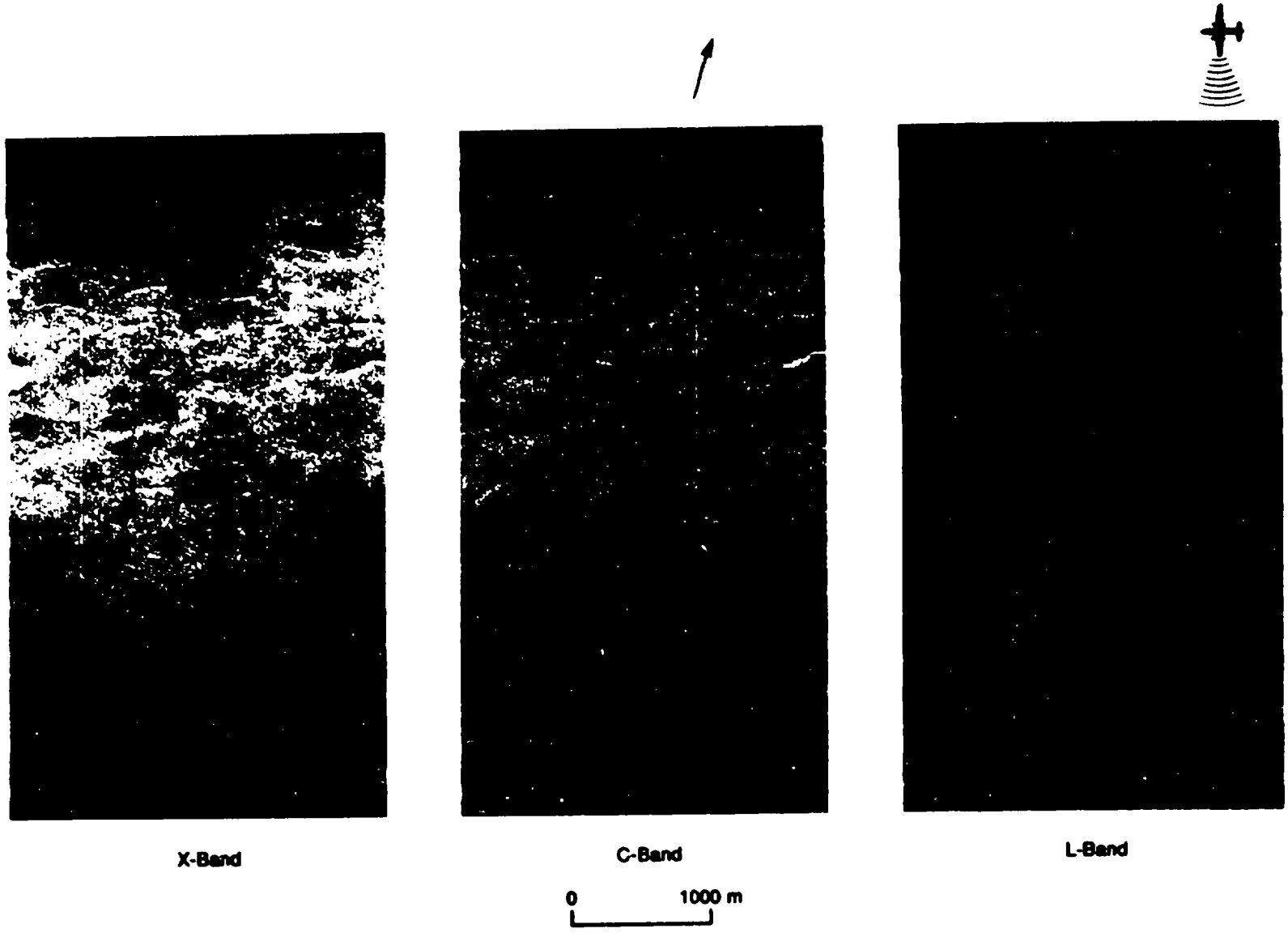

Figure 9. Digitally-Processed X-, C- and L-band SAR Data (VV polarization) Collected over the Blackwood Division of the Duke Forest

The tree stands in the Duke Forest range in size from 1 to > 50 hectares, and have been in a "forest condition" for more than 50 years. What makes this a particularly valuable test area for the evaluation of SAR imagery for forestry studies is that research records for the stands within the forest are extensive (Edeburn, 1981), with historical information on tree growth, stand age, stand density, stand mortality, etc., in existence for hundreds of permanent plots throughout the forest. In addition, the Duke Forest is the site of numerous ongoing and proposed forestry and ecological studies (see, e.g., Christensen and Peet, 1984).

For the present analysis, a 2.9 by 6.1 km area surrounding the Blackwood Division of the Duke Forest was utilized as the primary test area. Figure 10 is a mosaic of 1:9600 scale black and white aerial photographs which contains the Blackwood Division. The aerial photography was collected in January, 1985, nine months after the SAR data collection. Figure 11 presents a vegetation map of the Blackwood Division of the Duke Forest which was generated using a combination of existing forest cover maps (Edeburn, 1981), ground truth collected at the time of the SAR overflights, and the aerial photography presented in Figure 10. A point of reference for all the images and maps presented in this paper is the large grass field (site B9) located in the center of a recent clearcut area of the Blackwood Division.

A secondary test area outside of the Blackwood Division, which contained a forest stand located along a stream which was flooded during the SAR overflights, was also used in this study. An enlargement of the SAR imagery from this secondary test area is presented in Figure 12.

Twenty-two test sites were identified within the two test areas (see Table 3 and Figure 10). These test sites can be divided into the following basic categories:

Young Pine (Figure 13a): A three year old stand of loblolly pine (P.taeda), 1.2 m in height (site B8).

Figure 10. Aerial Photographic-Mosaic Collected over the Blackwood Division of the Duke Forest

COVER TYPES

CONIFER TYPES

L LOBLOLLY PINE

S SHORTLEAF PINE

V VIRGINIA PINE

LS LOBLOLLY PINE - SHORTLEAF PINE

SV SHORTLEAF PINE - VIRGINIA PINE

LV LOBLOLLY PINE - VIRGINIA PINE

M MISCELLANEOUS CONIFER

HARDWOOD TYPES

A RED GUM - YELLOW POPLAR

B RIVER BIRCH - SYCAMORE

C WHITE OAK - BLACK OAK - RED OAK

D POST OAK - BLACKJACK OAK

E MISCELLANEOUS HARDWOOD

AO RED GUM - YELLOW POPLAR - OAK

PINE - HARDWOOD TYPES

LO LOBLOLLY PINE - OAK

SO SHORTLEAF PINE - OAK

VO VIRGINIA PINE - OAK

LA LOBLOLLY PINE - RED GUM

SA SHORTLEAF PINE - RED GUM

LE LOBLOLLY PINE - MISCELLANEOUS HARDWOOD

MO MISCELLANEOUS CONIFERS - OAKS

NF NON-FORESTED LAND AND RESERVED LAND

AGE CLASSES

PINE TYPES

0	1 - 10 YEARS
1	11 - 20 "
2	21 - 30 "
3	31 - 40 "
4	41 - 50 "
5	51 - 60 "
6	61 - 70 "
7	71 - 80 "
8	81 - 90 "
9	91 - 100 "
10	101 - 110 "
11	111 - 120 "
U	UNEVEN - AGED

PINE - HARDWOOD AND HARDWOOD TYPES

1	1 - 20 YEARS
2	21 - 40 "
3	41 - 60 "
4	61 - 80 "
5	81 - 100 "
U	UNEVEN - AGED

Key to Figure 11

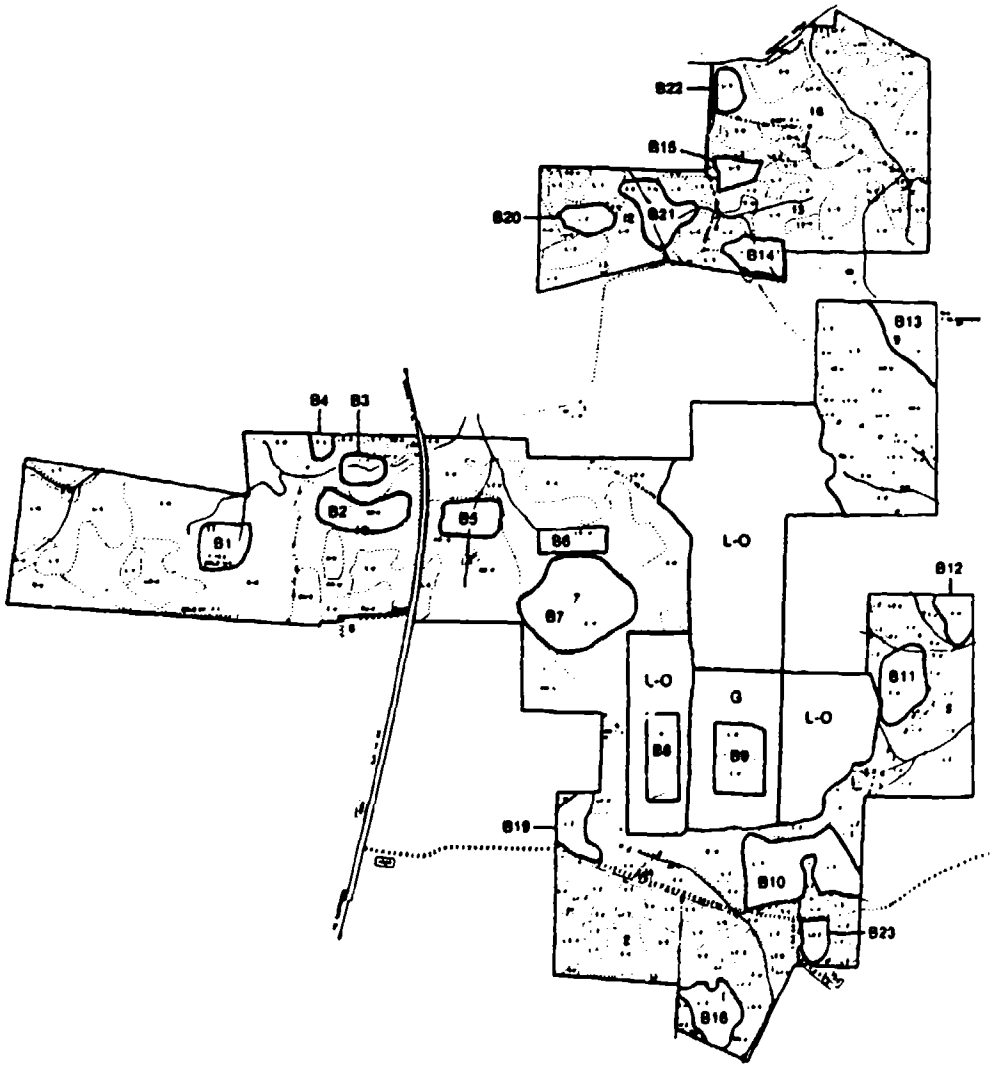

Figure 11. Forest Cover Map of Blackwood Division Test Site

X-Band

C-Band

L-Band

Figure 12. Digitally-Processed X-, C- and L-band SAR Data (VV polarization) Collected over a Flooded Forest Stand North of the Blackwood Division of the Duke Forest

TABLE 3
DUKE FOREST TEST SITES

			CONFIGEROUS SPECIES				DECIDOUS SPECIES			
SITE	TREE TYPE	AGE	STEMS/ ha	DBH (cm)	BASAL AREA (sq m/ha)	HEIGHT (m)	STEMS/ ha	DBH (cm)	BASAL AREA	HEIGHT (m)
B1	D	U	7	36	1	21	640	17	27	22
B2	SO	U	99	30	8	26	388	19	18	
B3	C	U					121	37	18	27
B4	S	60	121	34	11	31	1247	11	18	
B5	AO	U	10	54	2	31	472	19	22	
B6	LE	U	106	36	12	25	810	19	22	
B7	C	U	10	41	1	27	699	18	30	
B8	L	3		8		1				
B9	G	-								
B10	L	50	247	35	32	26	378	15	9	
B11	C	U	10	41	1	24	566	28	27	24
B12	D	U	104	27	7	23	299	31	30	24
B13	D	U								20
B14	L	60	170	39	21	30	729	16	24	
B15	L	40	454	31	37	27	17	41	3	
B16	L	40	437	28	28	24	284	10	3	
B18	L	30	410	22	18	20				
B19	L	30	963	24	46					
B20	L	30	531	25	28	22	79	21	5	
B21	E	U					442	22	27	28
B22	L	40	358	31	28	27				
B23	L	30	390	25	21	22	72	20	3	
B24	SSF	U								
B25	SSD	U								

TREE TYPE KEY

AO - SWEETGUM/YELLOW POPLAR
C - WHITE OAK/RED OAK/BLCK OAK
D - BLACKJACK OAK/POST OAK
E - MIXED HARDWOOD
L - LOBLOLLY PINE
LE - LOBLOLLY PINE/MIXED HARDWOOD
S - SHORTLEAF PINE
SO - SHORTLEAF PINE/OAK
SSD - SYCAMORE/SWEETGUN/LOBLOLLY-DRY SITE
SSF - SYCAMORE/SWEETGUM/LOBLOLLY-FLOODED SITE

(a) Young Pine (Site B8)

(b) Mature Pine (Site B23)

(c) Old Pine (Site B14)

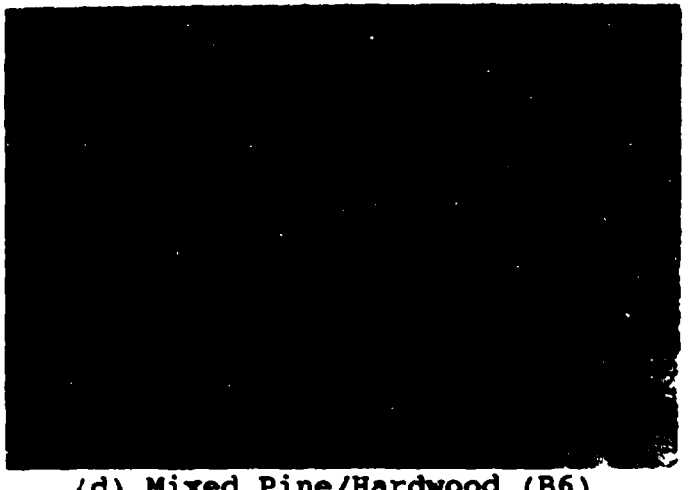

(d) Mixed Pine/Hardwood (B6)

Figure 13. Surface Photographs of the Key Forest Stand Classes in the Blackwood Division of the Duke Forest

(e) Hardwood (Site B7)

(f) Flooded Forest (Site B24)

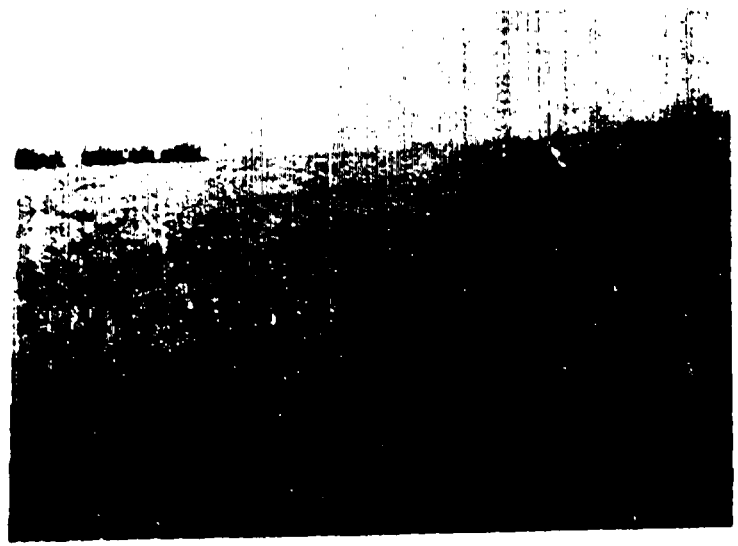

(g) Grass Field (Site B9)

Mature Pine (Figure 13b): Thirty to forty year old loblolly pine stands, with virtually no other tree species in the overstory or understory (site B23).

Old Pine (Figure 13c): 50 to 60 year old stands of loblolly pine and shortleaf pine (P. echinata), where mortality in the overstory has allowed the invasion of deciduous species (site B14).

Mixed Pine/Hardwood (Figure 13d): Stands where both pine and hardwoods are dominant overstory species (site B6).

Hardwood Stands (Figure 13e): Stands where hardwood species dominate the overstory. On drier sites, pure and mixed stands of oak prevail (Q. alba, Q. rubra, Q. velutina, Q. marilandica, Q. prinus and Q. stellata), while on moister sites, yellow poplar (L. tulipifera) and sweetgum (L. styraciflua) are the dominant species (site B7).

Flooded Stand (Figure 13f): Spring rains resulted in one stand of sycamore (P. occidentalis) and sweetgum being flooded at the time of the SAR data collection. Although the picture of this area in Figure 13f was collected at a time when the site was not in a flooded state, the water marks on the tree trunks clearly indicate that this stand is flooded at some stage during the year (site B24).

Grass Field (Figure 13g): This test site containing short (5 cm in height) grass was included as a reference for the other test sites (site B9).

The research records from the Duke Forest were reviewed, and a set of tree parameters obtained for each test site. These parameters include:

Age: The average age (usually rounded to the nearest ten years) of the trees within the stand.

items/hectare: The average number of trees per hectare greater than 10 cm in diameter within the stand.

Diameter at breast height (DBH): The average diameter of all trees within the stand measured at a height of 1.3 m above the ground level.

Basal area: The total area (in m^2) of all tree trunks (at 1.3 m above the ground) within the forest stand.

Height (m): The average height of the trees within the stand.

These parameters are summarized for the 22 test sites in Table 3. Note that the data presented in Table 3 has been divided into two groups (coniferous and deciduous species) for each test site.

Estimates of the radar scattering coefficient (σ^0) were generated for the 22 test sites using the average value from a 40 by 40 pixel subset extracted from the calibrated SAR images.

Table 4 summarizes the σ^0 values for the 22 test sites. The incidence angle (θ_i) for the test sites is 57°, except for sites B24 and B25, where it is 46°. In Table 4 the test sites have been grouped by tree type and age. For analysis purposes, the 22 test sites were organized into 13 categories. The average σ^0 values for these 13 categories are summarized in Table 5 and presented in Figure 14. The upper and lower error bounds are also presented in Figures 14a-14c. We define the upper bound (UB) being equal to the lower bound (LB) as

$$UB = LB = [r^2 + s_f^2 + SE^2]^{1/2} \qquad (2)$$

where r is the relative calibration of the SAR (1 dB), s_f is the variability due to speckle (.35 dB) and SE is the standard error of the mean defined in Eq. (1). Figure 14d presents the average σ^0 values for all three radar frequencies plotted on the same graph for comparison purposes.

From Tables 4 and 5 and Figure 14, we can make several observations. We first note that while there is a significant difference between the dry and flooded sycamore stands in the L-band (3.5 dB) and C-band (3.0 dB) imagery, there is considerably less difference in the X-band data (0.9 dB). The observation at L-band is consistent with studies conducted with satellite SARs (Krohn, et al., 1983; Ormsby, et al., 1985; Lyon and McCarthy, 1981). At C-band, no previous SAR data exists where flooded forests had been imaged. However, previous aircraft X-band SLAR imagery collected over a flooded forest canopy

TABLE 4
RADAR SCATTERING COEFFICIENTS FOR DUKE FOREST TEST SITES

TREE SITE	TYPE	AGE	SCATTERING COEFFICIENTS X-BAND	C-BAND	L-BAND
B9	G	-	-5.14	-5.50	-16.34
B8	L	3	-1.33	-3.30	-13.39
B19	L	30	-3.11	-3.97	-10.98
B20	L	30	-1.75	-5.17	-11.61
B23	L	30	-1.26	- .41	-11.58
B15	L	40	-2.88	-3.51	-12.12
B16	L	40	-3.00	-3.58	-10.80
B22	L	40	-4.43	-3.05	-11.02
B10	L	50	-4.43	-3.05	-11.02
B4	S	60	-2.22	-4.51	-13.05
B14	L	60	-1.84	-4.76	-11.58
B2	SO	U	- .64	-3.26	-11.36
B6	LE	U	- .74	-3.67	-11.29
B1	D	U	- .01	-2.73	-11.03
B12	D	U	-3.13	-3.47	-11.21
B13	D	U	- .73	-3.23	-11.67
B3	C	U	- .64	-3.60	-11.41
B7	C	U	- .18	-2.56	-10.62
B11	C	U	-3.15	-3.55	-10.97
B5	AO	U	-1.30	-2.77	-11.28
B21	E	U	- .47	-4.06	-11.60
B24	SSF	U	- .95	-1.47	- 8.12
B25	SSD		-1.78	-5.14	-11.62

TREE TYPE KEY

AO - SWEETGUM/YELLOW POPLAR
C - WHITE OAK/RED OAK/BLCK OAK
D - BLACKJACK OAK/POST OAK
E - MIXED HARDWOOD
L - LOBLOLLY PINE
LE - LOBLOLLY PINE/MIXED HARDWOOD
S - SHORTLEAF PINE
SO - SHORTLEAF PINE/OAK
SSD - SYCAMORE/SWEETGUN/LOBLOLLY-DRY SITE
SSF - SYCAMORE/SWEETGUM/LOBLOLLY-FLOODED SITE

TABLE 5
MEANS AND STANDARD DEVIATIONS OF DUKE FOREST
RADAR CROSS SECTION VALUES

SITE	N		X-BAND	C-BAND	L-BAND
GRASS FIELD	1		-9.11	-0.47	-16.34
3 YR PINE	1		-5.31	-7.28	-13.39
30 YR PINE	3	MEAN	-6.07	-7.21	-11.39
		SD	.95	2.60	.29
40 YR PINE	3	MEAN	-6.62	-8.10	-11.67
		SD	.66	.88	.62
50 YR PINE	1		-8.36	-6.98	-11.02
60 YR PINE	2	MEAN	-6.19	-8.79	-12.31
		SD	.23	.22	.73
HARDWOOD/PINE MIX	3	MEAN	-4.87	-7.55	-11.32
		SD	.06	.28	.03
CHESTNUT OAK	3	MEAN	-5.37	-7.22	-11.30
		SD	1.30	.22	.27
MIXED OAK	3	MEAN	-5.35	-7.22	-11.00
		SD	1.29	.52	.32
YELLOW POPLAR/SWEETGUM	1		-5.39	-6.86	-11.29
MIXED HARDWOODS	1		-4.68	-8.26	-11.60
DRY SYCAMORE	1		-6.37	-9.72	-11.62
FLOODED SYCAMORE	1		-5.60	-6.12	- 8.12

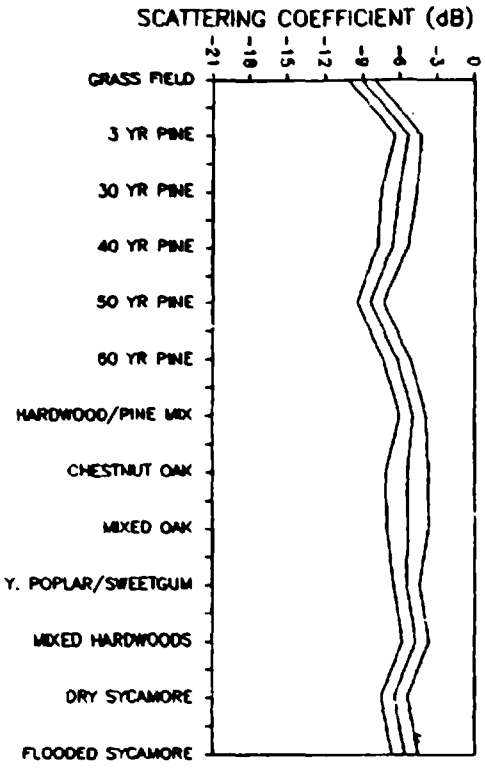

(a) X-band Data

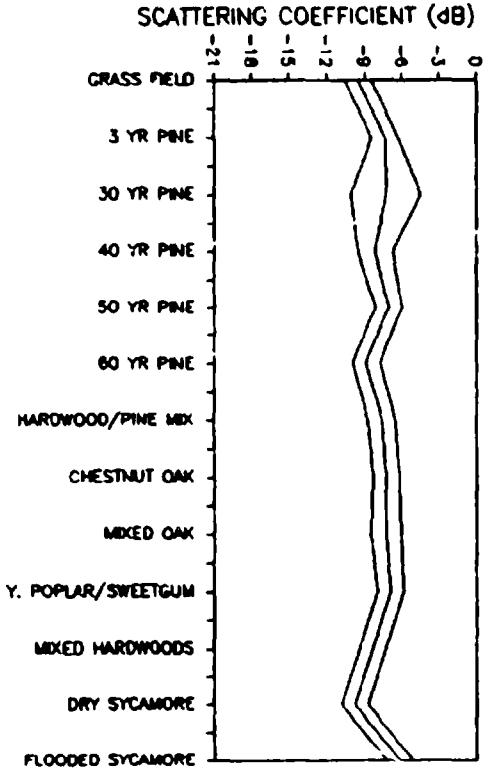

(b). C-band Data

Figure 14. Radar Scattering Coefficients and Error Bounds for 13 Different Forest Stands from the Duke Forest Blackwood Division [Figures (a) through (d)]

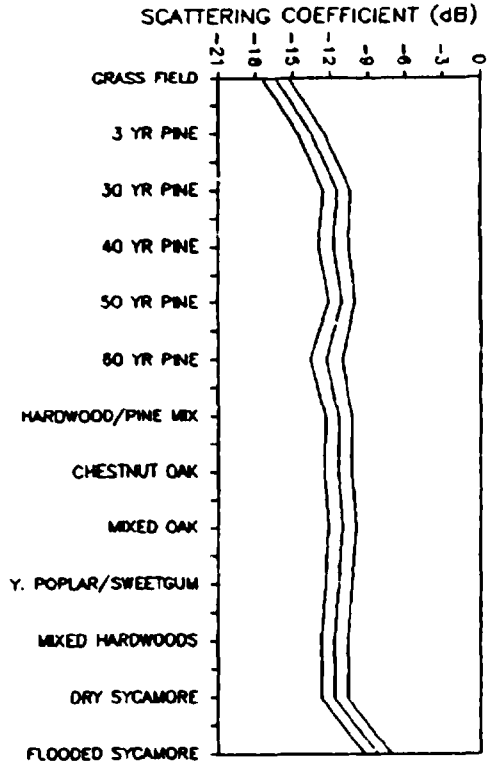

Figure 14 (c). L-band Data

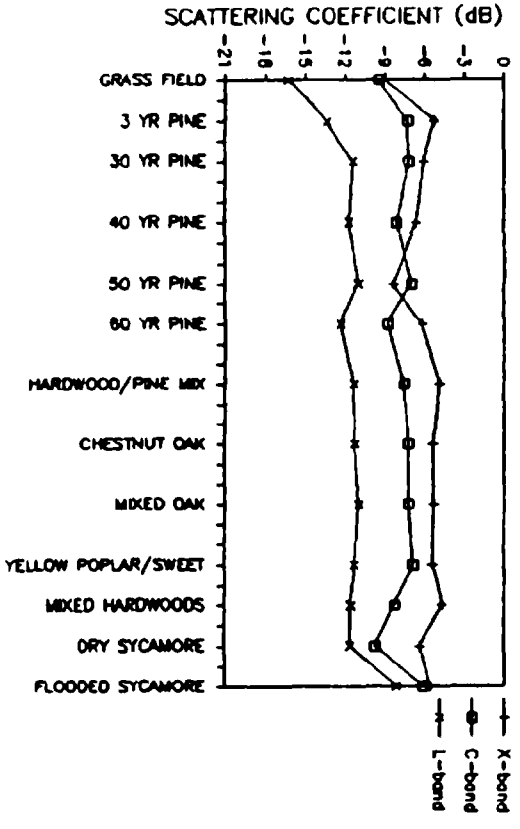

Figure 14 (d). Comparison of X-, C- and L-band Data

(Ormsby, et al., 1985) revealed no significant difference from adjacent unflooded canopies.

The second observation we can make from the SAR forestry data concerns the ranges of radar scattering coefficients observed over different forest stands. In this analysis, we consider only those sites from the same incidence angle range with full canopies (i.e., all sites in Table 4 except B8, B9, B24, B25). If we consider the average values presented in Table 5, the range of observed σ^0's at X-band is 3.4 dB, at C-band, 2.3 dB, and L-band, 1.3 dB. If we consider all the values, as presented in Table 4, then the range of scattering coefficients for mature, dry forests is 4.2 dB at X-band, 4.8 dB at C-band and 2.8 dB at L-band. Thus, the highest range of radar responses for forest canopies occurs at the higher radar frequencies (X and C-band).

2.3 ATLANTIC OCEAN TEST SITES

A considerable amount of calibrated L-band (HH) SAR imagery was collected over open ocean regions during the 1984 SARSEX experiment. In this section, we will present L-band scattering coefficients from three passes collected during this mission.

Computer programs have been developed to extract calibrated radar scattering cross-section (σ) or scattering coefficient σ^0) measurements from airborne SAR imagery. The SAR calibration algorithm developed by Larson, et al. (1987) has been coupled with an algorithm which allows for scanning along any track in any direction within the SAR scene. This computer program allows for the operator to select: (1) scan direction, (2) number of pixels for averaging in the cross-track direction, and (3) number of pixels for averaging in the along-track direction. The algorithm outputs a plot with either slant or ground range as the X-axis and relative or absolute σ or σ^0 as the Y-axis.

The tracks of the surface vessels collecting the ocean measurements during SARSEX were always oriented perpendicular to the propagation direction of the internal waves. Thus, the scans extracted from the SAR images were oriented so they were parallel to the ship's track, with the center of the scan coincident with the ship's position in the SAR image. To generate these scans, a window of 150 m in the cross-track direction and 22 m in the along-track direction was used. The number of pixels or independent samples used to generate each σ^0 measurement leads to a maximum $\pm$ 0.55 dB uncertainty (90% confidence interval) in the resultant σ^0 value due to image speckle or fading (Ulaby, et al., 1982).

The data used in this analysis was collected during three separate passes: SARSEX-4, Pass 5; SARSEX-5, Pass 9; and SARSEX-8, Pass 4. Figure 15 presents the σ^0 scans for these three passes. The incidence angle ranges for these data sets was from 25^0 to 56^0. We can see that the overall σ^0 level for the three passes was fairly constant with respect to wind speed, but there is a noticeable fall- off in σ^0 as incidence angle decreases. This fall-off is approximately 0.25 dB per degree in incidence angle. The observed fall-off matches model predicted values quite well (Lyzenga and Bennett, 1987; Kasischke, et al., 1987).

2.4 FRAM STRAIT ICE TEST SITES

L-band (HH) radar scattering coefficient (σ^0) values were extracted from airborne SAR imagery collected during the MIZEX experiment. In order to calibrate this data set, the L-band SAR image intensities were compared to helicopter-borne scatterometer measurements collected near-coincidently with the SAR data (Onstott and Larson, 1986).

Table 6 summarizes the L-band (HH) σ^0 values. (Burns, 1987) All data were collected at an incidence angle of 35^0. Note that in this case, the σ^0 value from the open water test site is -32.5 dB,

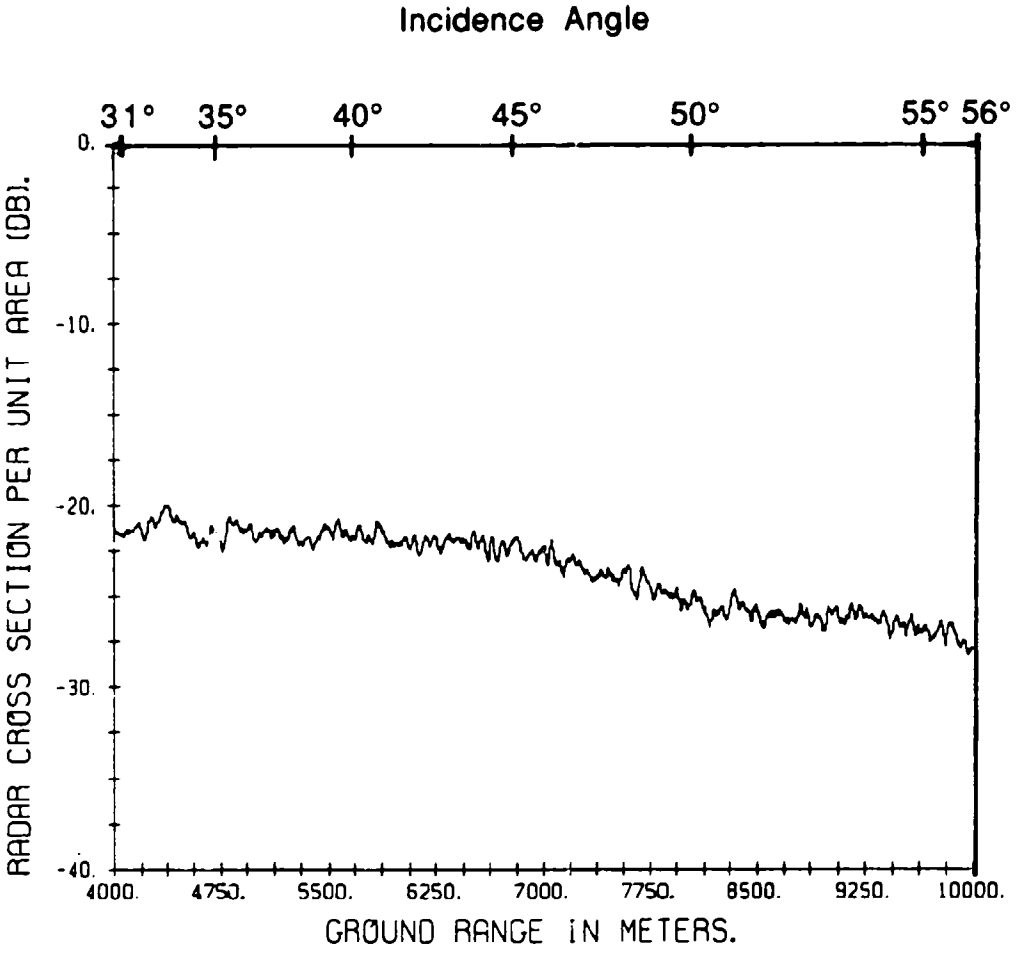

(a) SARSEX-4, Pass 5 (9 knot wind)

Figure 15. L-band (HH) Radar Scattering Coefficients (σ^{o}) for Ocean Surface Areas [Figures (a) through (c)

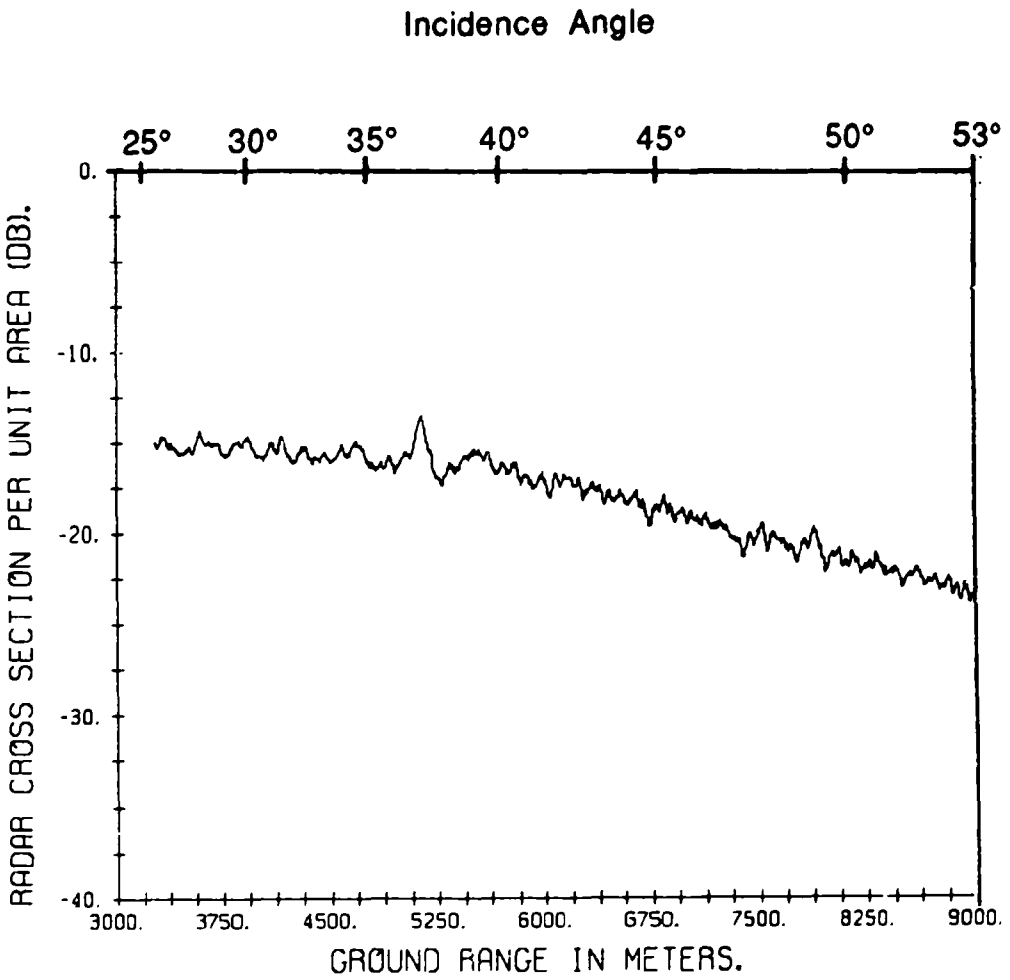

Figure 15 (b). SARSEX-5, Pass 9 (7 knot wind)

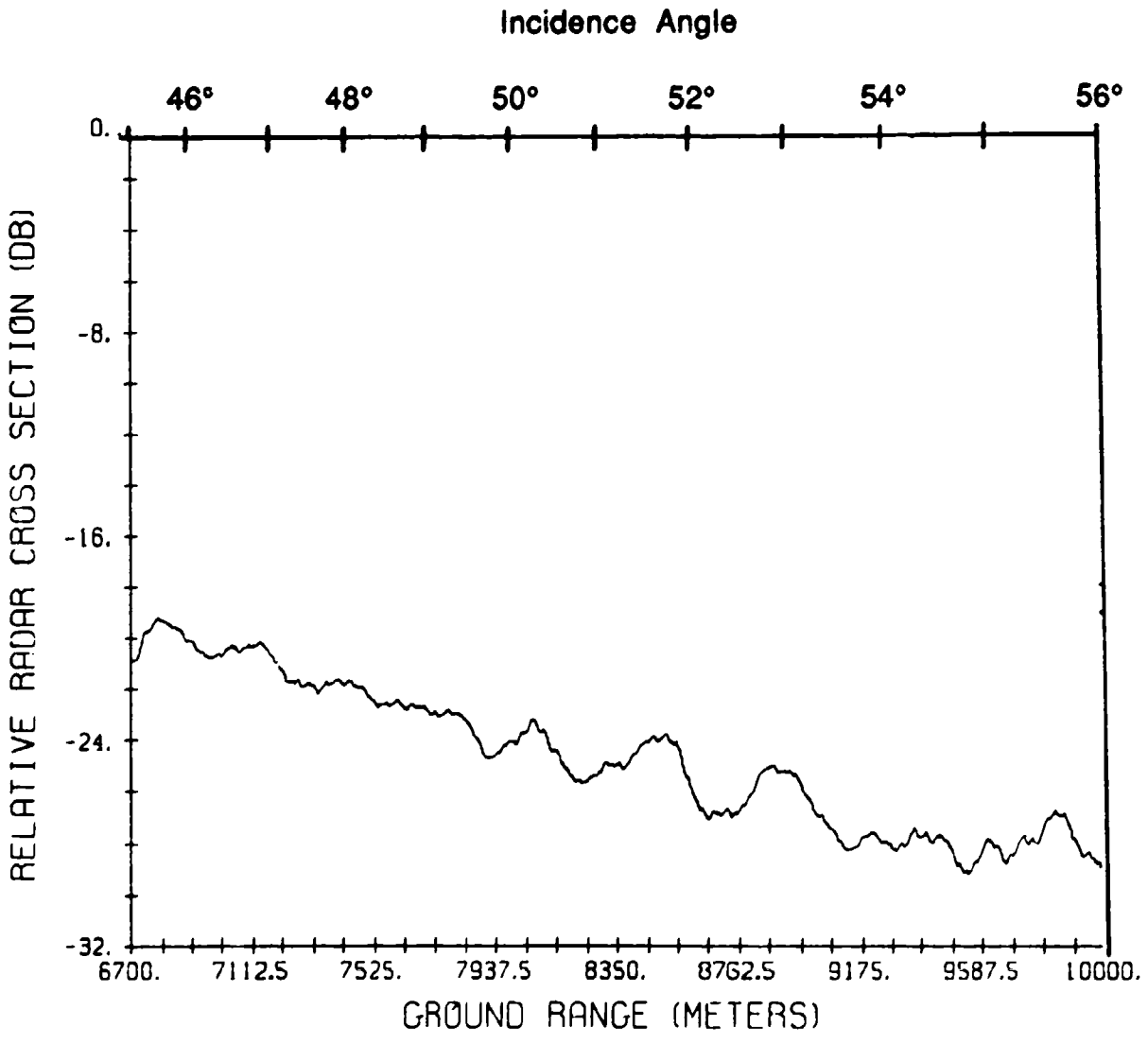

Figure 15 (c). SARSEX-8, Pass 4 (16 knot wind)

TABLE 6
SUMMARY OF RADAR SCATTERING COEEFICIENT (σ^o)
VALUES FOR THE FRAM STRAIT TEST SITE

TEST SITE	^{o} VALUE (dB)
Open Water	-32.5
Brash Ice	-21.5
Thin First Year Ice	-25.0
Medium First Year Ice	-25.0
Heavy Snow Cover	-27.5
Pressure Ridge	-25.5
Multiyear Ice with Snow	-26.0
Multiyear Ice with Melt Pools	-22.5

approximately 15-20 dB lower than the values observed over the SARSEX test areas. Surface observations of the open water areas in the MIZEX scenes showed that the water surface was extremely calm, with no surface capillary waves present. The data in Table 6 clearly illustrate the wide range of σ^o values present in data collected over Arctic regions.

3
DENSITY DISTRIBUTIONS ON SAR DATA

The distribution of the recorded intensities on synthetic aperture radar (SAR) imagery is the result of radar fading (resulting in SAR image speckle) and the distribution of the scatterers within the area imaged by the SAR. The radar fading dominates the spatial patterns present on an image unless steps are taken to reduce its influence. Two techniques are commonly used to reduce SAR image speckle. Non-coherent integration or multiple-looking is achieved by processing separate portions of the SAR bandwidth independently, and then averaging these separate sub-images to form the desired output image (Porcello, et al., 1976). The second technique simply involves averaging a number of pixels together after the SAR image has been formed. Both of these methods reduce the speckle or fading in a SAR image at the expense of spatial resolution. These methods also reduce the amount of textural information available from tne SAR data.

To better understand the characteristics of the intensity distributions on SAR data collected over distributed targets, an analysis was performed where the observed intensity distributions from airborne SAR imagery were compared to those predicted by three mathematical functions. The functions evaluated were: the Gamma distribution, the Inverse Gaussian distribution, and the Log Normal distribution.

The SAR data from each test site was first digitally processed into imagery, and corrected for antenna gain and range fall-off variations. No multiple-looking was performed during the processing of the SAR data.

An 80 by 80 pixel subset was extracted from each test site listed in Table 7 for each SAR channel. Every other pixel was discarded from this initial sample so that each pixel was independent from its

TABLE 7
SAR IMAGE INTENSITY DISTRIBUTION STUDY TEST SITES

SAR MISSION	TEST SITE	DESCRIPTION
U.S.G.S	G1	Grass Field
	G2	3 Year Old Pine
	G3	30 Year Old Pine
	G4	50 year Old Pine
	G5	Mixed Oaks
	G6	Sweetgum/Yellow Popular
SARSEX	S1	Sea Surface, 7 kt wind
	S2	Sea Surface, 16 kt wind
	S3	Grass Field
	S4	Potato Field
	S5	Unharvested Corn Field
	S6	Harvested Corn Field
	S7	Mixed Deciduous Forest
MIZEX	M1	First Year Ice
	M2	Second Year Ice

neighbors. From these original samples, eight additional data sets were generated by spatially averaging between 2 and 9 adjacent pixels. Thus, for each original 80 by 80 pixel data set, we now have nine subsets, with the number of independent samples, N, equal to 1, 2, 3, 4, 5, 6, 7, 8, and 9.

3.1 SAR IMAGE INTENSITY MODELS

The Gamma distribution can be formulated as

$$f(x) = [(x/b)c^{-1}\ e^{-x/b}]/[b\Gamma(c)] \tag{3}$$

where x is a given value within the population, $\Gamma(c)$ is the Gamma distribution evaluated at c, and b and c are defined as

$$b = s^2/\bar{x} \tag{4}$$

$$c = \bar{x}^2/s^2 \tag{5}$$

where $\bar{x}$ is the mean value for all x's in the sample and s is their standard deviation. The Gamma distribution is used to model radar fading for power measurements where no background variation is present. In this case, c = N, where N is the number of independent samples averaged to form the radar data set.

The Inverse Gaussian distribution can be formulated as

$$(x) = \{\lambda/[2m(x-a)^3]\}^{1/2} \cdot \exp\{-\ [x-\sigma-u]^2/[2u^2(x-\sigma)]\}, \tag{6}$$

where

$$a = \bar{x}_1 - (x - x_1)^3/(2s^2 \log n), \tag{7}$$

x_1 is the minimum value of x in the sample,

$$u = \bar{X} - \alpha, \tag{8}$$

and

$$\lambda = [(1/n)\ \Sigma\ (x_i - \alpha)^{-1} - (1/u)]^{-1}. \tag{9}$$

Eqs. (7-9) use the sample data set to generate the necessary parameters for the Inverse Gaussian distribution in Eq. (6).

The Log Normal distribution can be formulated as

$$f(x) = \{1/[(x-\alpha)\sigma\ \mathrm{sqrt}(2\pi)]\}\exp\{-0.5[\ln((x-\alpha)/m)]/\sigma)^2\}, \tag{10}$$

where

$$\sigma = \text{standard deviation (ln x)}, \tag{11}$$

$$m = e^U, \tag{12}$$

with

$$U = \text{mean (ln x)}. \tag{13}$$

Again, Eqs. (11-13) use the data set to generate the necessary parameters for the Log Normal Distribution described by Eq. (10).

The parameters defined by Eqs. (4,5,7-9,11-13) are maximum likelihood estimates described by Cheng and Amin (1981) and Folks and Chhikara (1978).

In order to determine whether or not a derived Gamma, Inverse Gaussian or Log Normal Distribution matched the sample population, a non-parametric statistical test was applied. The type selected for this analysis was the Kolmogorov test described by Conover (1981).

This test operates by comparing the maximum vertical separation between the sample distribution and a candidate distribution [e.g., in our case, Eqs. (2,5,9)] with a Kolmogorov test statistic (K). The Kolmogorov test statistic is based on the number of points in the sample population (N) and the level of significance. For a 95% level of significance, this statistic is

$$K = 1.36/N^{1/2} \tag{14}$$

This test statistic is used by comparing the cumulative distribution functions of the candidate and sample distributions. Figure 16 presents a plot of the CDF for test site S3, along with the Inverse Gaussian and Log Normal distribution fits for this data set. Figure 17 presents plots of the differences between the actual data and these two distributions. The K-parameter for this example is $\pm$ 0.04. Thus, we can see that both the Inverse Gaussian and Log Normal distributions adequately model the observed intensity distributions for this test site.

Cumulative distribution functions for all three speckle models were generated for all test sites for sample numbers N = 1 to 9 using the maximum likelihood estimates. The predicted CDFs were then compared to the CDFs from the actual SAR data.

Surprisingly, in all cases, all three speckle models generated distributions which matched the SAR data using the Kolmogorov goodness of fit test. Overall, the best fit was achieved using the Gamma distribution. In the next section, we will discuss how the relationship between N and the c-parameter generated using Eq. (5) can be used to estimate the texture within the SAR scene.

3.2 TEXTURE MODEL

The variability in the intensities recorded on a SAR image is due to two factors: (1) radar fading or speckle; and (2) the natural

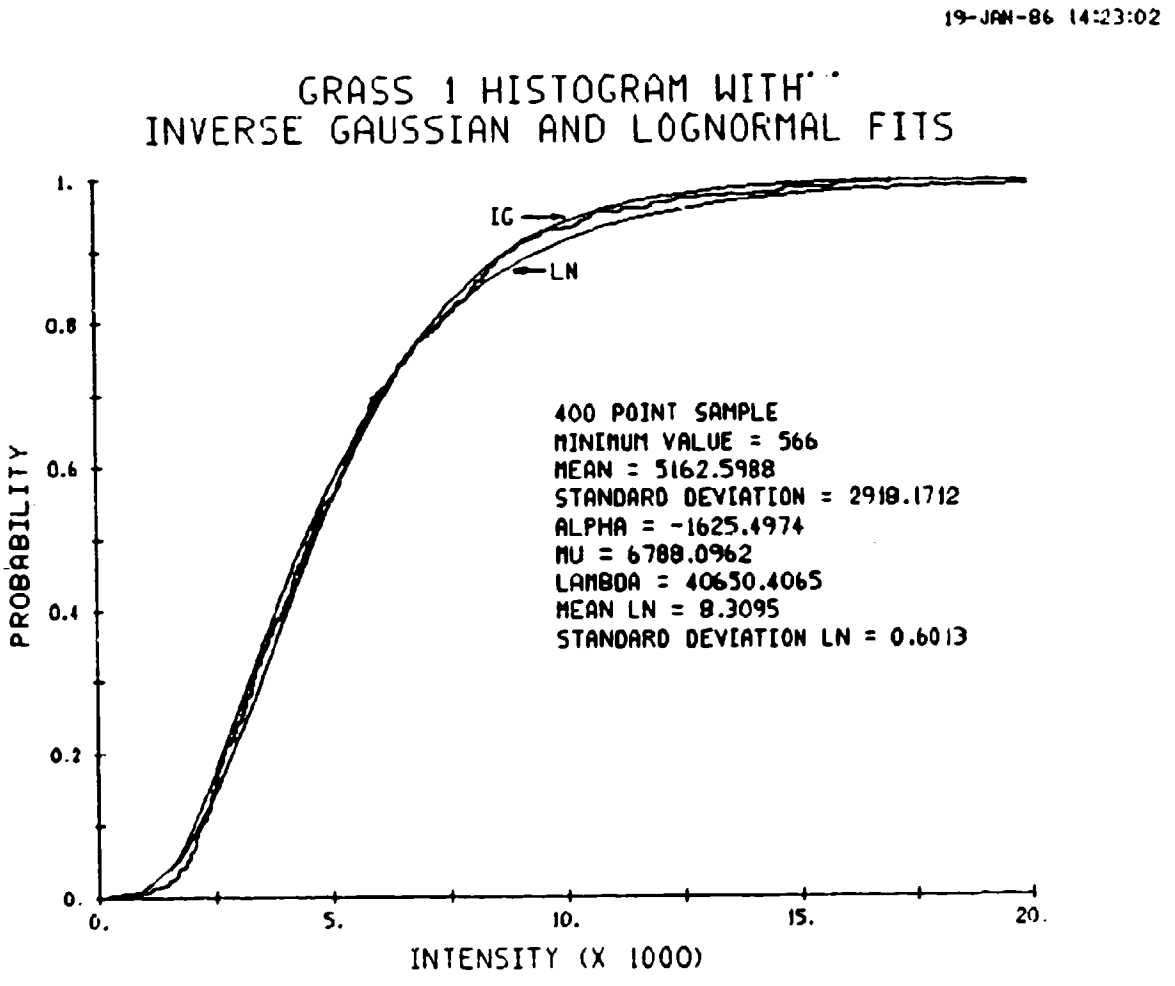

Figure 16. Cumulative Distribution Function (CDF) for Test Site S-3 with Inverse Gaussian and Log Normal Fits

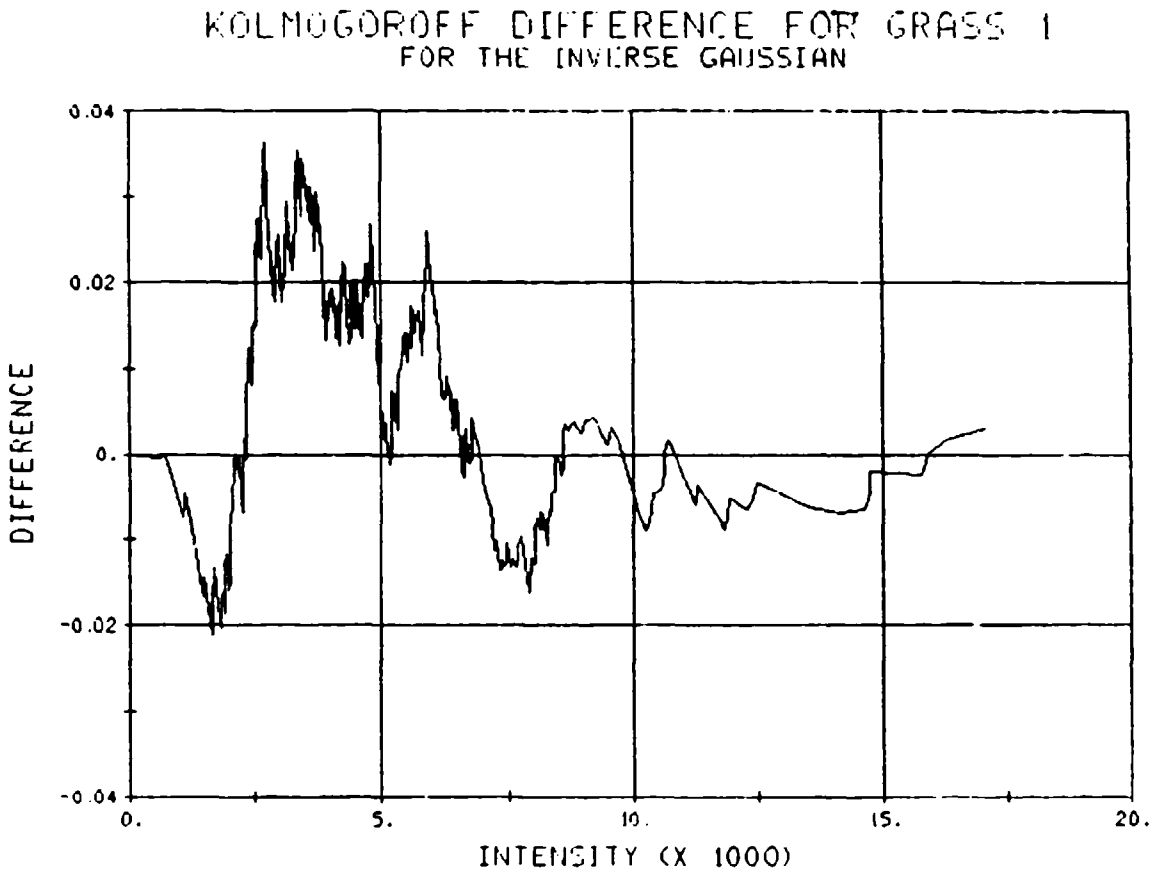

(a) Inverse Gaussian

Figure 17. Kolmogoroff Difference Plots for Test Site S3 [Figures (a) and (b)]

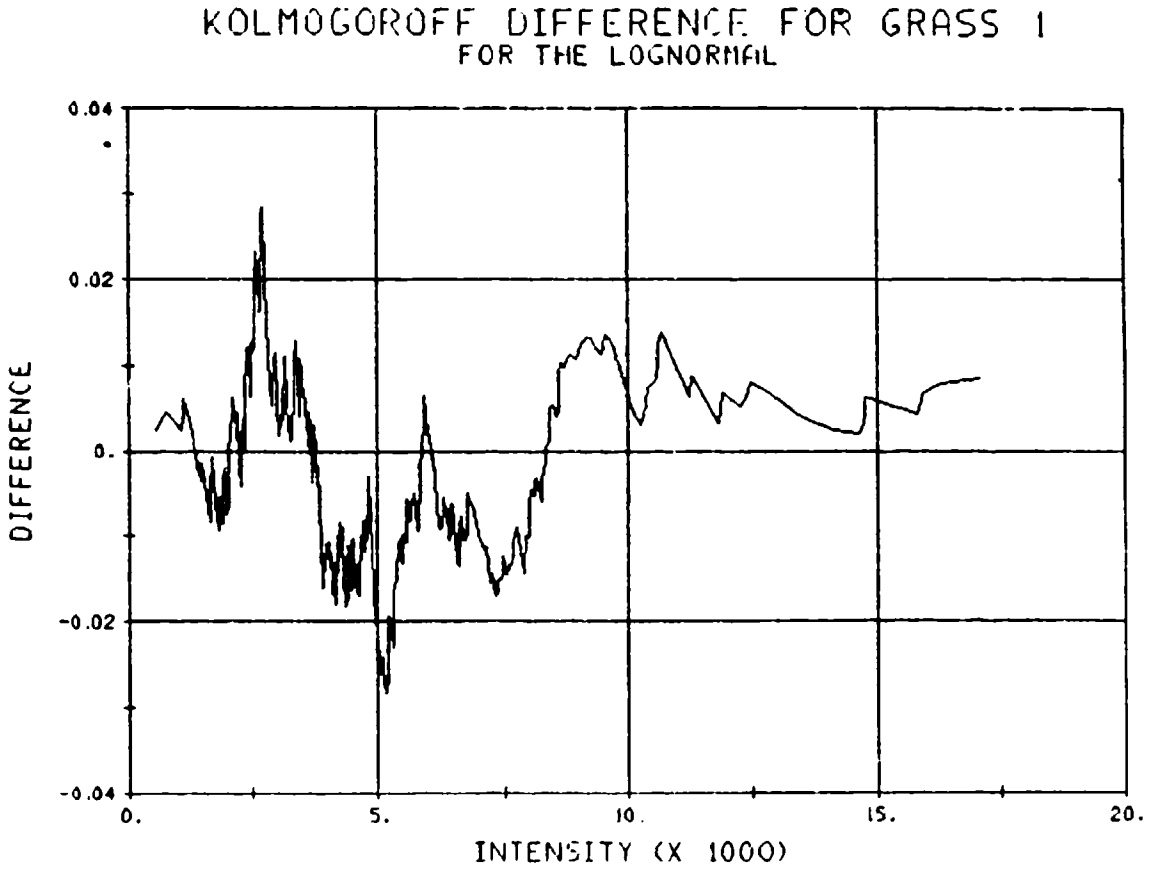

Figure 17 (b). Log Normal

variability or spatial distribution of the scatterers within the scene resulting in the radar backscatter. The distribution of the SAR image intensity can be accounted for by using a multiplicative model which takes into account both radar fading and the texture present in the data. This variability can be modeled after Ulaby, et al. (1986) as

$$P_{ij} = P_i \, T_i(j) \, F_N(j) \tag{15}$$

where

P_{ij} is the image intensity of the jth pixel in the ith field,

P_i is the mean image intensity of the ith field,

$T_i(j)$ is the texture random variable accounting for the natural variability in the ith field, and

$F_N(j)$ is the speckle variable accounting for signal fading (this fading is characterized using a Γ^2 distribution with 2N degrees of freedom).

The texture random variable, Ti(j), in Eq. (15) is dependent on the scattering characteristics of the surface resulting in the radar backscatter, and thus should be considered along with the measured power intensity, P_{ij}, when developing radar scattering models.

Figure 18 presents a scatter plot of the Gamma distribution c-parameter versus the number of independent samples, N, for the 3 year loblolly pine field (test site G3) for each radar frequency. Also presented in Figure 18 are the least-squares regression lines [12] which best fit the data. Clearly, a strong linear relationship exists between the c-parameter and N.

The variability within an image due to the texture (s_t) of the target resulting in the radar backscatter can be expressed after Ulaby, et al. (1986) as

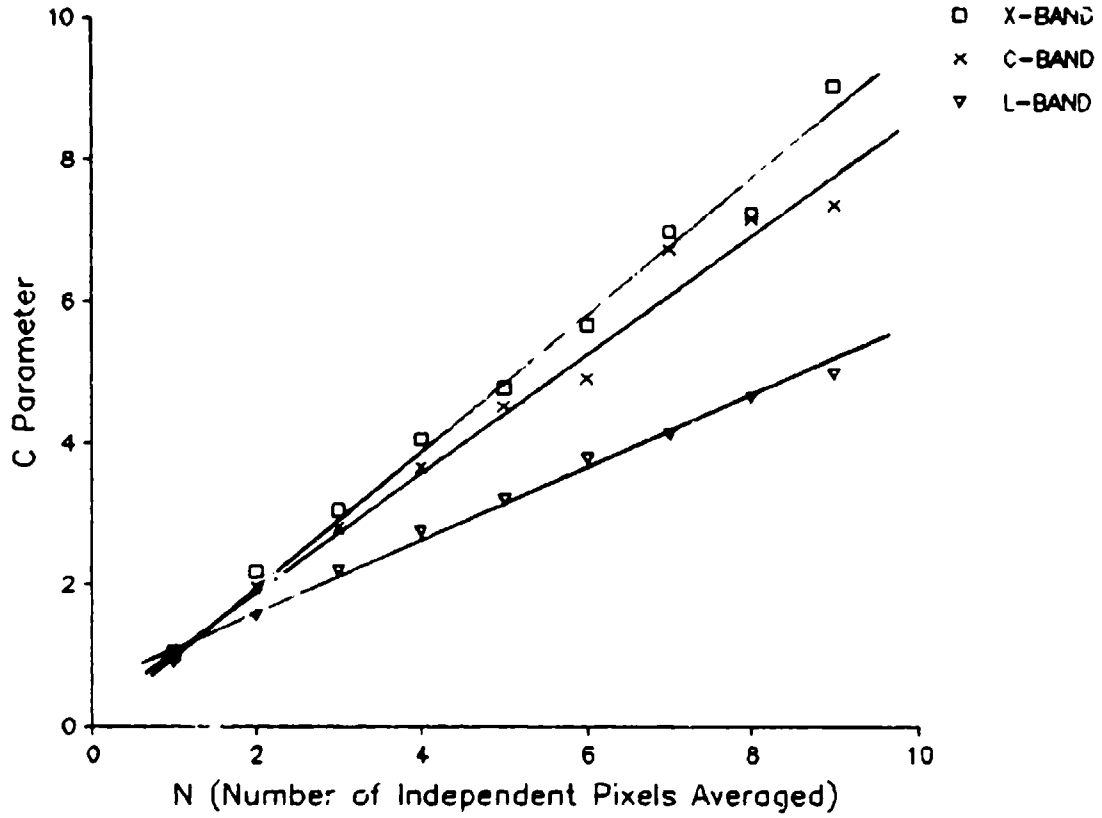

Figure 18. Scatter Plot of Gamma Distribution c-Parameter versus Number of Independent Samples for 3 Year Pine Field

$$s_t^2 = [(s/\bar{X})^2 - 1/N]/[1 + (1/N)]. \quad (16)$$

Combining Eqs. (16) and (5) results in

$$s_t^2 = [(1/c) - (1/N)]/[1 + (1/N)]. \quad (17)$$

Note that in order for Eq. (17) to be valid, c always has to be less than or equal to N. Since our analyses indicate that c is a linear function of N, i.e.,

$$c = AN \quad (18)$$

where A is the slope of the regression line determined by least squares techniques, Eq. (17) can be expressed as

$$s_t^2 = [1 - A]/[AN + A]. \quad (19)$$

From Eq. (19), several observations can be made. First, if the slope of the regression line, A, is 1.0, then s_t^2 is 0. This is consistent with our earlier observation that if c = N, then the Gamma distribution describes a pure speckle background with no scene variability. Second, for any N, as A decreases, s_t^2 increases. And finally, for any c, as N increases, s_t^2 decreases (i.e., as the number of pixels averaged increases, the texture within the scene decreases). The A-parameter for all the test sites examined during this analysis are summarized in Table 8.

TABLE 8
SUMMARY OF A-PARAMETERS FOR STUDY TEST SITES

TEST SITE	DESCRIPTION	X-BAND	C-BAND	L-BAND
G1	Grass Field	1.00	0.80	0.61
G2	3 Year Old Pine	0.97	0.83	0.51
G3	30 Year Old Pine	0.70	0.77	0.76
G4	50 Year Old Pine	0.79	0.72	0.79
G5	Mixed Oaks	0.82	0.67	0.72
G6	Sweetgum/Yellow Poplar	0.92	0.67	0.72
S1	Ocean Surface, 5 kt wind	0.83		0.69
S2	Ocean Surface, 15 kt wind	0.77		0.87
S3	Grass Field	0.83		0.61
S4	Potato Field	0.89		0.62
S5	Unharvested Corn Field	0.59		0.47
S6	Harvested Corn Field	0.55		0.92
S7	Mixed Deciduous Forest	0.59		0.64
M1	First Year Ice	0.70		0.86
M2	Second Year Ic	0.84		0.73

4
COMPARISON OF SCATTERING COEFFICIENTS TO SURFACE ROUGHNESS PARAMETERS

Thus far in this report, we have concentrated on presenting means to extract L-band clutter statistics from SAR imagery. These techniques have included extraction of σ^0 values from SAR data as well as mathematically modelling the distributions of the σ^0 values. Another goal of this program was to collect information on the surface roughness characteristics of the test sites being examined, and to correlate the roughness measurements to the σ^0 values. These comparisons will be presented in this chapter.

In Section 4.1, we present scattering models which utilize surface roughness parameters to estimate radar scattering from different types of fields. In this analysis, we utilize the roughness measurements collected during this program (summarized in Larson, et al. 1986). In Section 4.2, we present a statistical comparison between the σ^0 from the Duke Forest Test Sites and the forest parameters for the 22 test sites. Finally, in Section 4.3, we discuss the implications of the texture measures derived from the Gamma distribution with respect to the scattering properties of the scene.

4.1 MODELLING OF RADAR CROSS SECTION (σ^0)

Three scattering models were evaluated for the describing σ^0 values observed from several of the Long Island Test Sites. These models were exercised using the surface roughness measurements collected coincidently with the SAR overflights. Four fields were used in this analysis: Site M (smooth, bare field); Site H (corn stubble); Site K (grass field); and Site RF3 (grass field).

4.1.1 SCATTERING MODELS

The scattering models utilized in the present study were: (1) the Barrick and Peake (1967) model for slightly rough surfaces; (2) the

Barrick (1968) model for slightly rough surfaces based and Gaussian surface height statistics; and (3) the Rayleigh scattering model defined by Rice (1951).

The two scale models combine the backscatter from a slightly rough surface with the scattering predicted by specular theory. The backscatter coefficient as derived by Barrick and Peake (BP) for a slightly rough surface is given by

$$\sigma_{xx} = 4\, k_o^4 \cos^4\theta_1 |a_{xx}|^2\, W(-2k_o \sin\theta_1) \qquad (20)$$

where

K_0 = $\frac{2\pi}{\lambda}$
o_1 = incident angle
$W(\theta_1)$ = surface height spectrum
$a(\theta_1)$ = scattering coefficient
xx = transmitter/receiver polarizations

Both the surface height spectrum and scattering coefficient have been derived from ground measurements and used to calculate a value for σ. The second part of the two scale model uses the scattering coefficient predicted from specular theory as developed by Barrick (1968). The scattering coefficient, derived by Barrick and based on Gaussian surface height statistics, is given by:

$$\sigma_{vv} = \sigma_{hh} = [(\sec^4\theta_1)/S^2] \exp[(\tan^2\theta_1)/S^2] |R(o)|^2 \qquad (21)$$

where S^2 = mean square of surface slope
R(o) = normal, O = 0, reflection coefficient

Values for the parameters in the BP slightly rough model are derived from surface roughness measurements and dielectric constant measurements.

The Rayleigh scattering model as extended by Rice (Cosgriff, 1960) is of value for the slightly rough surfaces considered in this investigation. The scattering coefficient σ_o is given in Equation 22 for the Rice model.

$$\sigma^o = 8 \cos^4\theta_1 \, \bar{h}^2 k_o^4 \int_{-\infty}^{\infty} p(h) \, J_o(2k_o h \sin\theta_1) \, r \, dr \qquad (22)$$

where h^2 = mean square surface roughness, and
$\rho(r)$ = surface height autocorrelation function

The Barrick and Peake and Rayleigh (Rice) scattering models were exercised using the surface roughness and moisture parameters listed in Table 9 and summarized in Figures 19 and 20. Both of these models were exercised for VV and HH-polarizations. The results of the models are presented in Figures 21 and 22. Also presented in the plots are the SAR-observed σ^o values for the HH-polarized imagery. Finally, Figure 23 presents a comparison of the HH-polarized data.

Overall, we can see that the Rayleigh (Rice) model predicts lower σ^o values than the Peake and Barrick model. Both models predict the observed decrease in L-band σ^o as a function of incidence angle. The Peake and Barrick model results match the observed results quite well, with the model overpredicting the SAR-observed values somewhat for test sites M and RF3. Contributions to the scattered field from the slightly rough component of the BP model dominated the true scale model results. The only test site where the Rayleigh (Rice) model comes close to matching the SAR-observed σ^o values is for test site H. In all other cases, the model significantly underpredicted the observed results.

TABLE 9

SUMMARY OF SURFACE ROUGHNESS AND MOISTURE PARAMETERS
USED AS INPUTS INTO THE SURFACE SCATTERING MODELS

Test Site Description	Values of Measured Surface Parameters				Derived Surface Parameters		
Site Photo-Figures*	Surface Height Figure #	rms Height	Dielectric Constant Top 5 cm	Moisture Content	Height Spectra Figure #	Correlation Lenght/Function Inches/Figure #	Slope rms
MEW	19a	0.137	3.98	11.6	20a	3.79/20a	.243
MNS	19a	0.186	3.98	11.6	20b	5.66/20a	.076
RFS	19b	0.446	3.69	13.21	20b	7.64/20b	.044
H	19c	0.486	3.66	10.7	20c	12/20c	.017
K	19d	0.246	4.3	16	20d	4.28/20d	.065

*Photos included in Interim Report RADC-TR-85-266.

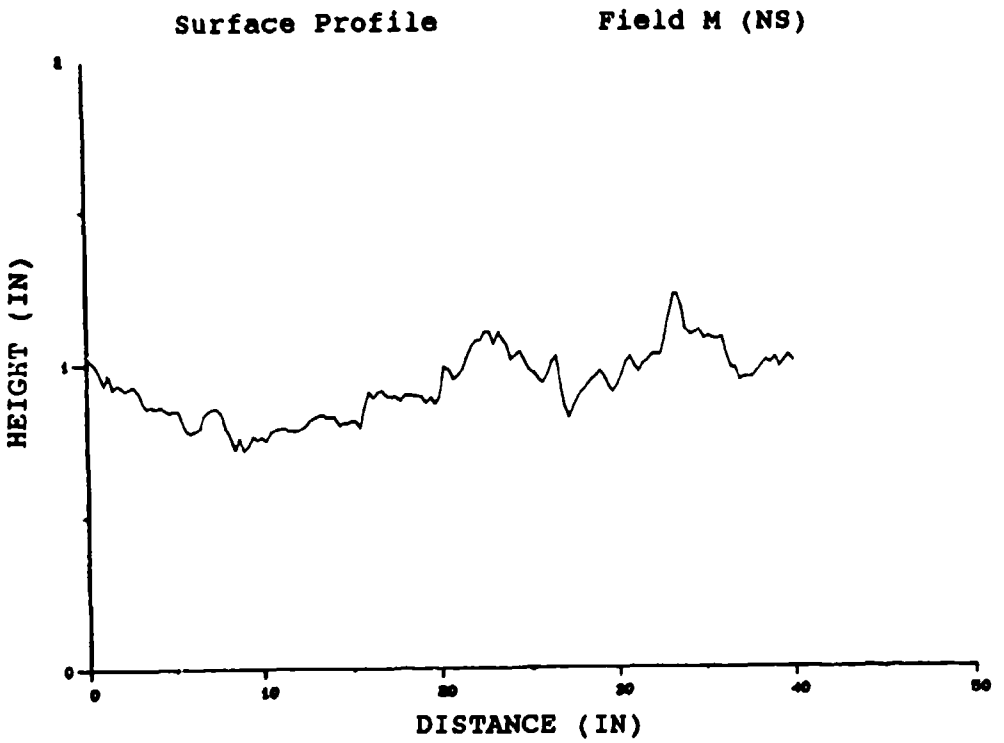

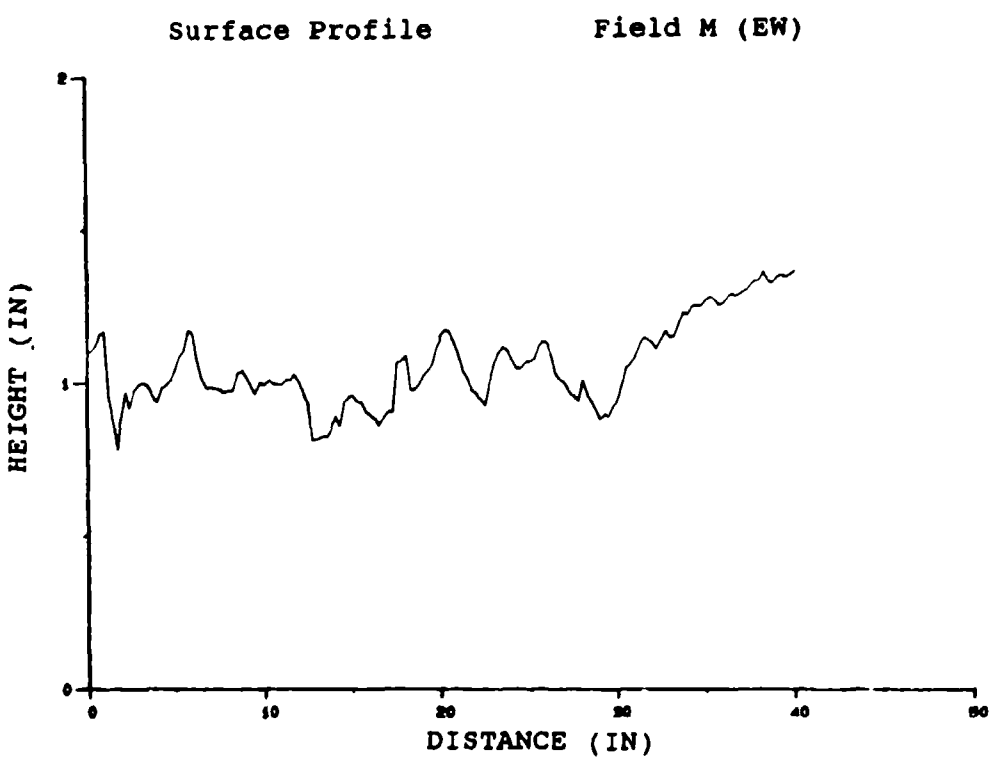

Figure 19. Surface Height Distribution Plots for Long Island Test Sites [Figures (a) through (d)]
(a) Site M - Smooth, Bare Field

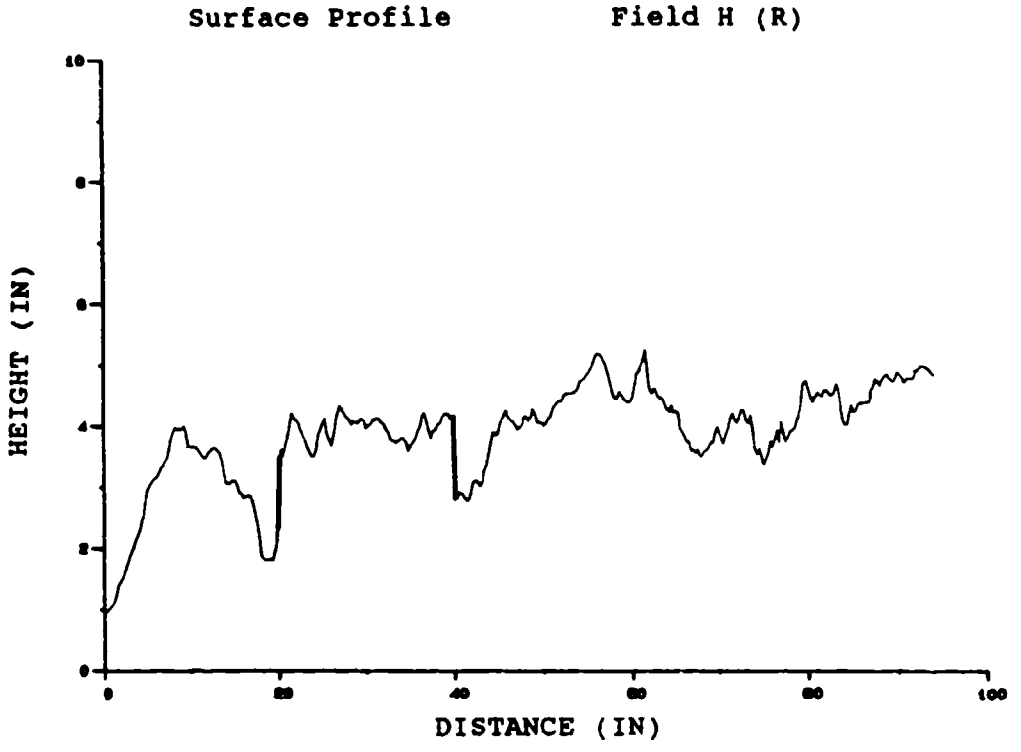

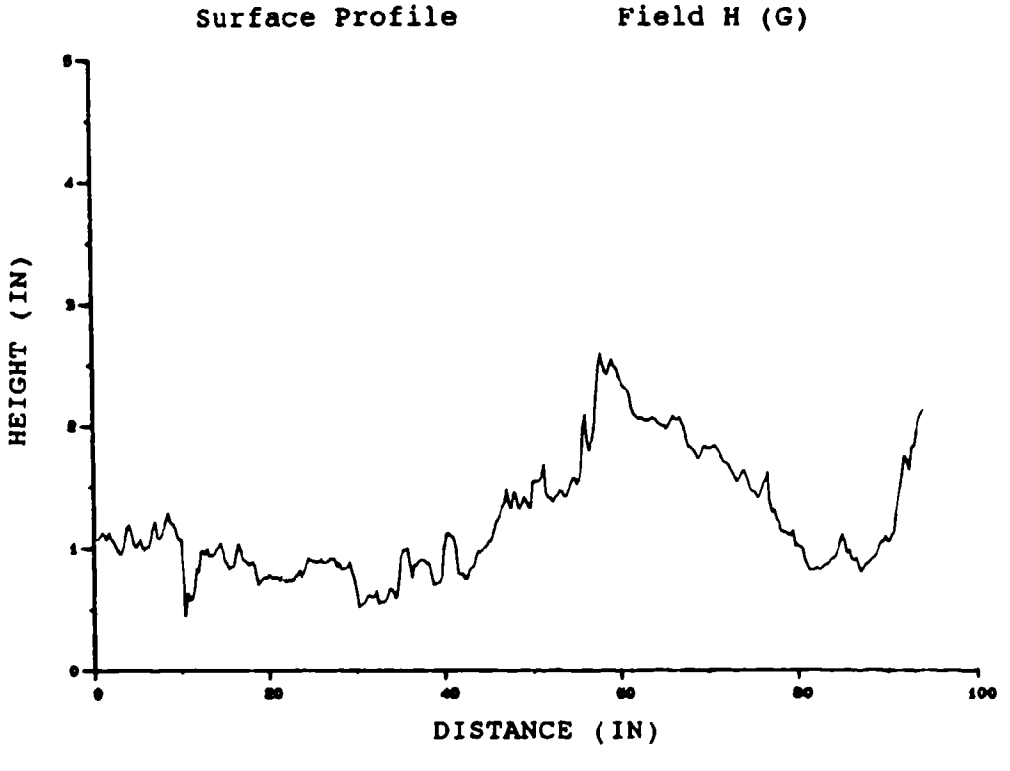

Figure 19 (b). Site H - Corn Stubble

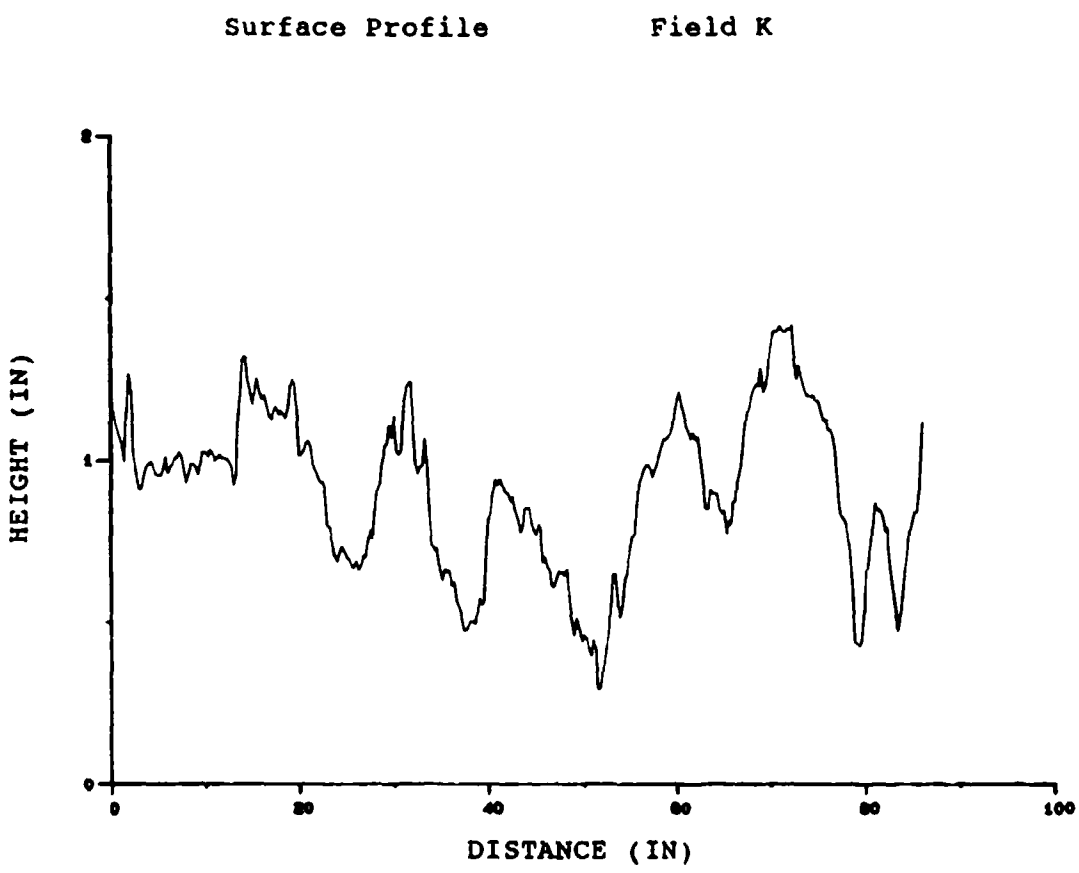

Figure 19 (c). Site K - Grass Field

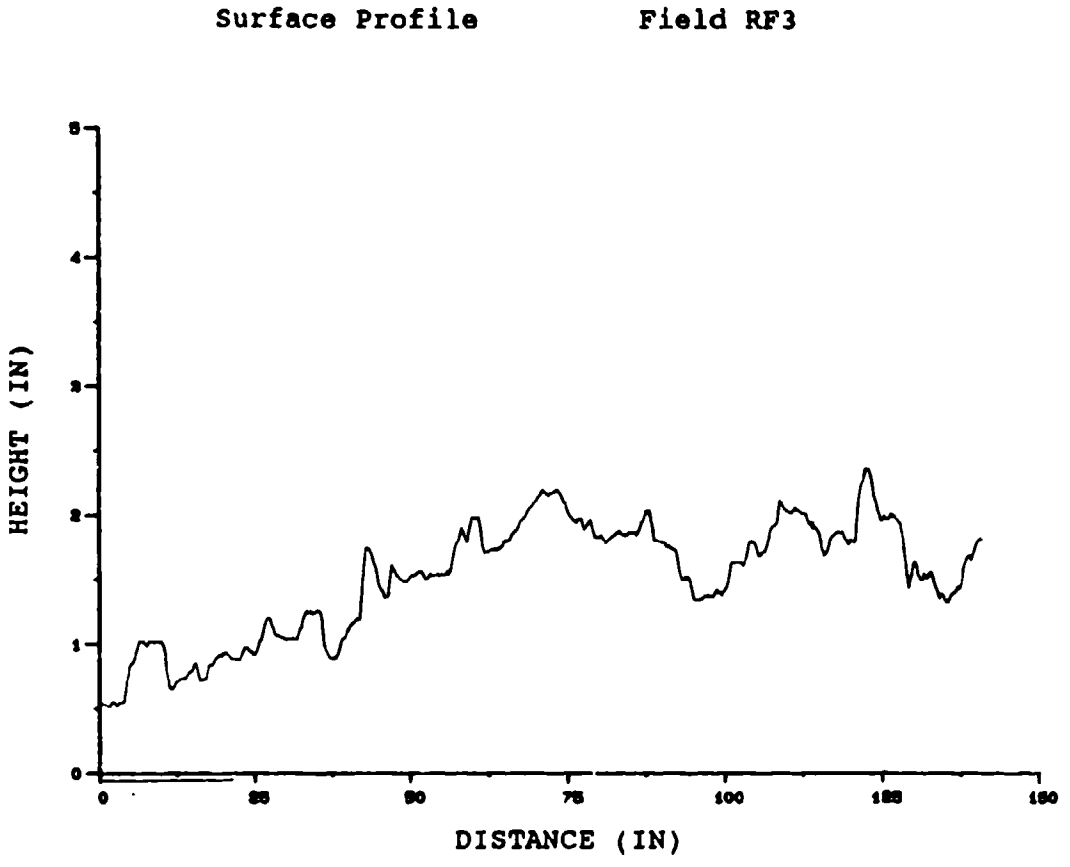

Figure 19 (d). Site RF3 - Grass Field

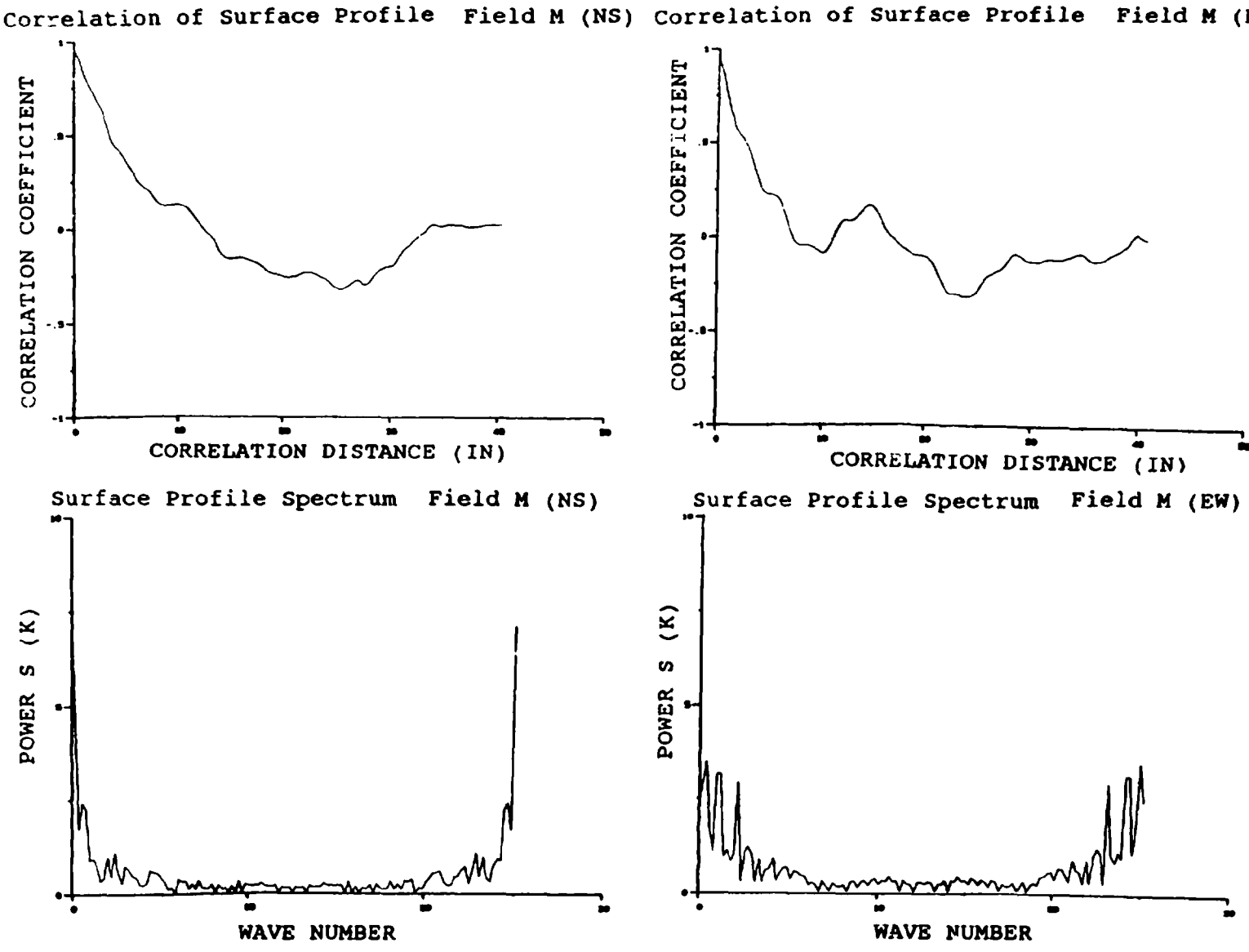

Figure 20. Correlation Length and Spectra Plots for Long Island Test Sites [Figures (a) through (d)]

(a) Site M - Smooth, Bare Field

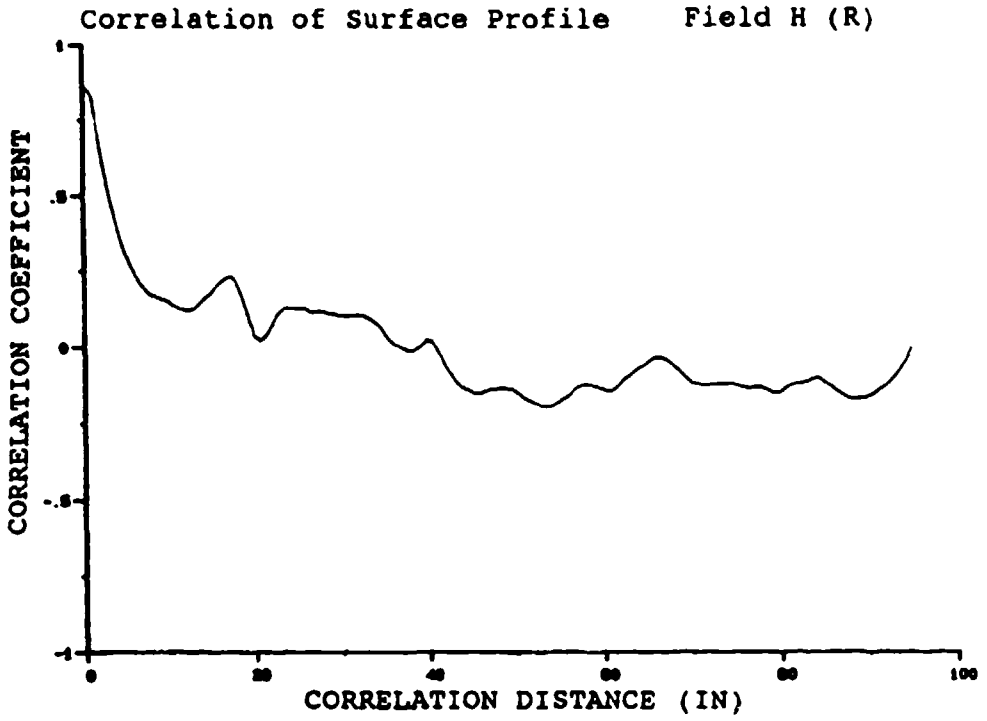

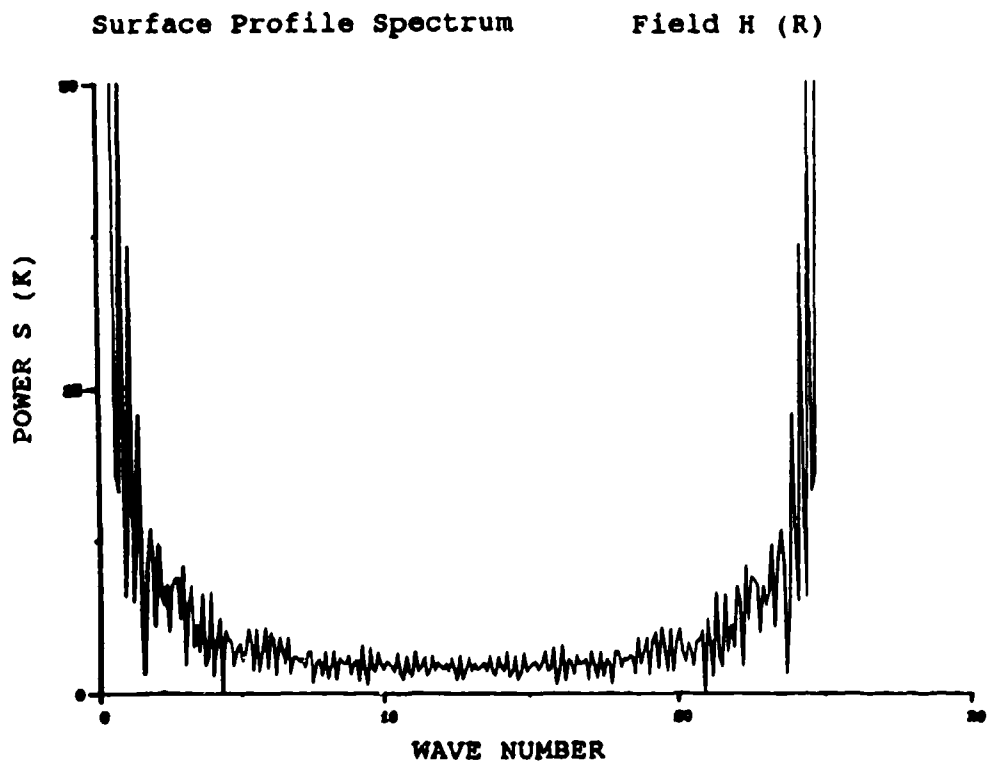

Figure 20 (b). Site H - Corn Stubble

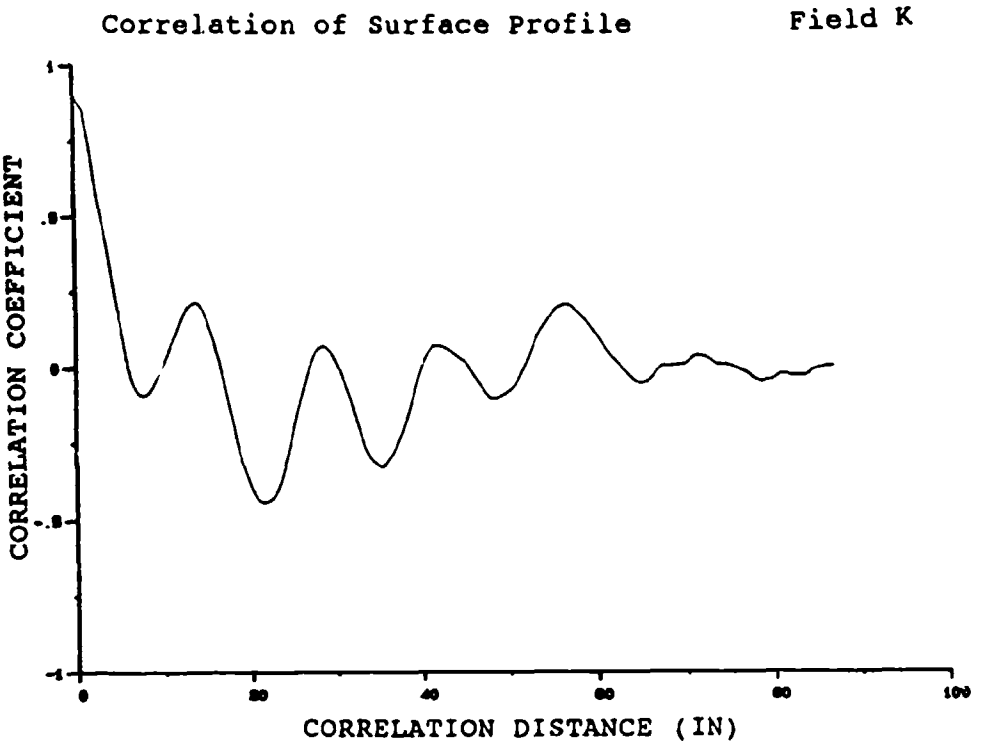

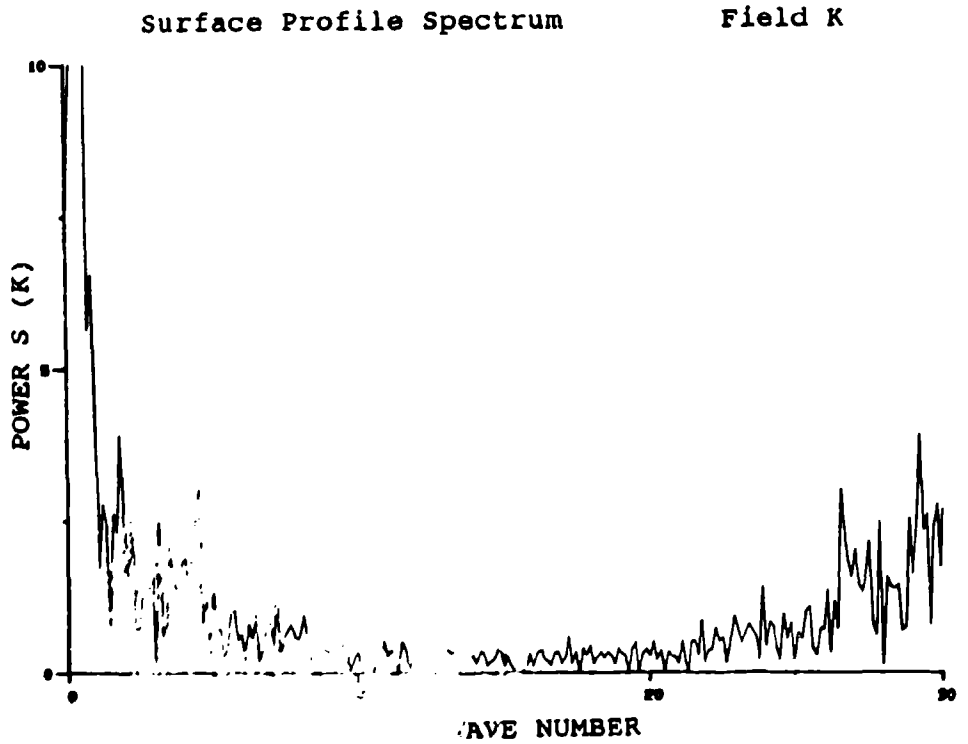

Figure 2(c). Site K - Grass Field

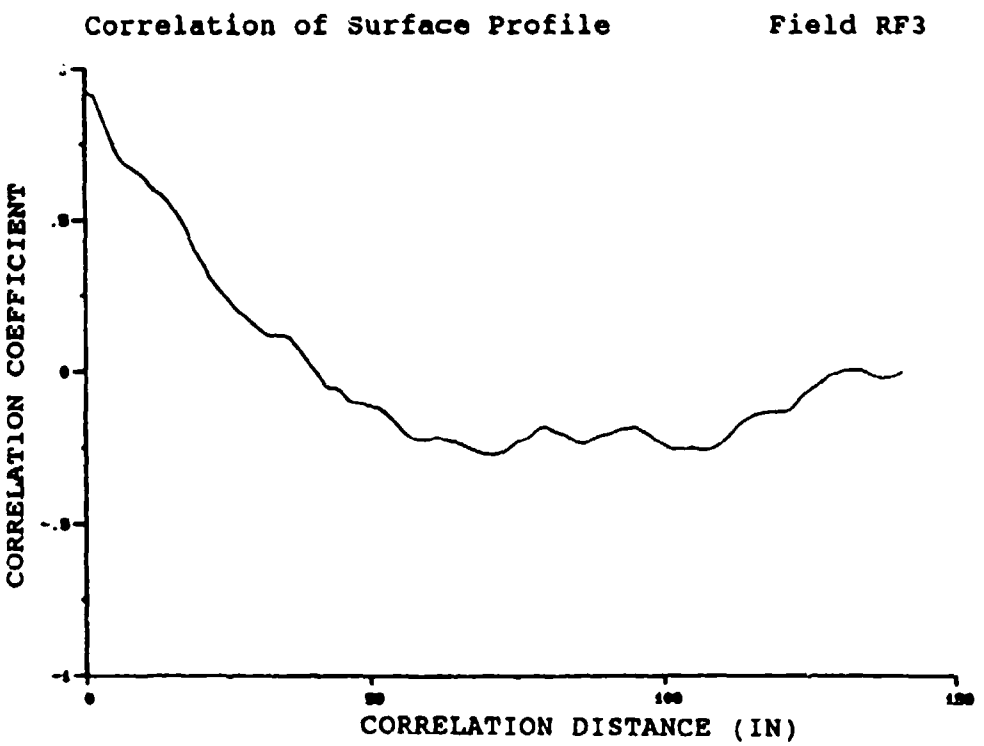

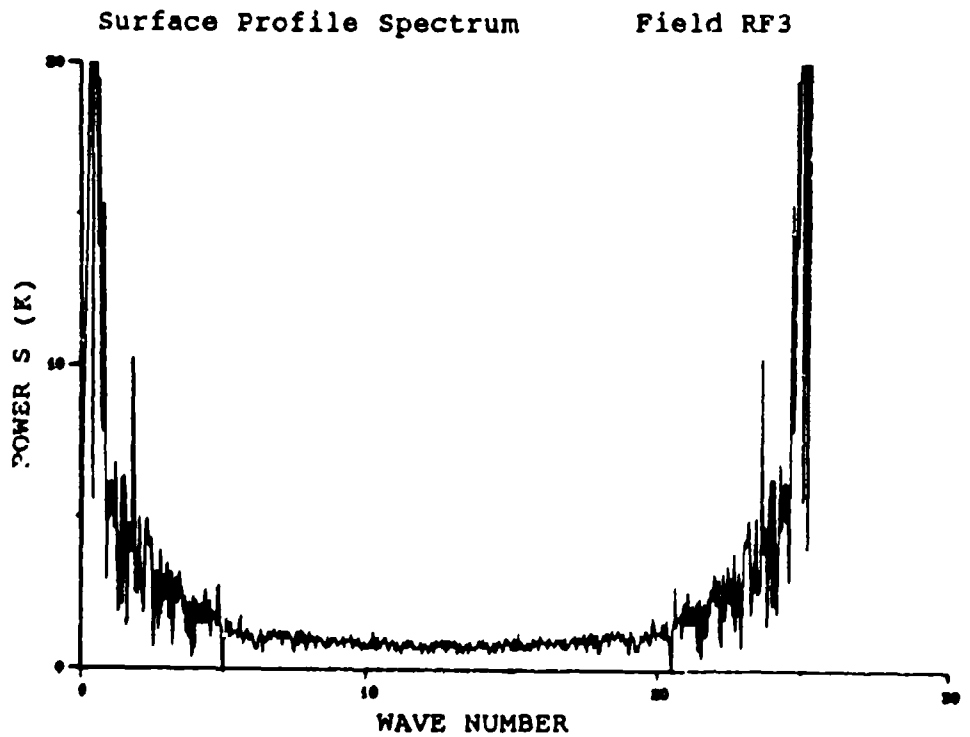

Figure 20 (d). Site RF3 - Grass Field

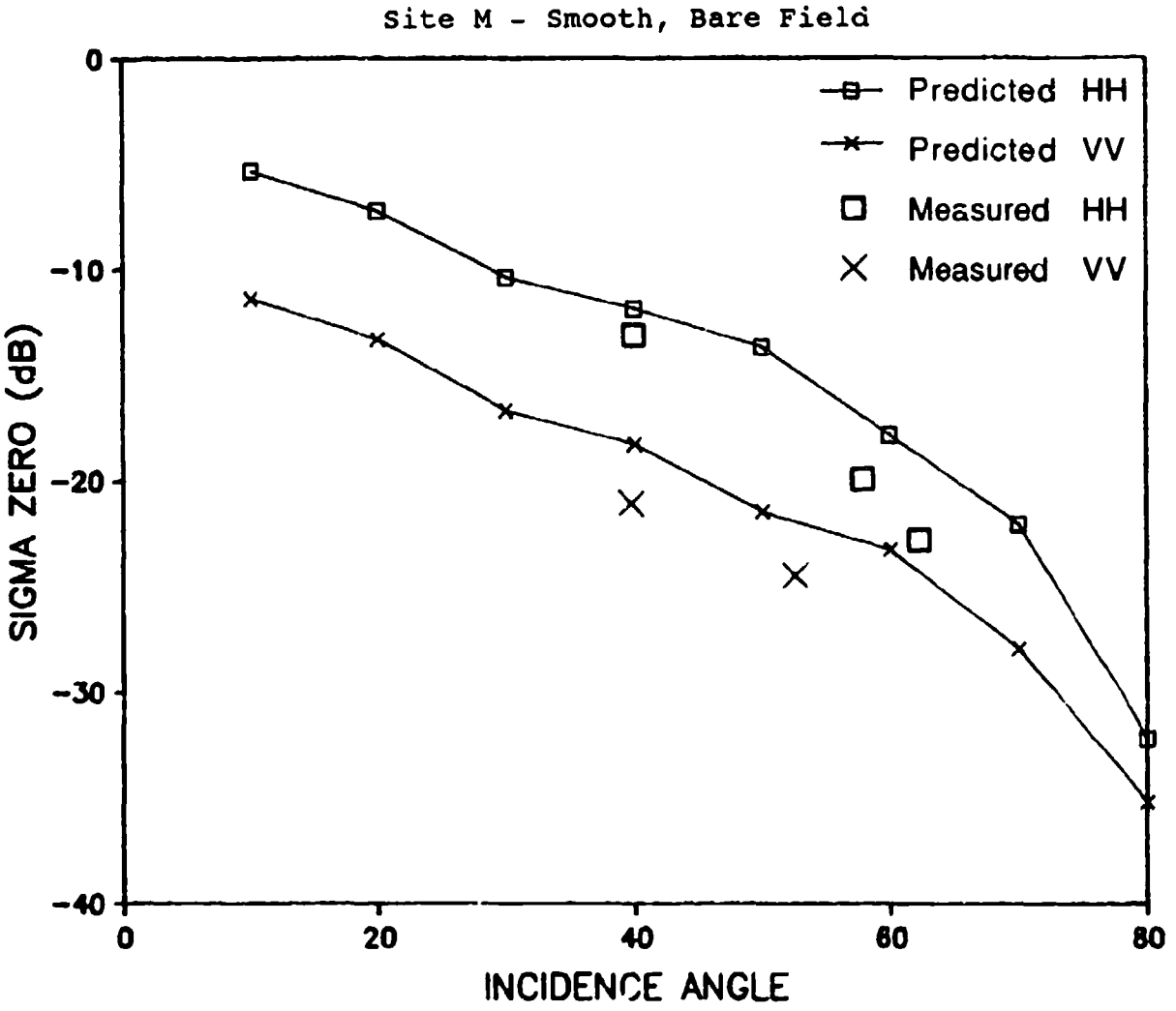

Figure 21. Results of Peake and Barrick Model Predicted versus SAR-Derived Values of σ^{o} [Figures (a) through (d)]
(a) Site M - Smooth, Bare Field

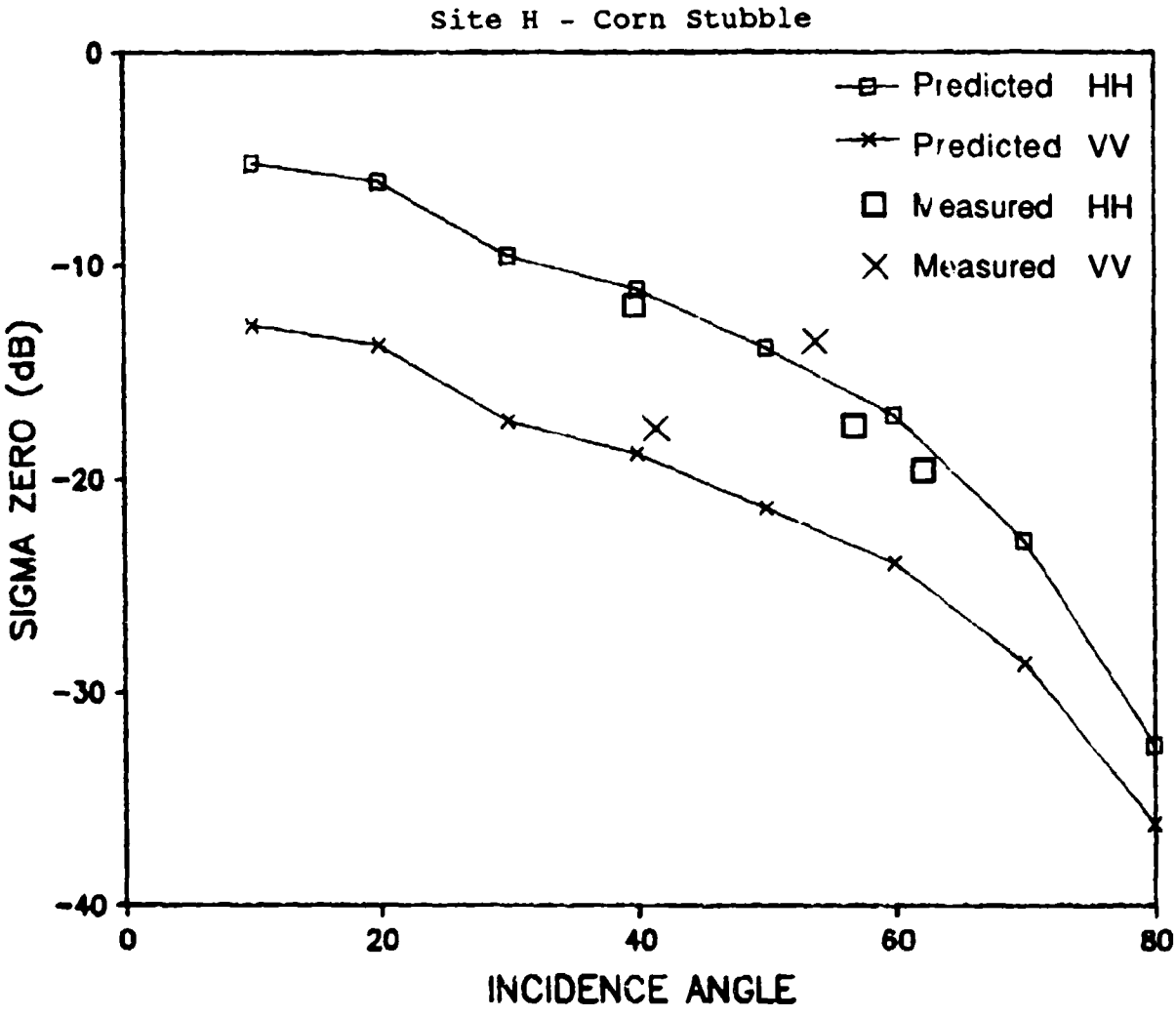

Figure 21 (b). Site H - Corn Stubble

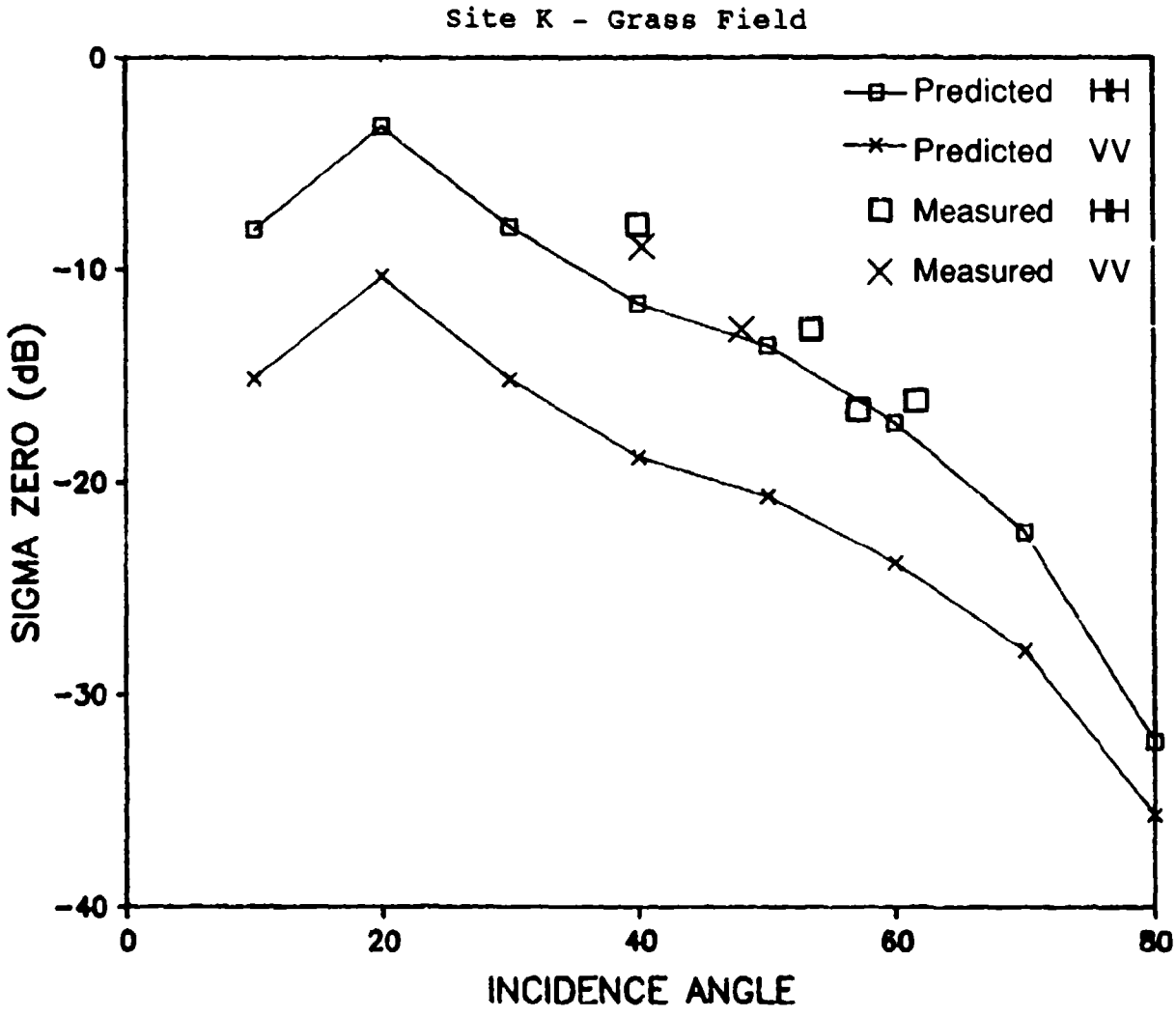

Figure 21 (c). Site K - Grass Field

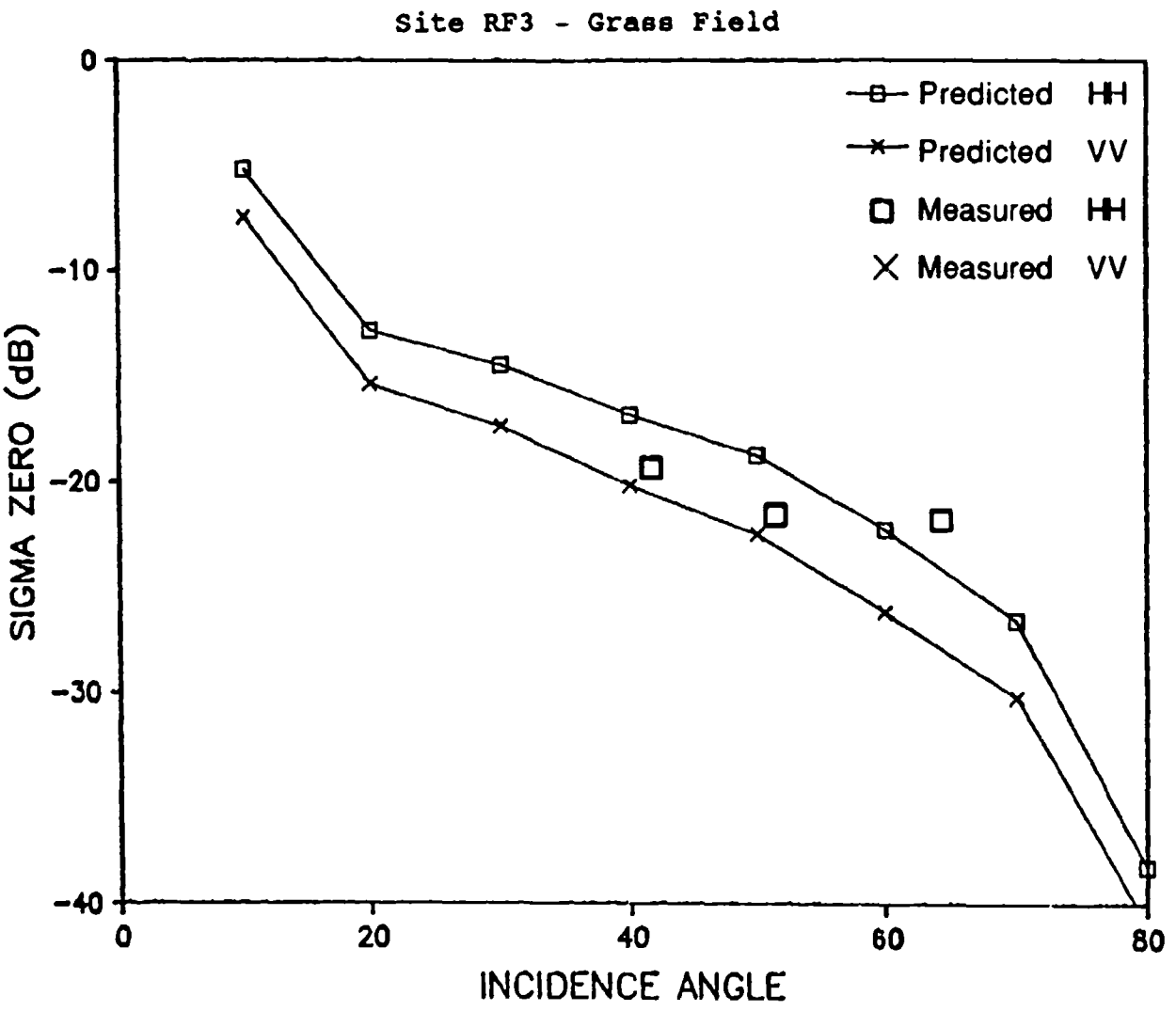

Figure 21 (d). Site RF3 - Grass Field

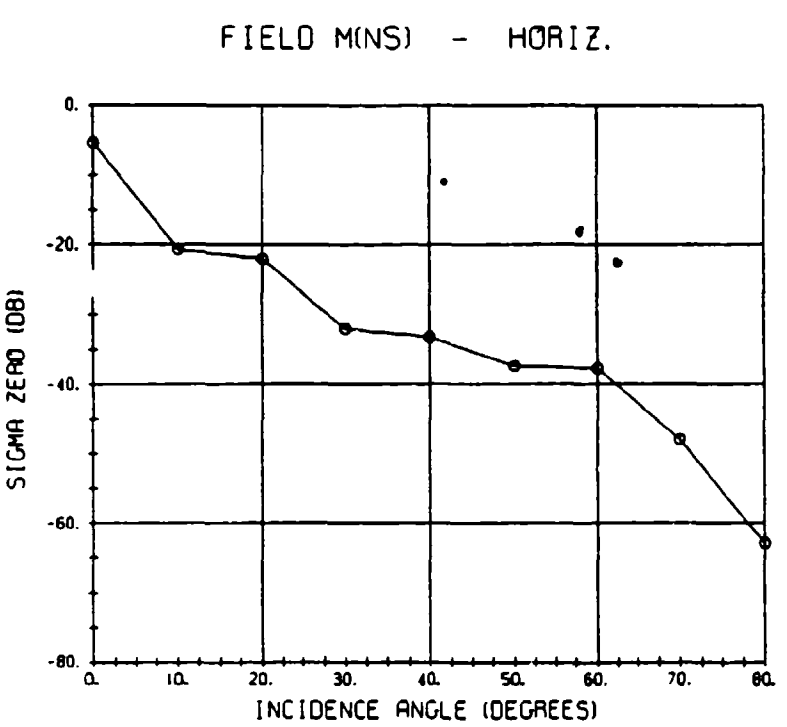

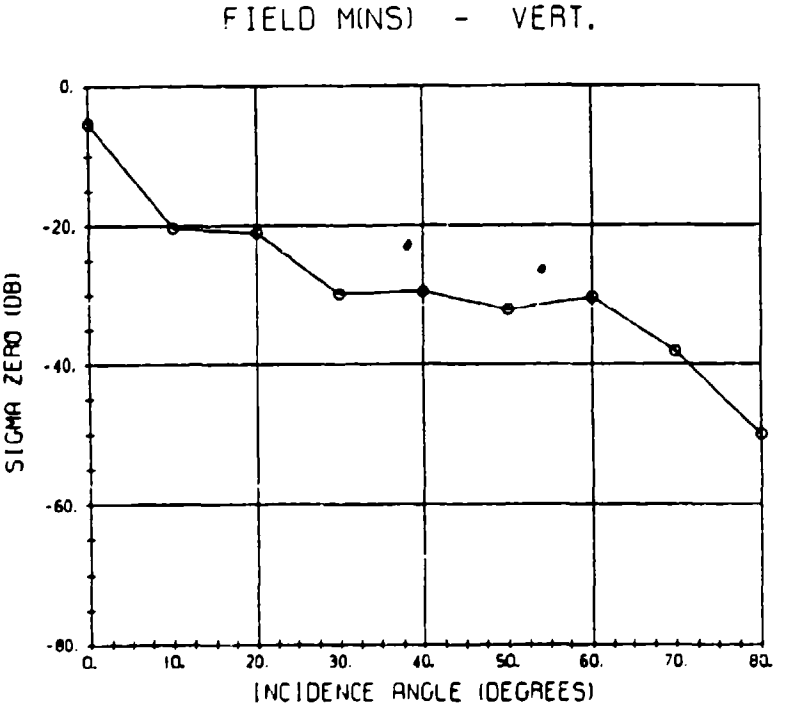

Figure 22. Results of Rayliegh (Rice) Model Predicted versus SAR-Derived Values of σ^{o} [Figures (a) through (d)]

(a) Site M - Smooth, Bare Field

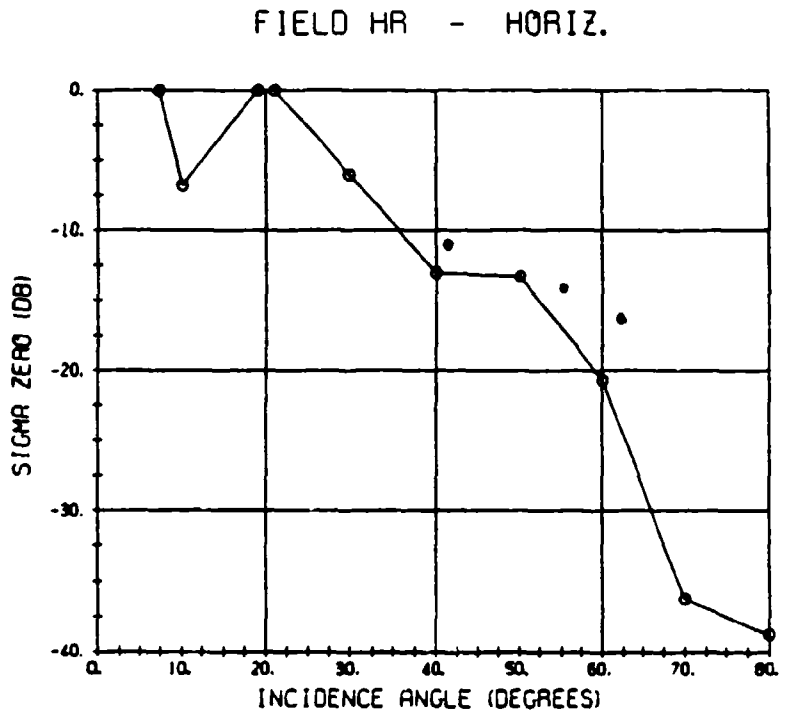

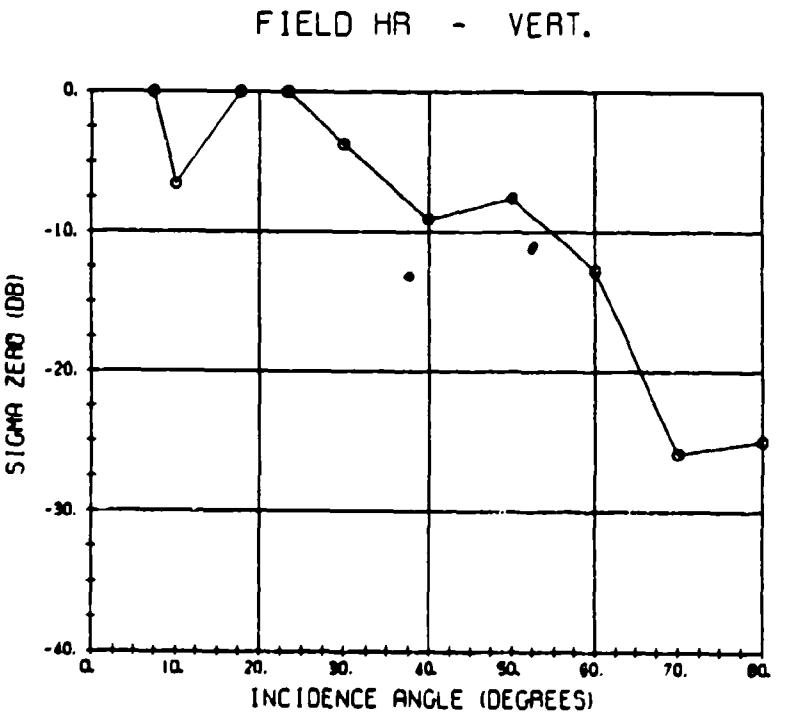

Figure 22 (b). Site H - Corn Stubble

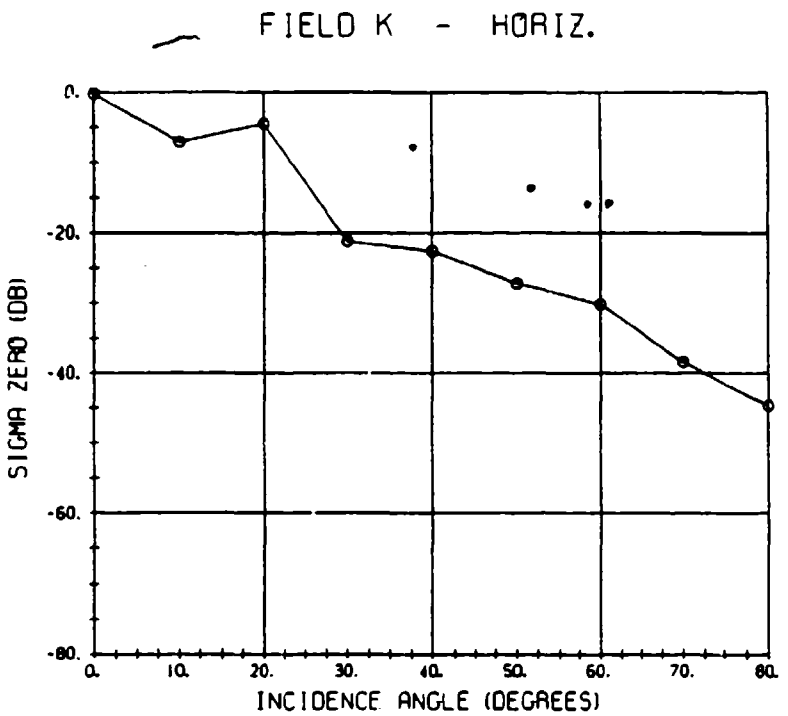

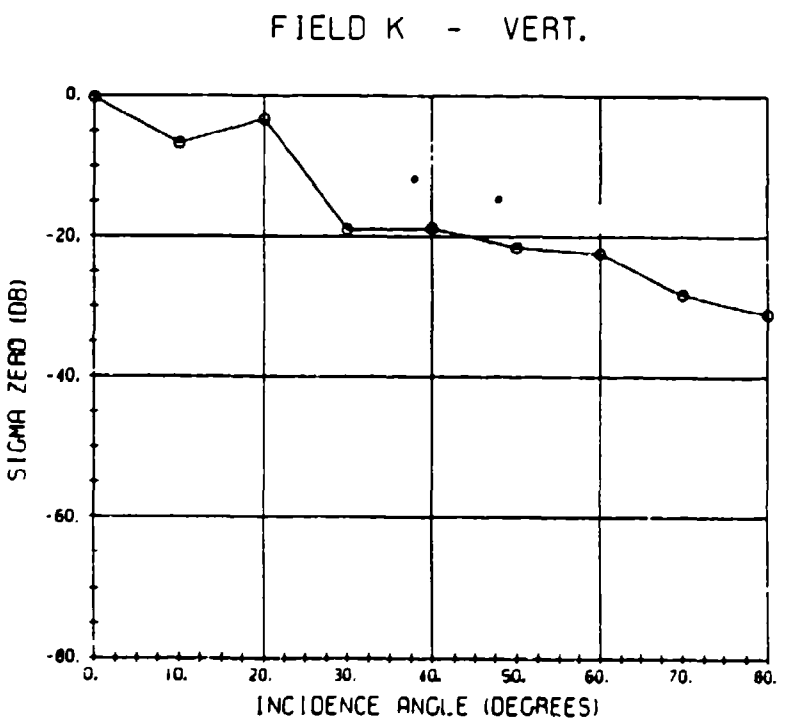

Figure 22 (c). Site K - Grass Field

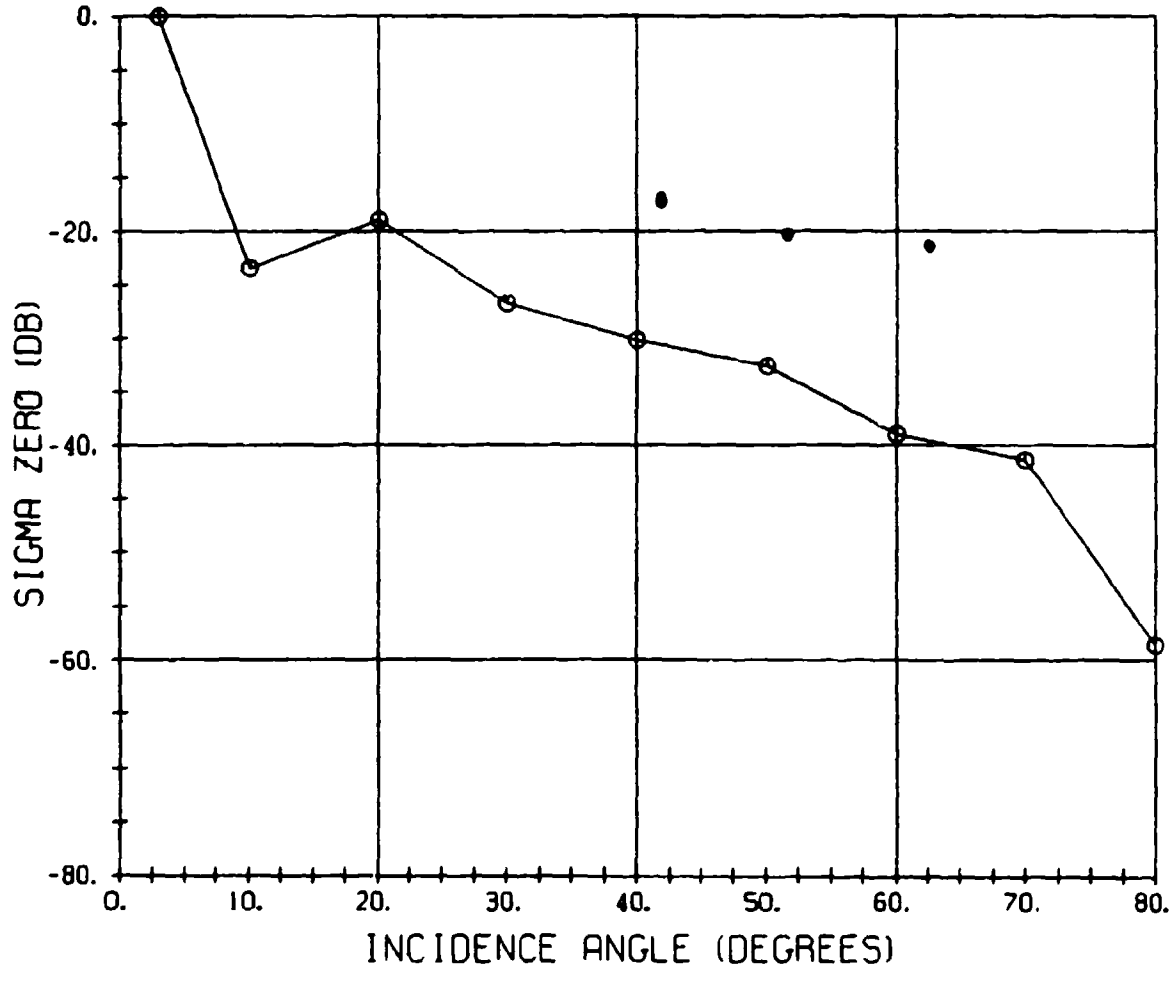

Figure 22 (d). Site RF3 - Grass Field

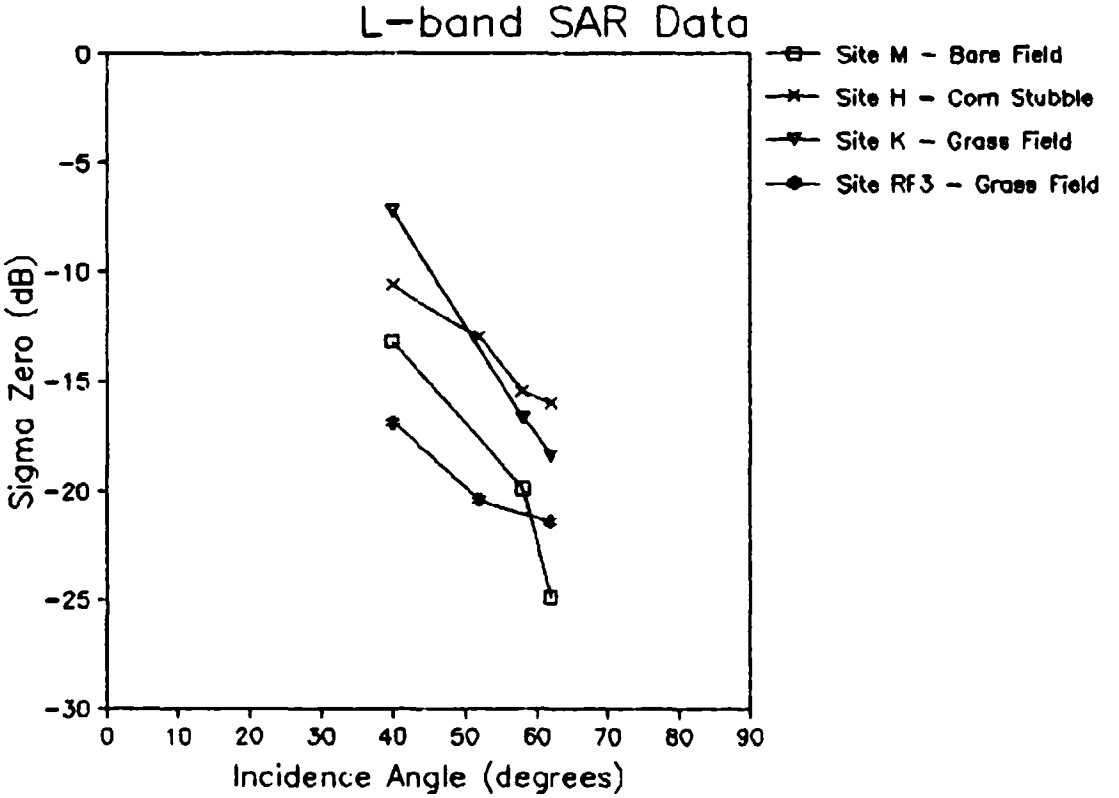

Figure 23. Comparison of Modeled versus SAR-Observed Values of σ^{o}. [Figures (a) through (c)]
(a) SAR-Derived Values

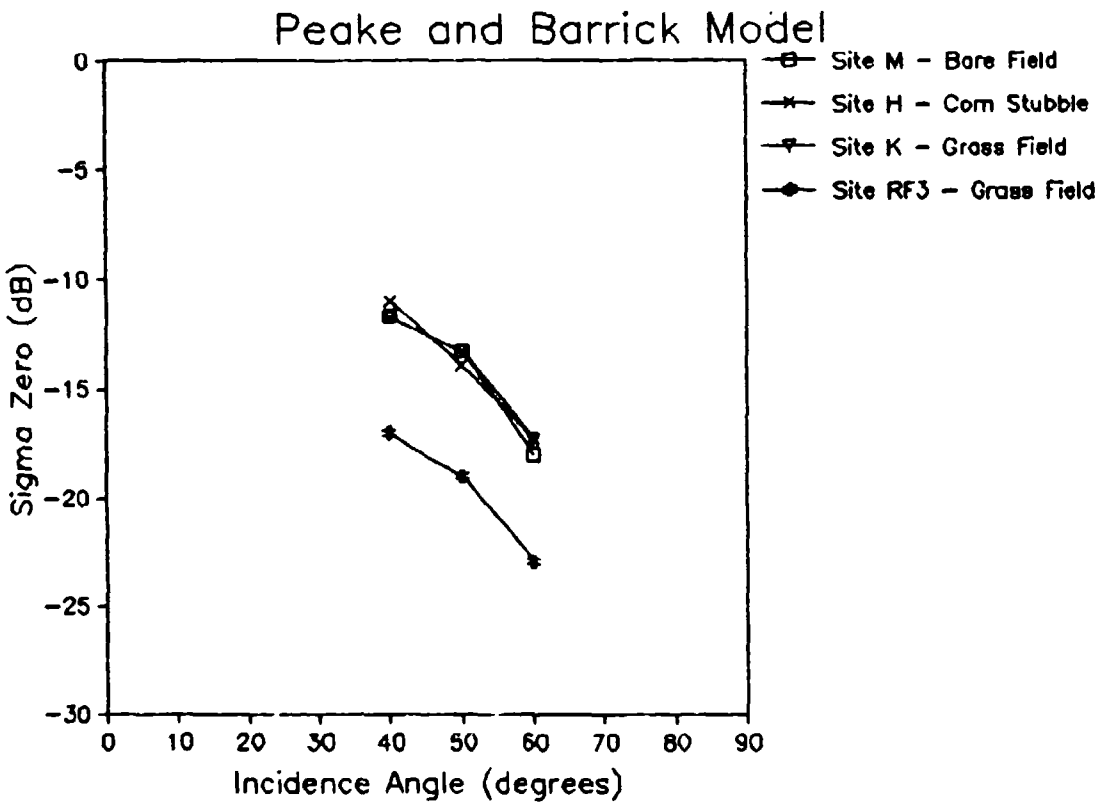

Figure 23 (b). Peake and Barrick Model

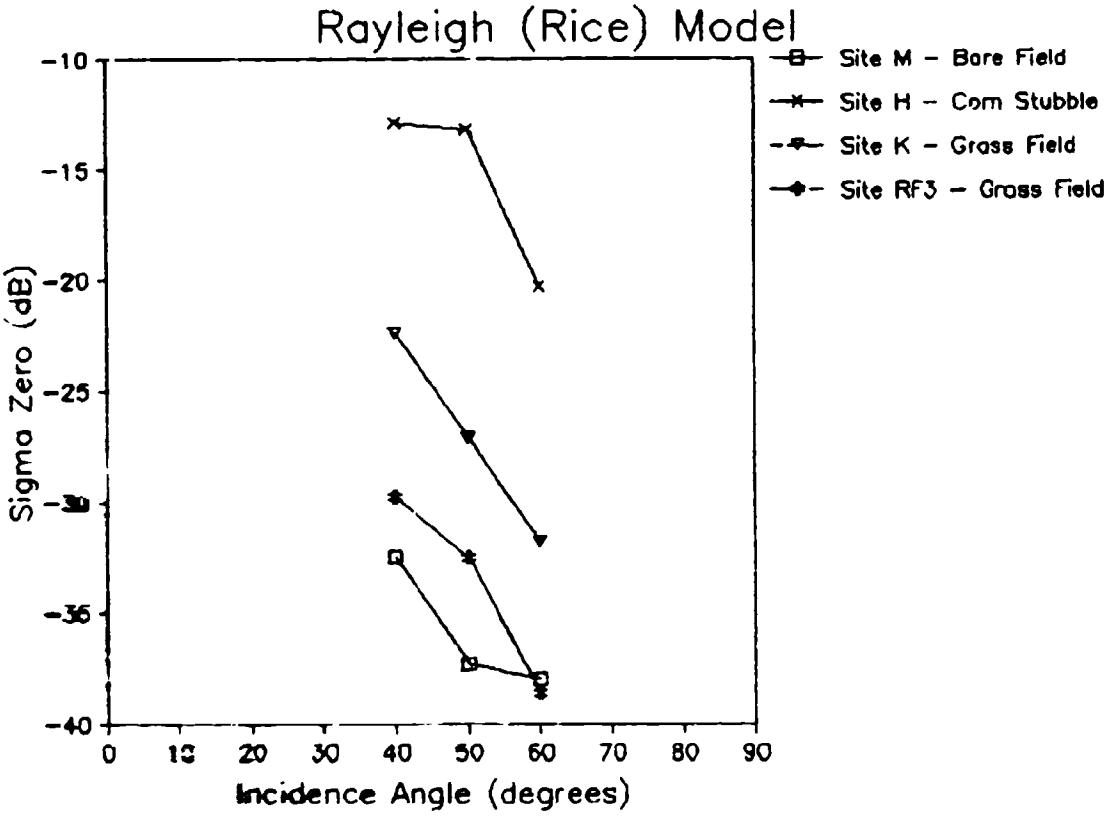

Figure 23 (c . Rayleigh (R ce) Model

4.2 STATISTICAL COMPARISONS

The next step in the analysis was to correlate the radar scattering coefficients listed in Table 5 with the forest canopy parameters presented in Table 3. The test sites were divided into two groups (hardwood stands and conifer stands) for these correlations. Simple linear correlations (Draper and Smith, 1966). indicated a significant relationship (at the 0.90 level of significance) between the L-band scattering coefficients and coniferous tree height (= - 0.65) and hardwood stems per acre (R = 0.69). Multiple linear regression analysis (Draper and Smith, 1966) of the data showed a significant (at the 0.90 level) correlation between the C-band scattering coefficients and deciduous DBH, basal area and tree height (R =0 .92) and the L-band scattering coefficients and coniferous DBH and tree height (R = .90).

These statistical correlations should be beneficial in more deterministic modeling efforts. A first order model to describe the forest radar cross section, σ_f, can be expressed after Ulaby, et al. (1982) as

$$\sigma_f = T_c^2[\sigma_b + \sigma_t + T_u^2(\sigma_s + \sigma_{st})] \qquad (23)$$

where T_c is the transmissivity of the overstory canopy layer,
T_u is the transmissivity of the understory canopy layer,
σ_b is the cross section of the branches in the overstory,
σ_t is the cross section of the tree trunks in the overstory and understory,
σ_s is the cross section of the soil layer, and
σ_{st} is the soil/trunk interaction scattering coefficient.

The correlations found in this study indicate that at C- and L-band, a significant portion of the radar backscatter is explained by parameters which describe the dimensions and numbers of tree trunks in

the forest stand. These results indicate that modeling efforts at C- and L-band at vertical polarization should initially concentrate on those parts of scattering model described in Eq. (23) which involve the σ_t and σ_{st} terms.

4.3 SCENE TEXTURE AS A FUNCTION OF SCENE COMPOSITION

Examining the scene texture as described by the A-parameter presented in Chapter 3 may lend insight into the processes resulting in the radar backscatter from the different test sites. For this study, six test sites from the Duke Forest test site were selected (see Figure 13): B9 (grass field); B8 (3 year pine); B19 (30 year pine); B10 (50 year pine); B7 (mixed oak) and B5 (sweetgum/yellow poplar).

The nature of the scattering will affect the surface texture in two ways. First, for single-bounce, surface scattering, the spatial distribution of the surface scatterers should be detected directly in the observed texture pattern. For volume scattering, the spatial patterns of the scatters will not be as clear because of the multiple-bounces within a volume-scattering medium will act to reduce the variation of the pixel intensities within the scene. Forests will act as a complex scene with respect to texture because, depending on wavelength, parts of the canopy will act as volume scatterers while other parts will result in direct radar backscatter.

Figure 24 presents plots of the regression lines of the c- parameter as a function of N for the six test sites. These plots compare the X-, C- and L-band data. Figure 24, from the grass field (see Figure 13g), contains the results which are most readily interpreted. At X-band, the scattering is most likely occurring from volume scattering from the grass itself. Since grass is very homogeneously distributed throughout the scene in this case, with no bare ground being visible, the scattering is almost exponential in nature

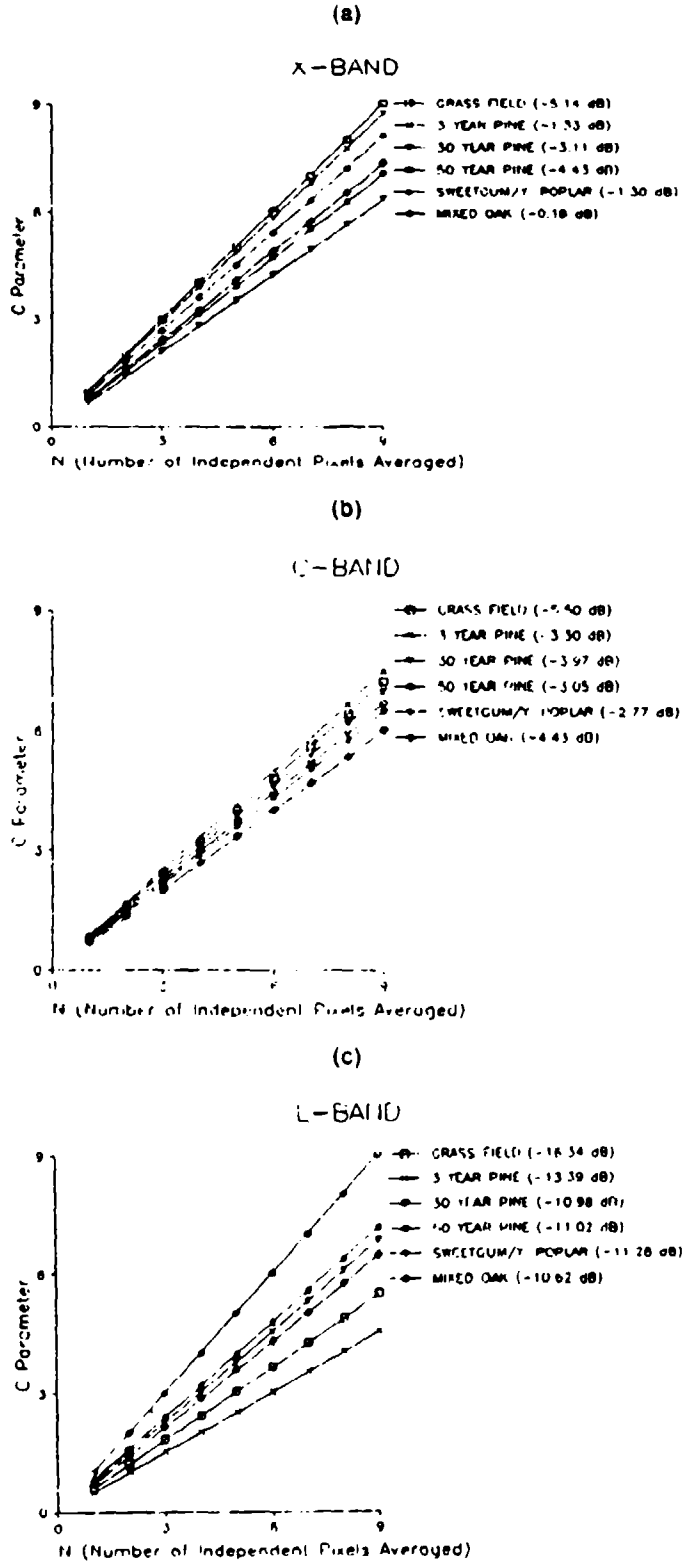

Figure 24. Regression Lines of the C-Parameter as a Function of N (the number of independent pixels averaged)

(i.e., A = 1.00). The opposite extreme from the volume scattering in the X-band case is the L-band scattering, which is more than likely almost entirely from the soil underneath the grass. This surface scattering results in rougher texture in the L-band image. At C-band, we would expect a combination of volume and surface scattering, resulting in a texture somewhere between those observed at X- and L-band. This is indeed the case.

The next most complex scattering case is represented by the 3 year pine stand (see Figure 13a). At L-band, the branches of the small pine trees are probably not large enough to influence the scattering of the vertically-polarized waves, but the trunks of these trees are probably large enough to result in additional scattering from the scene. This additional scattering is indicated by the higher L-band σ^0 value for the 3 year pine stand relative to the grass field, and also results in more texture in the scene, as the decrease in the A term in Table 8 and Figure 24 indicates. At X- and C-bands, there is almost no change in image texture compared to the grass fields, indicating that the vertically-polarized electromagnetic energy at these radar frequencies is not being greatly influenced by the presence of the small pine trees in this field.

While simple, first-order scattering models can be used to explain the differences in observed texture for the grass and three year pine test sites, more complex models are needed for the test sites which contain a fully-developed forest canopy. The only mature forest test site where any significant variation in scene texture exists is for the sweetgum/yellow poplar stand. Two questions arise when examining the textures for the mature forest stands. First, why are there no variations in texture as a function of radar frequency for the 30 year pine, 50 year pine and mixed oak stands? And second, why does the image texture at X- and L-bands for the sweetgum/yellow poplar stands vary from the other stands? The answers to these two questions depend to a great degree on the sources of the scattering at the different

radar frequencies. Radar scattering models from forest canopies have not been developed to the point where these questions can be addressed. One possible explanation lies in the density of the trees within the four mature forest stands. From Table 5, we can see that the sweetgum/yellow poplar stand had a lower tree density (470 stems/ha) than any of the other three sites (620 to 963 stems/ha). The lower tree density may result in a discontinuous canopy profile for this stand (versus a continuous canopy profile for the others), causing a different spatial pattern in the scene scatterers, which is detected as a texture difference in the SAR imagery.

5
CONCLUSIONS AND RECOMMENDATIONS

A goal of research sponsored by the Rome Air Development Center (RADC) is to develop a terrain scattering model to predict terrain scattering properties at L-band. In order to achieve this goal there has been a need to:

1. Collect a data base of radar cross-section signatures (both the mean and the histogram) for various terrain types,
2. Collect a coincident (with [1] above) set of surface scattering characteristics (i.e., surface roughness and dielectric property measurements) for the various terrain types, and
3. Develop a model (deterministic and statistical) which predicts the radar cross-section signature as a function of the surface scattering characteristics.

Research has been conducted at ERIM for RADC over the past two years to further develop L-band terrain scattering models (Larson, et al., 1986; Kasischke 1987). Under this program, a set of airborne, L-band SAR data collected over several test areas has been analyzed. L-band cross-section signatures of various terrain types have been extracted from the SAR data using ERIM's digital SAR image calibration algorithm (see Larson, et al., 1986). These signatures include both an average radar cross-section value (σ^o) as well as a radar cross-section histogram for each terrain type.

A selected set of terrain property measurements were made for a limited set of test sites during each SAR overflight. From each site the following information or data were obtained: (1) soil samples were obtained, from which dielectric property, soil moisture and soil density measures were obtained; (2) surface photographs were taken to document the general state of the vegetation; (3) the height and density of the vegetation were noted, and measured when ever possible; and (4) surface height profiles were obtained, from which additional

surface roughness properties were derived, including: (a) spectrum of the surface height, (b) slope distribution, (c) radius of curvature, and (d) autocorrelation of the surface heights (see Larson, et al., 1985).

Results obtained and reported under the present research effort include the correlation of the cross-section signatures with surface parameter measures via scattering models. These models are either deterministic or statistical in nature.

The deterministic models are used to correlate the average radar cross-section with the surface scattering properties. The second modeling effort has utilized methods for describing the statistical distribution of the radar cross-section values for each terrain type. The cumulative distribution model is compared to the actual radar derived distribution via non-parametric statistical tests.

With the exception of Forest sites, all of the test fields for which surface measurements were obtained are classified as slightly rough. The appropriate surface parameter descriptor, as derived from surface height and dielectric measurements, are utilized in scattering models to derive backscattering coefficients. Results obtained using the Barrick and Peake model for slightly rough surfaces provided best agreement with σ^0 values derived from calibrated SAR data of the test fields. Calculated values using the Rice model were 6 to 10 dB larger than measured cross section values. Histograms of σ^0 for various test fields were constructed from SAR data. An Inverse Gaussian distribution provided the best fist to the histograms of the test fields. The Gamma distribution provide best fit to the Forest test sites.

The limited number of fields and range of roughness values precluded extensive analysis; however, the results obtained did indicate a trend of increasing σ^0 with increasing rms surface height roughness scale for bare fields. Correlation lengths of surface roughness did not show any particular correlation with σ^0.

Derived values of σ_0 have been compared to other published values as obtained from the University of Massachusetts data bank. Using published results obtained with conditions that best fit our derived values, general agreement (within 2 to 5 dB) were noted. Data utilized in a comparison included:

- A.J. Blanchard, et al., IEEE Geo. Rem. Sen. GE20(1), pp. 36-41, 1982; and
- F.T. Ulaby, et al., IEEE Geo. Rem. Sen. GE17(2), pp. 33-40, 1979.

Most data were obtained with relatively large values of incident angle so that comparisons are difficult as little low angle results are available.

Results obtained have shown that terrain scattering coefficients can be derived from calibrated L-band SAR. In addition, the large areal coverage capability of the SAR is used to obtain data from which scattering coefficients from a large number of sites and terrain types are derived. Although only a small fraction of the calibrated L-band SAR data available were utilized in this research due to funding limitations, scattering coefficients have been obtained from a wide variety of terrain types and forests areas. Data may be obtained for a wider range of incident angles, being limited only by the number of SAR data collection passes made.

Research reported in this report has focused on the reduction and analysis of L-band data from several programs conducted for other U.S. Government sponsors. Although much progress was made, there are still fundamental limitations in this data set. These limitations are within two areas: (1) the number of test sites and their location limited the variation in surface scattering parameters which is needed to fully develop L-band terrain scattering models; and (2) techniques

have to be further developed to measure the surface scattering properties of terrains, especially tree canopies. The following are specific recommendations for future work to continue and address the above stated goal of RADC.

1. Collect L-band radar cross-section coefficients over a wide variety of surface-terrains under a variety of conditions using a surface-based scatterometer,
2. Utilize available L-band SAR data and where necessary collect additional radar cross-section data over different terrain types as required, obtain surface measurements incident with RCS measurements,
3. Evaluate new techniques to measure the surface characteristics of various terrain types, including the use of a laser profiling system and photographic techniques, and
4. Correlate the surface scattering measurements to the L-band radar scattering data via deterministic and/or statistical scattering models.

It is anticipated that arrangements may be made in the future to collect X-L-C-band SAR data using the ERIM SAR which is being deployed on a U.S Navy P-3. With sponsor approval, the data from this system may also be processed to generate X-band, L-band and C-band terrain radar cross-section values. It is recommended that surface-based scatterometers be used to collect data at sites within each test area coincident with SAR data collection. The SAR and scatterometer data collections should be coordinated so that each instrument is collecting data on the same day. The scatterometer can be configured to collect data at a range of incidence angles.

It is further recommended that at each test site during SAR and scatterometer data collection period, surface scattering data be collected, including soil samples, surface profiles and surface photographs. One site should be established as an intensive test site.

Within this site, extensive scatterometer and surface scattering measurements should be obtained, including surface roughness profiles utilizing a laser-profiling device such as what has been developed at ERIM.

Verification of methods for the characterization of surface roughness. The use of recently developed laser profilers that allow large areas to be profiled with accuracies of better than 1 cm should be utilized in future research. Surface contours obtained using this system can be correlated with samples of surface roughness obtained using conventional techniques (Larson, 1986) to determine when surface roughness profile has been adequately sampled for use in scattering models. Since the measured surface profile is used to derive other surface descriptors for use in scattering models, the answer to this speculation is critical to the development of reliable models.

It is recommended that the North Carolina test be used to further develop techniques to quantify the structural characteristics of the forest canopy, and to relate these characteristics to the radar scattering signatures. This is recommended because of the extensive ground truth data available describing the entire forest test site. The surface profiling techniques developed for low-lying vegetation canopies cannot be applied to forest canopies, and different approaches must be developed. We recommend photogrammetric techniques to measure the canopy closure and the horizontal and vertical surface area of the different forest stands within the experimental forest west of Durham, North Carolina (i.e., the Duke Forest). These measurements, along with the other canopy characteristics which are on record for this forest (i.e., canopy height, stand or stem density, age, species diversity, and basal area or average stem diameter) may be correlated with the L-band radar cross-section data collected over this area. A data set already exists where SAR data were collected when there were no leaves on the trees. It is recommended that an

other data set be collected when leaves are on the trees along with coincident, photographics data when the SAR data is collected.

Analysis of this new data would provide the radar cross-section data to be correlated to the surface scattering data using statistical or deterministic scattering models, much in the same manner as was used in the present program. These results may then be used to add to the available data base for an L-band scattering model, and to provide additional empirical data correlation for verification of the L-band scattering model.

6
REFERENCES

Burns, B.A., "Determination of Ice Field Parameters from Multitemporal SAR Images," J. Geophys. Res., in press, 1987.

Cheng, R.C.H. and N.A.K. Amin, "Maximum Likelihood Estimation of Parameters in the Inverse Gaussian Distribution," Technomet., 23, pp. 257-263, 1981.

Christensen, N.L. and R.K. Peet, "Convergence During Secondary Succession," J. Ecol., 72, pp. 25-36, 1984.

Conover, W.J., Practical Nonparametric Statistics, John Wiley and Sons, Inc., New York, 1966.

Cosgriff, R.L., W.H. Peake, and R.C. Taylor, Terrain Scattering Properties for Sensor System Design, Ohio State University, May 1960.

Draper, N.R. and H. Smith, Applied Regression Analysis, John Wiley and Sons, Inc., New York, 1980.

Edeburn, J.D., Management of the Duke Forest, Duke University, 164, pp., 1981.

Folks, J.L. and R.S. Chhikara, "The Inverse Gaussian Distribution and Its Statistical Application - A Review," J.R. Statis. Soc. B, 40, pp. 263-289, 1978.

Kasischke, E.S., R.A. Shuchman, R.W. Larson, D.R. Lyzenga, J.C. Clinthorne, and P.L. Jackson, SAR Data Collection and Processing Summary - 1984 SARSEX Experiment, ERIM Topic Report No. 155900-21-T, Ann Arbor, MI, p. 146, 1985.

Kasischke, E.S., and C.C. Wackerman, "Analysis of Three-Frequency Synthetic Aperture Radar Imagery Collected Over a Southern U.S. Forest, submitted to IEEE Trans. Geosci. Remote Sens., 1987.

Kasischke, E.S., D.R. Lyzenga, R.A. Shuchman, and C.C. Wackerman, "Analysis of SARSEX Synthetic Aperture Radar Imagery, sub. to J. Geophys. Res., 1987a.

Kasischke, E.S., A.L. Maffett and R.W. Larson, "Statistical Modeling of Speckle Distributions on Airborne SAR Imagery," Proc. 1987 Inter. Geosci. Remote Sens. Symp., Ann Arbor, MI (in press) 1987b.

Kover, A.N. and J.E. Jones, "A Major Source of Side-Looking Airborne Radar Imagery for Research and Exploration: The USGS Geological Survey," IGARSS '85, pp.1 158-159, 1985.

Krohn, M.D., N.M. Milton and D.B. Segal, "SEASAT Synthetic Aperture Radar (SAR) Response to Lowland Vegetation Types in Eastern Maryland and Virginia," J. Geophys. Res., 88, pp. 1937-1952, 1983.

Larson, R.W., E.S. Kasischke, and A. Maffett, Calibrated L-band Measurements and Analysis Program, Interim Report No. RADC-TR-85-266, Air Force Systems Command, Griffiss AFB, N.Y., 164 p., 1986.

Larson, R.W., P.L. Jackson and E.S. Kasischke, "A Digital Calibration Method for Synthetic Aperture Radar Systems," IEEE J. Geosci. Remote Sens. (in press), 1987.

Lyon, J.G. and J.F. McCarthy, "Seasat Imagery for Detection of Coastal Wetlands," Proc. 15th Int. Symp. Remote Sens. Environ., Ann Arbor, MI, pp. 1475-1485, 1981.

MIZEX Group, "MIZEX East 83/84: The Summer Marginal Ice Zone Program in the Fram Strait/Greenland Sea," Eos, 67, pp. 513-517, 1986.

Onstott, R.G. and R.W. Larson, "Microwave Properties of Sea Ice in the Marginal Ice Zone Experiment," IGARSS 86 Digest, pp. 353-356, 1986.

Ormsby, J.P., B.J. Blanchard, and A.J. Blanchard, "Detection of Lowland Flooding Using Active Microwave Systems," Photogramm. Eng. Rem. Sens., 51, pp. 317-328, 1985.

Porcello, L.J., N.G. Massey, R.B. Innes and J.M. Marks, "Speckle in Synthetic Aperture Radar," J. Opt. Soc. Amer., 66, pp. 1305-1311, 1976.

Rawson, R., F. Smith and R. Larson, "The ERIM Simultaneous X- and L-Band Dual Polarized Radar," IEEE 1975 Int. Radar Conf., p. 505, 1975

Rice, S.O., Reflection of Electromagnetic Waves of Slightly Rough Surfaces, Symposium-Theory of Electromagnetic Waves, Interscience Pub. Co., New York, N.Y., 1951.

Ulaby, F.T., R.K. Moore and A.K. Fung, Microwave Remote Sensing, Active and Passive-Volume II: Radar Remote Sensing and Surface Scattering and Emission Theory, Addison-Wesley Publishing Co., Reading, MA, 607 pp., 1982.

Ulaby, F.T., R.K. Moore and A.K. Fung, Microwave Remote Sensing, Active and Passive-Volume III: From Theory to Application, Artech House, Inc., 1097, 1986.

*U.S. GOVERNMENT PRINTING OFFICE: 1988-500-000/60008